DETECTION OF SHALLOW BURIED CAVITY AND OBJECT WITH MICROWAVE REMOTE SENSING TECHNIQUE

A DISSERTATION

Submitted in partial fulfillment of the requirements for the award of the degree

of

MASTER OF TECHNOLOGY

in

ELECTRONICS AND COMMUNICATION ENGINEERING

(With Specialization in RF and Microwave Engineering)

By

PRASHANT MAHAJAN

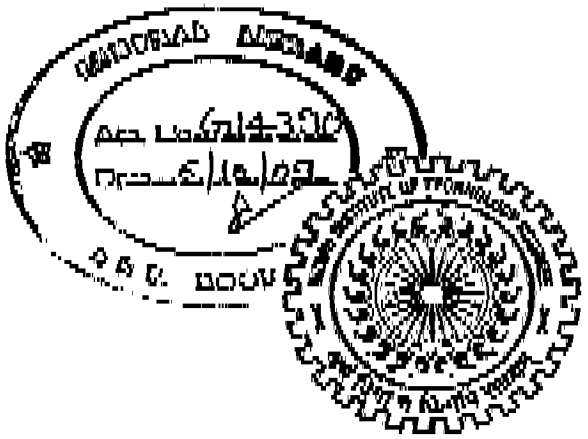

DEPARTMENT OF ELECTRONICS AND COMPUTER ENGINEERING
INDIAN INSTITUTE OF TECHNOLOGY ROORKEE
ROORKEE -247 667 (INDIA)

JUNE, 2009

CANDIDATE'S DECLARATION

I hereby declare that the work, which is presented in this dissertation report, entitled "**Detection of Shallow Buried Cavity and Object with Microwave Remote Sensing Technique**" being submitted in partial fulfillment of the requirements for the award of the degree of Master of Technology *with specialization in RF and Microwaves*, in the *Department of Electronics and* Computer Engineering, Indian Institute of Technology, Roorkee, India under guidance and supervision of Dr. Dharmendra Singh, Associate Professor, Department of Electronics and Computer Engineering, Indian Institute of Technology, Roorkee. The results submitted in this project have not submitted for the award of any other Degree or Diploma.

Date: 01 JULY 2009

Place: Roorkee

Prashant Mahajan

M Tech (2nd year)

ECE Department,

IIT Roorkee

CERTIFICATE

This is to certify that the statement made by the candidate is correct to the best of my knowledge and belief. This is to certify that the project entitled "**Detection of Shallow Buried Cavity and Object with Microwave Remote Sensing Technique**" is an authentic record of candidates own work carried out by him under my guidance and supervision. He has not submitted it for the award of any other degree.

(Dharmendra Singh)

Associate Professor, ECE Department,

ACKNOWLEDGEMENT

Knowledge and learning are ongoing processes in life which enable us to expand are horizon and capabilities. This can only be possible with the blessings and guidance of our teachers and help of our colleagues.

I would like to express my profound sense of respect and gratitude to my guide, Dr. Dharmendra Singh, Associate Professor, Department of Electronics and Computer Engineering , Indian Institute of Technology, Roorkee, for being instrumental in making me reach my target. I would like to thank him for his inspiration, guidance, constructive criticisms and encouragement throughout this project work.

My special thanks to the Mr. Abhay N. Gaikwad, Mr. Rishi Srivastav, Mr Triloki Pant and other Research Scholars of Remote Sensing Lab, Department of Electronics and Computer Engineering, IIT Roorkee for all the help and support they have extended to me throughout this dissertation work.

I am grateful to my parents and wife for their love, support and encouragement which they have extended to me patiently and quietly through this period.

Finally, I would like to extend my gratitude to all those persons who directly or indirectly helped me in the process and contributed towards this work.

Prashant Mahajan,

Abstract

A cavity is a body of material which has a lower density than that of the surrounding material. A cavity may be air filled (i.e. a void), it may be filled with water, alluvium, collapse material or a mixture of all of the above. The existence of this cavity alters the physical state of the strata, and results in a contrast between the cavity and the host stratum. Naturally occurring subsurface cavities posed a dilemma for civil engineers. Subsurface cavities were a problem at dams and reservoirs, resulting in severe leakage, water loss, and potential structural collapse. Microwave imaging of buried objects is widely used in sensing applications for geophysical exploration, medical imaging, civil engineering and non-destructive testing, in collapsed building or avalanche victims. Since very limited work has been carried out to detect the cavity using Microwave technique for remote sensing, an effort has been made to create and detect the subsurface air filled cavity in presence of other objects like metal. For this purpose a monostatic scatterometer is assembled, which can work at X and C-band with like polarization (i.e. HH and VV). The back scattered signal power is measured and processed by suitably modifying the techniques used in image processing. The techniques are used to set a threshold by which the returned signals are classified into detected objects. Encouraging results have been obtained which enforce that in near future with more detailed work, this technique may be a potential tool for subsurface cavity detection.

Acronyms

SAR	Synthetic Aperture Radar
GPR	Ground Penetrating Radar
RADAR	Radio Detection and Ranging
MRS	Microwave Remote Sensing
FGP	Foreground Pixels
BGP	Background Pixels
FAR	False Alarm Rate
DA	Detection Accuracy

Table of Contents

LIST OF FIGURES

LIST OF TABLES

CHAPTER 1

Introduction and Motivation

1.1 Problem Discussion

The fundamental process in subsurface detection is to visualize the composition of the subsurface which is not visible with the naked eye. It involves the detection of the objects using an appropriate sensor, and then to discriminate between objects of interest and objects not of interest. The shallow subsurface has assumed importance in engineering activities, environmental issues and archaeological investigations. It involves location of manmade resources such as utility pipes such as plastic and metallic gas pipes and water pipes, location of voids and tunnels possible exploration of energy sources such as oil, gas, and coal, demining, buried waste clean up, excavation planning, and archaeological investigations. The information regarding the subsurface is preferably obtained without disrupting it and this technique is called non-destructive technique.

A cavity is a body of material which has a lower density than that of the surrounding material. A cavity may be air filled (i.e. a void), it may be filled with water, alluvium, or a mixture of all of the above. The existence of this cavity alters the physical state of the strata, and results in a contrast between the cavity and the host stratum. Subsurface cavities are a problem at dams, reservoirs and canals, resulting in severe leakage, water loss, and potential structural collapse. The problem gets complicated in places where the urbanization has taken place at rapid rate thereby leaving limited scope of intrusive surveying and even non destructive surveying. Ninety percent utilities like water, telephone, sewer, gas pipelines lie up to 1.5 m depth which need to be detected, mapped and repaired. Military considerations led to the first efforts at remote cavity detection, as extensive tunnel complexes in Vietnam plagued American operations throughout the Southeast Asian war. The detection of bunkers and subsurface hangers for aircrafts and ammunition dumps can be other likely targets which need to be identified. Almost all developed cities across the world have or are in the process of subsurface tunneling for development of metro trains. These tunnels need constant monitoring and assessment from safety point of view. The voids in the surface of the airstrips, bridges and roads can be disastrous for the human life and vehicles. Huge storage

tanks and water channels which have been abandoned or not in use also need to be identified and mapped to avoid any constructions over such area without filling them.

Thus it can be clearly seen that most of the times it is not only difficult but also hazardous to carry out the survey. Thus a need is felt to explore the possibility of detecting the subsurface cavity remotely without having to undertake the rigmarole of deploying sensors or surveying onsite. Microwave remote sensing (MRS) can thus become an important tool to detect subsurface cavities especially shallow cavities by systematically scanning the target areas and processing the information. The advantage of microwave to scan at any time of the day and in any weather conditions can be added advantage. One of the most important features can be almost real time availability of reliable and accurate data. The system can be satellite or aircraft borne.

1.2 Overview

The detection of tunnels, pipes and other buried inhomogeneities has been recently addressed by using electromagnetic inverse scattering approaches [1]-[4]. Microwave imaging of buried objects is widely used in sensing applications, such as geophysical exploration, medical imaging, civil engineering and non-destructive testing, in collapsed building or avalanche victims [5] To detect the cavity the techniques being applied are: **Geophysical techniques** like Seismic refraction, Seismic reflection, Gravity survey technique [6], electrical resistivity imaging, electrical gradient techniques etc; **Electromagnetic techniques** like Measurement of the magnitude and direction of Earth's magnetic field [7], Electromagnetic Surveying etc; **Radar techniques** GPR [5], [8] and Crosshole Borehole Radar [9] to detect the cavity; **Miscellaneous techniques** like infrared scanners [10] and combination [11] [14] of the some above mentioned techniques. All these techniques have some limitations like observation can be taken only by going in near vicinity of the target and this is sometime difficult and some time dangerous also. To minimize this effect now days MRS technique is coming as a powerful tool

Still very limited work has been carried out to detect the cavity with **Microwave technique** for remote sensing. One of the probable cause for this is a compromise with the penetration depth that has to be made while considering the microwaves. The penetration depths of these waves are restricted because at higher frequency attenuation is more

Subsurface target identification is a challenging task as there are a variety of randomly distributed unwanted objects, returns from which obscure the return from the object of interest. Furthermore, the medium involved (i.e. the ground) is usually lossy, inhomogeneous and gives moisture-dependent losses that significantly limit the signal-to-noise ratio. The anisotropy and complex soil boundaries of the ground make the propagation of waves undergo reflection, refraction and diffraction, thus making energy transmission interpretation difficult. These together with the presence of the random roughness of air-ground interface make the task of subsurface target identification truly formidable. The return from the cavity gets obscured while the subsurface study is carried out with microwaves. The nature of the cavity also plays an important role as it may be filled with liquid or air. The constitutive parameters of the cavity content and its interaction with the surrounding medium affect the returns of the incident power.

Active microwave monostatic scatterometer technique has been utilized in our experimental work. The considered scene is irradiated with continuous waves synthesized by a frequency synthesizer and the back scattered power is measured with the same antenna. Transmit and receive paths are isolated using a circulator. The backscattered raw data is then processed to carry out the detection of the buried objects. The sequential processing of the raw data is carried out after suitably adopting the techniques available in image analysis mode. It involves the steps of preprocessing, image enhancement and object detection. Using this microwave technique with image analysis approach an endeavor has been made to detect the shallow air filled cavity and distinguish it from buried object at the same depth.

1.3 Available Techniques for Cavity Detection and their limitations

1.3.1 Seismic Waves The seismic method relies on the differences in velocity of elastic or seismic waves through different geological or man made materials. An elastic wave is generated in the ground by impact force (a falling weight or hammer blow) or explosive charge. The resulting ground motion is detected at the surface by vibration detectors called geophone (which converts ground motion into an analog electrical signal). A few successful mapping attempts using high-resolution seismic reflection surveys have been reported [15] [17]. Some limitations of this technique are

(i) The use of seismic methods to determine the geometry of the sub-soil is associated with a low level of success of these techniques in shallow investigations.
(ii) It entails a large set of resources to be employed onsite and attached to the ground to carry out the study due to which it is much slower than non contacting techniques.

1.3.2 Gravity Method The gravimetric method responds to differences in the mass of their surroundings, which results either from contrasts in the density of the ground, or from variations in geometry (cavities and voids, embankments, hills etc). Gravimetric technique involves measurement in variations in the intensity of the earth's gravitational field (expressed as acceleration in centimeters per second squared, or gals). This method has found its use in detecting the water or solution filled cavities using microgravimeters. The technique has been used for cavity detection by Butler [6] but the technique requires a lot of care such as
(i) Station measurements along a section or on a grid require great care in setting up the instrument, and the elevation of each station must be carefully surveyed. The height of each station has to be carefully managed.
(ii) Gravity data obtained in the field must be corrected for elevation, rock density, latitude, earth-tide variations, and the influence of surrounding topographic variations.

1.3.3 Electrical Resistivity Method In this method the resistivity of subsurface environment is measured by injecting an electrical current into the ground by a pair of surface electrodes and measuring the resulting potential field (voltage) between a second pair of electrodes. This method relies on measuring subsurface variations of electrical current flow which are manifested by an increase or decrease in electrical potential between two electrodes. Qady *et al.* have used this technique in conjunction with the GPR to detect subsurface cavities in Egypt [11]. But the interpretation of data in the presence of complex geology and the existence of natural currents and potentials is complex. Also the depths measured by this technique are normally an overestimation of the true investigation depth and on the other hand this technique involves the usage sensors which need to be placed on ground thus it is slow, time consuming and also the survey area is limited.

1.3.4 Ground Penetrating Radar (GPR) GPR applies to a range of electromagnetic techniques designed primarily for the location of objects or interfaces buried beneath the earth's surface or located within a visually opaque structure. GPR usually operates at frequencies between 1 and 2500 MHz and is capable of penetrating the ground to depths of more than 30m. While most GPR systems are used in close proximity to the ground, airborne systems have been able to map ice formations, glaciers, and penetrate through forest canopy. The great advantage is that this method is nondestructive and high speed. Despite having a lot of advantages it is focused with limitations like

(i) GPR is vulnerable to extremely high levels of clutter at short ranges and this is its major technical handicap.

(ii) It is important to define clearly the target parameters. There is a considerable difference between the target response from a buried pipe, a buried mine, a void or a planar interface. This has a major impact on antenna design, polarization state and signal processing strategy. Hence the related cost factors to it become limiting factors.

1.3.5 Thermal methods Measurements of temperature variations in the subsurface can be used as both a near surface and a borehole method. Because water has a high specific heat capacity compared to most natural materials, its temperature changes slowly as it migrates through the subsurface. Consequently, shallow earth temperatures can be related to the occurrence and flow of ground water. Shallow geothermal measurements are usually made by measuring subsurface temperatures at a selected depth (up to 40 inches) at numerous stations over a short time span to detect the water or liquid filled cavities. The technique involves placing large number of station on which measurements have to be made. Hence it is time consuming and covers a limited area.

1.3.6 Magnetometry Magnetic methods are based on the measurement of local variations in the earth's magnetic field using magnetometers. Such variations are associated with differences in magnetic susceptibility of rocks and soils or the presence of permanently magnetized bodies. Magnetic techniques are particularly useful in locating localized subsurface features of engineering interest such as abandoned mineshafts, sink holes, and buried services. The main advantage of the method is that magnetic measurements can be

made extremely fast and hence the use of the method is reasonably cheap. It has serious drawbacks like

(i) Measured field strengths are seriously affected by interference from electrical cables, electric railways, moving vehicles.

(ii) Urban areas have in abundance old foundations, buried services, and waste material gives rise to complex anomalies which can easily mask anomalies produced by singular features of engineering interest.

1.3.7. Combination of techniques Over a period of time large numbers of surveys have been carried out in combination of techniques to reinforce the results obtained from one technique. Some of the experiments which have been reported are given below

(i) Detection of underground cavities by combining gravity, magnetic and ground penetrating radar surveys has been reported Spain by Mochales *et al.* [12].

(ii) Integration of ground-penetrating radar and microgravimetric methods to map shallow caves by Bures *et al.* [13]

(iii) Combined geophysical techniques for cavity detection have been proposed by Abdelhady *et al.* in which Vertical Electrical Sounding (VES) and GPR have been utilized in Egypt [14].

(iv) Imaging subsurface cavities using geoelectric tomography and ground penetrating radar was carried out by Qady *et al.* in Egypt [11]

A point to be noted is that all the combination techniques mentioned here include GPR. Thus radar forms an integral part in this type of detection. However, GPR having its own limitations, an endeavor is being made to develop a technique which will be useful in detecting the subsurface cavity or void remotely.

It is observed after critically analyzing various available techniques that there is a need to explore the possibility of application of MRS technique for subsurface cavity or void detection. Viewing the importance of application of MRS on subsurface cavity detection, in this present thesis an attempt has been made to detect the subsurface cavity in controlled conditions in the laboratory. To enhance the results we have also applied some image analysis technique by which the detection can be strengthened.

1.4 Thesis Organization

The various techniques available for the detection of the cavities and voids have been discussed in Chapter 1. The aim of this discussion was to analyze the strength and weakness of each technique.

Since it is envisaged to detect a cavity using microwave technique for remote sensing and distinguish it from the two different objects located in proximity to each other below the surface, Chapter 2 gives a brief introduction to remote sensing before dwelling into the MRS and its technique.

Chapter 3 deals with the methodology and data processing to achieve the detection of the cavity. It explains how the back scattered signal power is measured and processed. It also deals with the data processing techniques used in this dissertation. Using image processing technique the raw data plot is then subjected to preprocessing and the techniques of image enhancement before applying the thresholding. Various thresholding techniques have been developed over a period of time for different applications. The choice of thresholding using Otsu and Entropy thresholding for spatial domain is preferred to keep the algorithm simple and computationally less taxing.

Chapter 4 covers the detailed discussion of results for the experimental work carried out for during this dissertation work. The X-band and C band results have been discussed and a brief comparison is made between the results at the two bands.

Chapter 5 highlights the conclusion and future scope of work.

CHAPTER 2

Microwave Remote Sensing

Remote Sensing is the science and art of acquiring information (spectral, spatial, radiometric and temporal) about material objects, area, or phenomenon, without coming into physical contact with the objects, or area, or phenomenon under investigation. Remote sensing, also called earth observation, refers in a general sense to the instrumentation, techniques and methods used to observe, or sense, the surface of the earth, usually by the formation of an image in a position, stationary or mobile, at a certain distance remote from that surface. In remote sensing electromagnetic radiation coming from an object, are measured and translated into information about the object or into processes related to the object.

2.1 Remote Sensing

Remote Sensing is classified into three types in respect to the wavelength regions [18], [19].

- Visible and Reflective Infrared Remote Sensing.
- Thermal Infrared Remote Sensing.
- Microwave Remote Sensing.

The following components are involved in the process of remote sensing:

- The source of the electromagnetic radiation which is transmitted
- The path through the atmosphere
- The interaction with the object
- The recording of the radiation by a sensor (reception)
- Preprocessing of the recorded radiance
- Interpretation and analysis of the remote sensing data to give the final product

The remote sensing is divided into two methods based on the instrument [20]. The two types of remote sensing instruments are: passive and active. Passive instruments detect the reflected or emitted electromagnetic radiation from natural sources or from the observed scene. Active sensors are the instruments that radiate or illuminate the object or scene they observe. The energy is radiated from the sensor to the object and reflected or backscattered radiation is received from that object.

2.2 Microwave Remote Sensing

MRS image data is gathered by measuring the strength of energy scattered back to the sensor in response to energy transmitted [19]-[21]. The degree of reflection is characterized by the scattering coefficient for the surface material being imaged. This is a function of the electrical complex permittivity of the material and the roughness of the surface in comparison to a wavelength of the radiation used. Because of their long wavelengths, compared to the visible and infrared, microwaves have special properties that are important for remote sensing. Longer wavelength microwave radiation can penetrate through cloud cover, haze, dust, and all but the heaviest rainfall. This property allows detection of microwave energy under almost all weather and environmental conditions so that data can be collected at any time.

Surface interface radars have been utilized to conduct subsurface detection at bands lower than X-band. The predominantly used bands are P, L, S, C, and X-bands. The semi and to arid desert are the best for carrying out subsurface detection using microwaves as the sand affords deep penetration based on the wavelength of incident wave and soil conditions like humidity.

2.2.1 Microwave Sensors Some microwave sensors can detect the small amounts of naturally emitted microwave energy within its field of view. Such sensors are called passive because they detect MR that is generated externally, for example, by emittance by or reflectance from a target. The microwave energy recorded by a passive sensor can be emitted by the atmosphere, reflected from the surface, emitted from the surface, or transmitted from the subsurface. Because the wavelengths are so long, the energy available is quite small. Thus, the fields of view must be large to detect enough energy to record a signal. Most passive microwave sensors are therefore characterized by low spatial resolution. Passive microwave sensors are typically radiometers or scanners with an antenna to detect and record the microwave energy. Passive microwave radiometers such as the Scanning Multi channel Microwave Radiometer (SMMR) produce imagery with a low spatial resolution that is used to provide measurements of sea surface temperature and wind speed, and also to detect sea ice. Applications of passive MRS include meteorology, hydrology, and oceanography. By

looking at, or through the atmosphere, depending on the wavelength, meteorologists use passive microwaves to measure atmospheric profiles and to determine water and ozone content in the atmosphere. Hydrologists use passive microwaves to measure soil moisture since microwave emission is influenced by moisture content. Oceanographic applications include mapping sea ice, currents, and surface winds as well as detection of pollutants, such as oil slicks [19].

Active microwave sensor generates its own electromagnetic radiation at centimeter wavelengths, transmits this energy towards the ground, and then detects the strength of the backscattered signal from the target in the direction of the sensor [22]. Active microwave sensors are generally divided into two distinct categories: imaging and non-imaging. The most common form of imaging active microwave sensors is RADAR. The strength of the backscattered signal is measured to discriminate between different targets and the time delay between the transmitted and reflected signals determines the distance (or range) to the target. Non-imaging microwave sensors include altimeters and scatterometers. In most cases these are profiling devices which take measurements in one linear dimension, as opposed to the two-dimensional representation of imaging sensors. Some of the key active space borne sensors are given below [23].

• *RADARS* Different types of radars are being utilized today for the remote sensing purpose. The important ones have been briefly introduced.

(i) Synthetic Aperture Radars (SAR) Sensors looking to one side of the nadir track, collecting a phase and time history of the coherent radar echo from which typically can be produced a radar image or interferometric topographical map of the earth's surface. A new generation of SAR sensors is coming into existence, designed to be operationally stable, equipped with capabilities such as multifrequency, multipolarization data gathering, interferometric modes, and wide-swath coverage. The list of applications for SAR as a remote sensing tool is also rapidly expanding in fields as diverse as oceanography, forestry, sea-ice monitoring, planetary exploration, geology, agriculture, and terrain mapping.

(ii) Precipitation Radars These radars scan perpendicular to nadir track, measuring the radar echo from rainfall, to determine the rainfall rate over the earth's surface concentrating on the tropics.

(iii) Cloud Profile Radars These radars look at nadir, measuring the radar echo return from clouds, to determine the cloud reflectivity profile over the earth's surface.

• *Altimeters* Radar altimeters transmit short microwave pulses and measure the round trip time delay to targets to determine their distance from the sensor. Generally altimeters look straight down at nadir below the platform and thus measure height or elevation (if the altitude of the platform is accurately known). Radar altimetry is used on aircraft for altitude determination and on aircraft and satellites for topographic mapping and sea surface height estimation.

• *Scatterometers* They are also generally non-imaging sensors and are used to make precise quantitative measurements of the amount of energy backscattered from targets. The amount of energy backscattered is dependent on the surface properties (roughness) and the angle at which the microwave energy strikes the target. Thus scatterometry is a form of radar remote sensing that can measure various geophysical properties of surfaces based on the amplitude of microwave electromagnetic pulses.

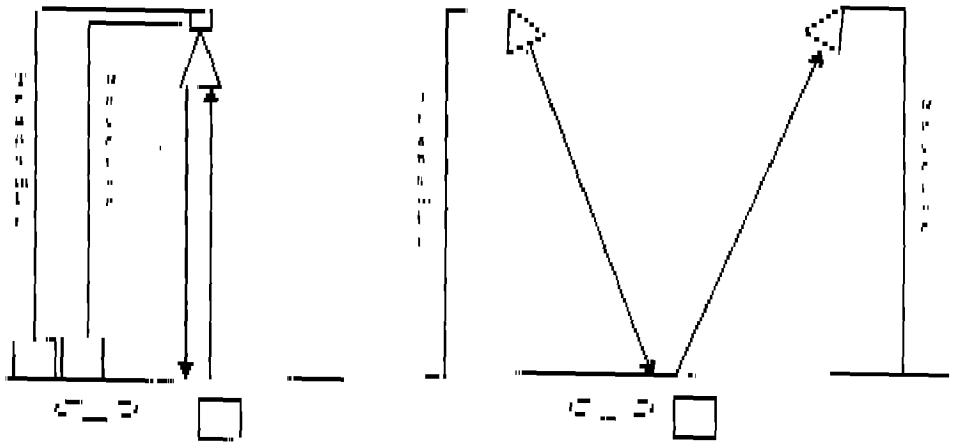

Fig. 2.1. Monostatic and bistatic scatterometer.

Scatterometry measurements over ocean surfaces can be used to estimate wind speeds based on the sea surface roughness. Ground based scatterometers are used extensively to accurately measure the backscatter from various targets in order to characterize different materials and surface types. Two primary types of scatterometer are monostatic and bistatic as shown in Fig. 2.1. In bistatic scatterometer the transmitting and receiving antennas are

located away from each other. In monostatic case the two antennas are collocated. Thus monostatic configuration is a special case of the bistatic system where the angle between the two antenna reduces to zero.

In this experimental work monostatic system with single antenna is considered which will enable only co-polarized (HH and VV) study. The antenna is connected to a circulator thus providing sufficient isolation to the receiver from the transmit path

2.3 Interaction of Microwaves with the Target

Complex interactions take place between the incident microwaves and the targets on/below the surface [24]. Besides the system related parameters the geometrical and electrical properties of the target along with its local surface geometry influence the backscatter. The magnitude or intensity of this backscattered energy is dependent on how the radar energy interacts with the surface, which is a function of several variables or parameters. The brightness of features in a radar image is dependent on the portion of the transmitted energy that is returned back to the radar from targets on the surface.

2.3.1 Sensor Parameters As the radar is an active instrument, the characteristics of the transmitted signal can be controlled. In particular, the wavelength and polarization of the signal are important properties of the radiation source used in remote sensing [24], [25].

- *Wavelength/Frequency* Radar wavelength has a direct bearing on the degree of penetration of the surface material achieved by the microwave such that lower frequency penetrates deeper into the medium. Most satellite-borne sensors that operate in the microwave region use microwave radiation with wavelengths between 3 and 25 cm. Radiation at these wavelengths can penetrate cloud, and the microwave band is thus a valuable region for remote sensing in temperate and tropical areas where cloud cover restricts the collection of optical and thermal infrared images. At L band wavelengths (approximately 23 cm), microwave radiation can penetrate the foliage of trees and, depending on the height of the tree, may reach the ground. Backscatter occurs from the leaves, branches, trunks, and the ground surface. In areas of dry alluvial or sandy soils, L-band radar can penetrate the ground for several meters. The same is true for glacier ice. Shorter wavelength C-band

radiation can penetrate the canopies of trees, and the upper layers of soil and ice. Even shorter wavelength X-band SAR mainly sees the top of the vegetation canopy and the soil and ice surface.

• *Polarization* The polarization of an electromagnetic wave refers to the orientation of the electric field during propagation. For radar systems, this can be chosen to be parallel to the earth's surface on transmission (a situation referred to as horizontal polarization or H mode) or in the plane in which both the incident and scattered rays lie (somewhat inappropriately called vertical polarization or V mode). The degree of polarization rotation that occurs can be a useful indicator of surface material [25]. The polarization of the signal has an effect on the nature and magnitude of the backscatter. There can be four combinations of both transmit and receive polarizations as follows:

(i) HH - for horizontal transmit and horizontal receive.

(ii) VV - for vertical transmit and vertical receive.

(iii) HV - for horizontal transmit and vertical receive.

(iv) VH for vertical transmit and horizontal receive.

The first two polarization combinations are referred to as like-polarized or copolarized because transmit and receive polarizations are the same. The last two combinations are referred to as crosspolarized because transmit and receive polarizations are orthogonal to one another. Polarimetric radars are able to transmit and receive both horizontal and vertical polarizations. Thus, they are able to receive and process all four combinations of these polarizations. HH, HV, VH, and VV. Since our system involves only co polarized antenna orientation complete polarimetric set can not be studied.

Each of these polarizations has varying sensitivities to different surface characteristics and properties. Thus the availability of multi polarization data helps to improve the identification of and the discrimination between features. In addition to recording the magnitude (i.e. the strength) of the returned signal for each polarization, most polarimetric radars are also able to record the phase information of the returned signals. This can be used to further characterize the polarimetric signature of different surface features.

2.3.2 Target Parameters The *target parameters* that influence the backscattering process are discussed below [28]. They are directly interrelated to the sensor parameters.

- *Surface Roughness* It refers to the average height variations in the surface cover from a plane surface, and is measured on the order of centimeters [23]. Whether a surface appears rough or smooth to radar depends on the wavelength and incidence angle. The *surface* roughness of a feature controls how the microwave energy interacts with that surface or target and is generally the dominant factor in determining the tones seen on a radar image. The *same* surface has different effective roughness in different frequencies and different incidence angles. A surface is considered smooth if the height variations are much smaller than the radar wavelength. When the surface height variations begin to approach the size of the wavelength, then the surface will appear rough. Thus, a given surface will appear rougher as the wavelength becomes shorter and smoother as the wavelength becomes longer. There are two *criterions for the surface roughness*

(i) Rayleighs criteria $$h > \frac{\lambda}{8\cos\theta} \qquad (2.1)$$

(ii) Fraunhofers criteria $$h > \frac{\lambda}{32\cos\theta} \qquad (2.2)$$

where h is the height variation of the surface and λ is the wavelength.

The latter is a more stringent criterion for the natural surfaces. Based on the amount of scattered power received the image is formed. Three types of *scattering* are shown in Fig. 2.2 (a), (b) and (c)

(i) Specular A smooth surface causes specular scattering of the incident energy (generally away from the sensor) and thus only a small amount of energy is returned to the radar. This results in smooth surfaces appearing as darker tonal areas on an image [22].

(ii) Diffused A rough surface will scatter the energy approximately equally in all directions (i.e. diffusely) and a significant portion of the energy will be backscattered to the radar. Thus, rough surfaces will appear lighter in tone on an image.

(c) Mixed It is *an intermediate condition* between the specular and diffused scattering. If the radar energy does manage to penetrate through the topmost surface, then volume scattering may occur. Volume scattering is the scattering of radar energy within a volume or

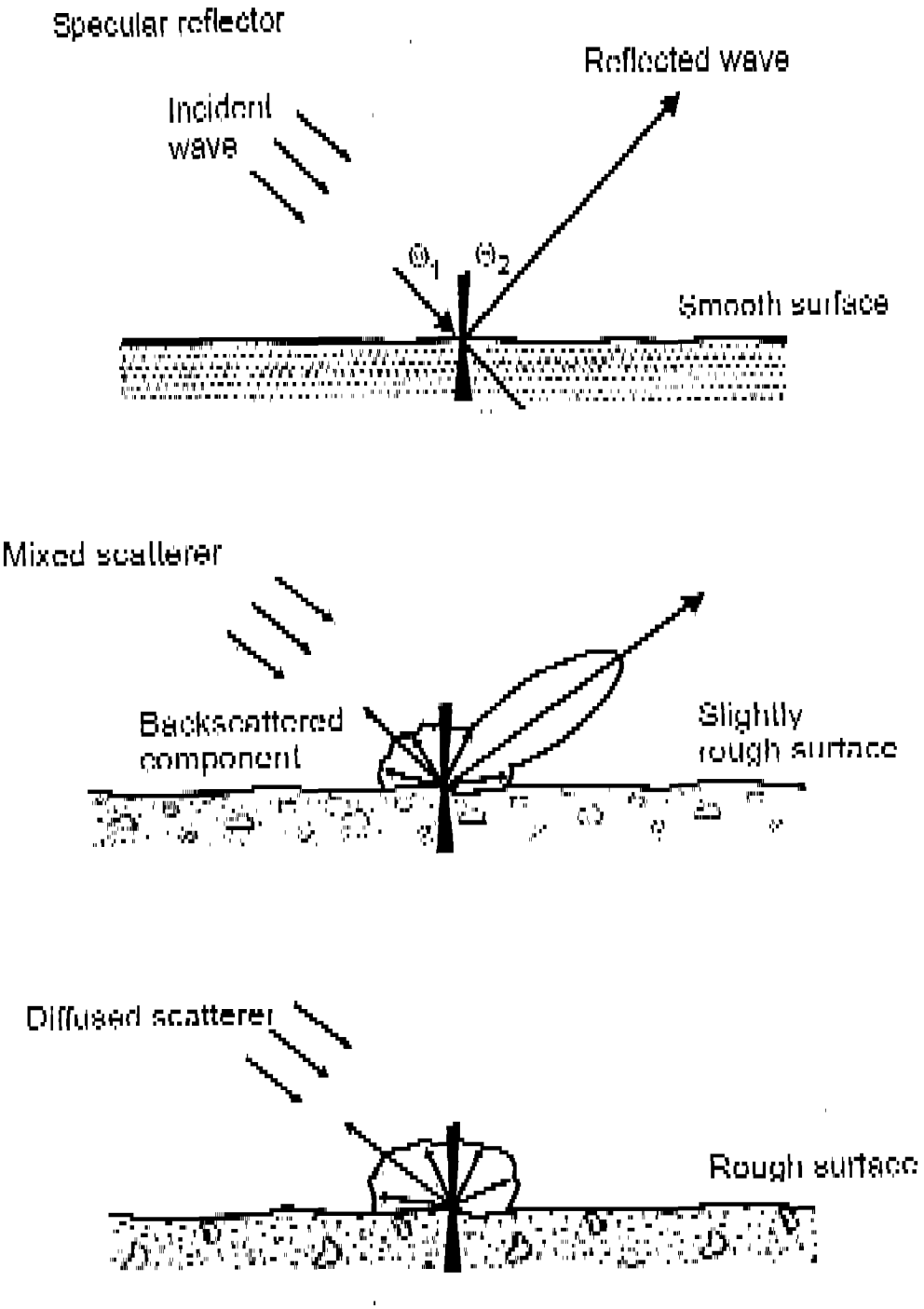

Fig. 2.2 Types of scattering (a) Specular (b) Diffuse (c) Mixed [24].

medium and usually consists of multiple bounces and reflections from different components within the volume. For example, in a forest, scattering may come from the leaf canopy at the tops of the trees, the leaves and branches further below, and the tree trunks and soil at the

ground level. It may serve to decrease or increase image brightness, depending on how much of the energy is scattered out of the volume and back to the radar.

In this thesis we have maintained smooth and dry surface thus the scattering is bound in the constraints of specular scattering.

- *Dielectric Properties* The dielectric constant is a response of a medium to an applied electrical property. The physical parameters that affect the dielectric constant are soil moisture, soil texture, bulk density, salinity, organic matter, and temperature. The change in soil dielectric constant is more influenced by change in soil moisture content than other soil characteristics listed above. The increase in soil moisture results in the increase in dielectric constant. The dielectric constant is denoted by symbol ϵ. The dielectric constant is a complex number consisting real (ϵ') and imaginary (ϵ'') parts shown in equation below

$$\epsilon = \epsilon' - j\epsilon'' \tag{2.3}$$

The real part refers to the relative permittivity and it influences the wave propagation and the amount of energy scattered. The imaginary part refers to the dielectric loss factor and defines the absorption properties of the media.

- *Moisture Effect* The presence (or absence) of moisture affects the electrical properties of an object or medium, changes in the electrical properties, influence the absorption, transmission, and reflection of microwave energy. Thus, the moisture content will influence how targets and surfaces reflect energy from radar and how they will appear on an image. Generally, reflectivity increases with increased moisture content.

If the target is very dry and the surface appears smooth to the radar, the radar energy may be able to penetrate below the surface, whether that surface is discontinuous (e.g. forest canopy with leaves and branches), or a homogeneous surface (e.g. soil, sand, or ice).For a given surface, longer wavelengths are able to penetrate further than shorter wavelengths. The depth of penetration of microwave radiation at a particular wavelength is proportional to the surface soil moisture as shown in Fig. 2.3.

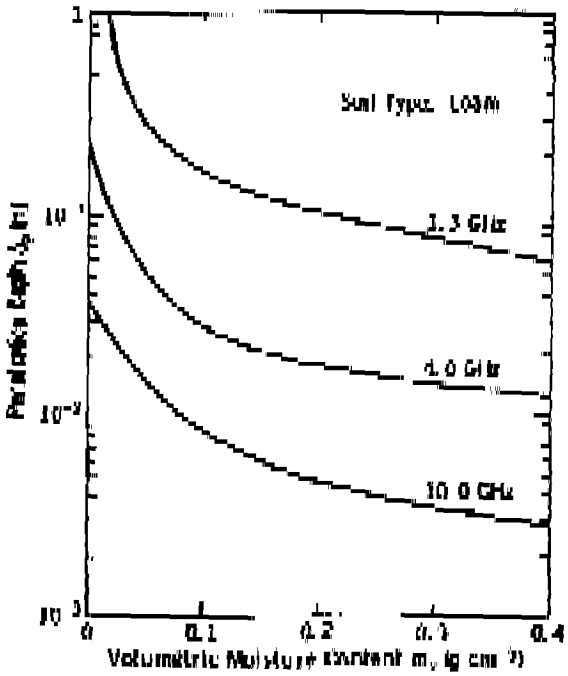

Fig. 2.3. Penetration depth as a function of moisture content for soil [27].

2.4 Applications of MRS

There are numerous applications of MRS. These have been briefly summed up as

- Vegetation mapping and Agriculture: identification and estimation of crop growth [28]-[30]
- Surveillance of forests and Environment Assessment [31] [33]
- Ocean surveillance and marine resources [31], [34].
- Hydrology: estimation of ground moisture, maps of rivers, expanses of water and flooded areas [31].
- Ice surveillance: displacement measurement of ice, navigation channel surveillance, iceberg detection [34], [35].
- Cartography, Urban and Land use applications: production of maps and three dimensional digital terrain models measurement of landslides and erosion phenomena [31], [32].

• Geology: identification of geological structures using low-frequency waves to pass through plant cover [32].

• Meteorological applications [33], [34].

• Disaster management: Drought and flood damage assessment [31].

• Soil moisture assessment [35]-[37].

CHAPTER 3

Methodology and Data Processing

3.1 Experimental Set up for Microwave Measurements for Cavity Detection

The schematic diagram of setup for the cavity/metal plate detection is as shown in the Fig. 3.1. An indigenous monostatic radar system at X-band with 10 GHz and C-band with 6 GHz of frequency of operation has been assembled. The system contains a microwave source (Rhode & Schwarz signal synthesizer SMR27: 10 MHz to 27 GHz), power meter (Rhode & Schwarz NVR8), circulator and horn antenna. It is used to supply 18 dBm of CW power at 10 GHz and 6 GHz frequency during the experimental work. The horn antenna is mounted on a movable platform at a height of 1.05 m and 0.40 m above the sand surface for the X-band and C-band respectively where it can slide both in x and y direction. The power meter is used to detect the backscattered power from the sand pit and is isolated from the transmission circuit by using a circulator. The circulator has an isolation of 28 dB. The system is mounted on a movable platform and has the flexibility in x and y direction for motion.

A sand pit of dimension 1.5 m × 1.5 m of depth 40 cm has been artificially created in which the cavity is buried inverted along with other objects. For obtaining the image we moved the radar system in both x and y direction at regular interval of 5 cm to form a matrix of 24 × 24 in a grid of 1.2 m × 1.2 m. Thus in all total of 576 readings were taken for each iteration.

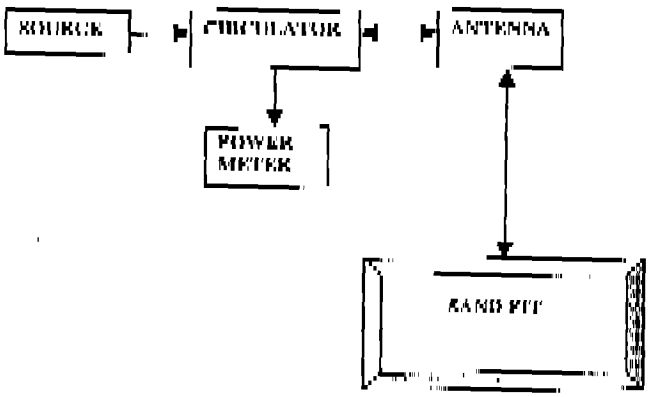

Fig. 3.1 Experimental setup schematic.

3.1.1 Antenna characterization Both the X-band and C-band antenna were characterized in the anechoic chamber to ensure noise isolation. The elevation and azimuth angles were calculated once the radiation pattern was plotted as tabulated in Table 3.1. The plotted radiation patterns have been shown as Fig. 3.2. (a), (b) and Fig. 3.3. (a), (b). Smaller beam width provides the finer spatial resolution, i.e. spatial resolution increases with the decrease in beam width. Sufficiently narrow beamwidth have been obtained for the two horn antenna. The gain measurements were carried out using the reference antenna which was compared with the approximate formula

$$\text{Gain (dB)} = 10 \log_{10}\left[\frac{41253}{\theta_e \times \theta_h}\right] \tag{3.1}$$

Using the above formula with the calculated values of elevation and azimuth angle we get the gain for X and C-band as 21 dB and 22.1 dB. Another important parameter which needs to be calculated is the swath. Swath of the antenna is defined as the elliptical area that the antenna beam can illuminate on the plane in any direction. The swath, A on the surface of the sand with the antenna at height h is given by:

$$A = \pi \times a \times b \tag{3.2}$$

where:

$$a = h \times \tan\left(\frac{\theta_e}{2}\right) \tag{3.3}$$

$$b = h \times \tan\left(\frac{\theta_h}{2}\right) \tag{3.4}$$

Thus by replacing the values of a and b from (3.3) and (3.4) into (3.2) we get the swath as

$$A = \pi \times h^2 \times \tan\left(\frac{\theta_e}{2}\right) \times \tan\left(\frac{\theta_h}{2}\right) \tag{3.5}$$

Table 3.1 Antenna characteristics for the experimentation.

Ser No	Frequency Band	Elevation Angle (Degree)	Azimuth Angle (Degree)	Height of Antenna above Sand Surface	Antenna Gain (dB)	Antenna Swath
1.	X band	16.8	19.5	1.05 m	19.39	879 cm^2
2.	C-band	15.2	16.7	0.40 m	21.31	31.33 cm^2

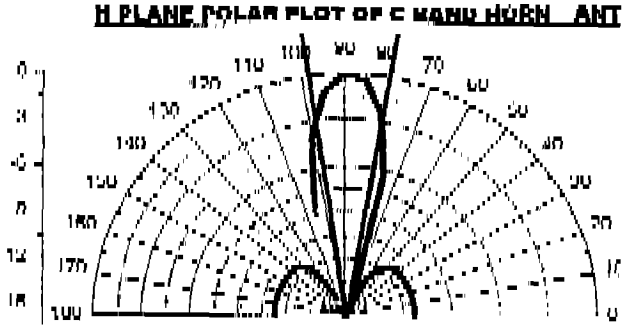

Fig. 3.2. (a) H plane polar plot of C-band Horn antenna.

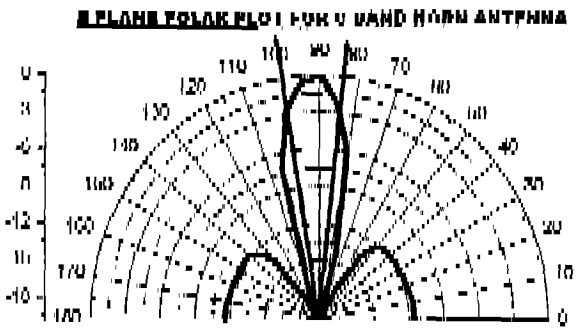

Fig. 3.2. (b) E plane polar plot of C band Horn antenna.

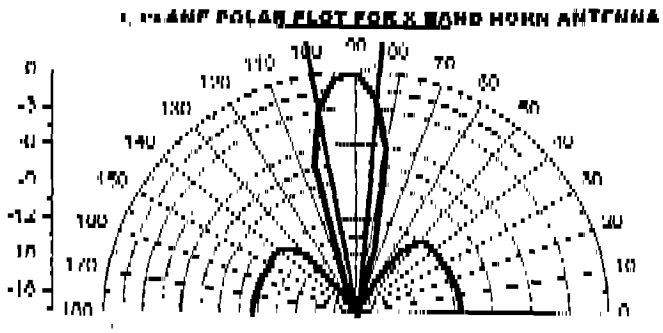

Fig. 3.3. (a) H plane polar plot of X band Horn antenna.

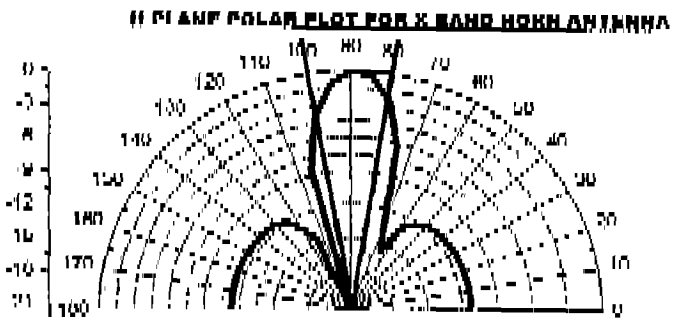

Fig. 3.3. (b) E plane polar plot of X band Horn antenna.

3.1.2 Cavity formation and its characterization Two different cavities of dimension 32 cm × 22 cm × 20 cm with different thickness were prepared from soil as shown in Fig. 3.4. (a), (b).These were placed individually in the sand such that cavity is visible from the top and the scattered power is measured as seen in Fig. 3.4. (c). For each cavity the scattered power levels were recorded individually. The thin cavity was buried inverted (the open end of the cavity is looking down) such that the cavity faces the ground below the surface of the sand and the backscattered power was measured. This was followed by placing the thin cavity inverted in sand along with following a metal plate in all iteration at different depths.

Fig. 3.4. (a) Cavity with thick walls.

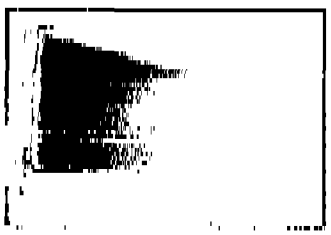

Fig. 3.4. (b) Cavity with thin walls.

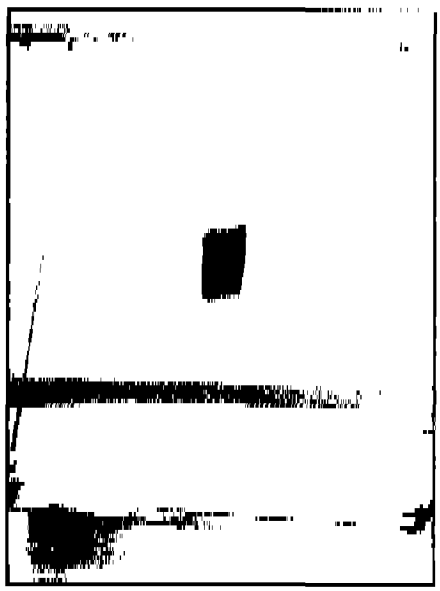

Fig. 3.4. (c) Cavity buried in test bed.

During the preparation of these cavities it was ensured that they were dried in the sun till complete dryness was achieved (and not baked at high temperature) to maintain the soil properties.

3.1.3 Determination of complex permittivity of the cavity It was then imperative to find the complex permittivity and loss tangent of cavity which was carried out using the transmission line technique. This technique is used to measure the characteristics of the low loss material. The dielectric constant is a complex number consisting real (ε') and imaginary (ε'') parts shown in equation below.

$$\varepsilon = \varepsilon' - j\varepsilon'' \tag{3.6}$$

The real part is associated with the ability of the dielectric material to store energy while the complex part with the losses that occur in a material. The loss of energy as heat is measured as the loss tangent. Loss tangent is the ration of power dissipated to the power stored per cycle.

$$\tan \delta = \frac{\varepsilon'}{\varepsilon''} \qquad (3.7)$$

The shift in minima position with and without the insertion of sample is the measure of the dielectric constant. The shift in the distance between the 3 dB point on either side of the minima with and without the sample is used to measure the loss tangent. Thus we can calculate the imaginary part of the dielectric constant from (3.7). To carry out this activity square pellets of the cavity soil were formed and fitted into the X-band metal plate with slot. Great care was taken to fit these pellets tightly without any gap with the slot walls and it was also ensured that the surface of these pellets was smooth.

The position of voltage minimum and spacing between half power point with and without the specimen were measured using the slotted line section. The following equations were used to measure the dielectric constant

$$\varepsilon' = \left(\frac{x\lambda_0}{2\pi t}\right)^2 + \left(\frac{\lambda_0}{\lambda_c}\right)^2 \qquad (3.8)$$

where λ_0 is the free space wavelength, λ_c is the cutoff wavelength and t is the thickness of the sample.

The value of x in (3.8) is found by solving the equation

$$\frac{\tan x}{x} = \frac{\lambda_0}{2\pi t} \times \tan \frac{2\pi(1+d)}{\lambda_g} \qquad (3.9)$$

where λ_g is the guide wavelength, d is the shift in the position of the minima.

Since the solution of the LHS of the (3.9) is multi valued we need to know the approximate value of x to find its exact value. Thus after finding the value of x we can find the value of ε''. The value of tan δ can be found from the (3.10) below

$$\tan \delta = \frac{d_1 - d_2}{x' \times t}\left(\frac{\lambda_0}{\lambda_g}\right)^2 \qquad (3.10)$$

where d_1 and d_2 are the distances between the 3 dB point without and with the specimen. The values were found in the lab and using this technique the complex dielectric constant at 10 GHz frequency was found to be 3.6269 + j0.2289 which is quite close to dry sand [38]. Thus an effective air cavity was created using soil with almost similar dielectric constant as sand.

3.1.4 *Data Collection* *For iteration at a given depth, first the square meal plate and then* the triangular metal plate was buried alongside the inverted cavity. Adequate care was taken while filling up the sand and leveling it each time. The surface was kept smooth and dry. The back scattered power was measured by taking plane polarized in HH and VV at normal incidence for all the targets. Thus a total of 4 sets of readings for individual cavities and 12 sets of readings for thin cavity with different targets at different depths were recorded in the X-band and 6 sets of reading in C-band were taken as given in Table 3.2. These sets of readings are then utilized to detect the cavity and the metal plate by using the image processing [39]-[41] algorithm based on MATLAB [42], [43]. The back scattered power levels obtained were in the decreasing order for the regions containing the metal plate, inverted cavity and sand.

Table 3.2 Different objects used in experiment.

Ser No	Target	Dimensions	Polarisation	Depth
1.	Cavity with Square Plate	30 cm × 30 cm	Both HH and VV in X-band	1 cm, 5 cm , 8 cm at X-Band
			HH in C band	2 cm, 5 cm , 10 cm at C-Band
2.	Cavity with Triangular Metal Plate	Each side of 30 cm	Both HH and VV in X band	1cm, 5 cm , 8 cm at X-Band
			HH in C band	2 cm, 5 cm , 10 cm at C-Band

3.2 Microwave Modeling

The primary aim of this dissertation is to detect the cavity. Since the cavity is made of soil having almost the similar characteristics as sand the microwaves will have interaction with an air filled cavity and metal plate. These have been discussed below.

3.2.1 Metal Plate The total returned electric field, as shown in Fig. 3.5, at the scatterometer [38], [44] receiver, E_R, arising due to incident electric field, E_i, is the result of simultaneous effect of

- Specular reflections and the diffuse scattering from the air-sand interface.
- Reflection from the Aluminum reflector at the depth H under the surface.
- Diffraction and scattering by surface irregularities of the reflector.
- Volume scattering from the inhomogeneities of the sand layer.

We can neglect the diffuse and the diffraction component of the electric field scattered by the aluminum reflector, as it is smooth with respect to the radar wavelength of 3 cm. Since the thickness of the aluminum reflector is much greater than the depth of its skin layer, which is of order of micrometer, its surface can be considered a flat boundary through which there is no further penetration of the electric field into sand.

Consequently, E_R consist of the backscattered power from homogeneous layer of sand that is located between medium 1 and medium 3 with a flat specular reflecting boundary at $z = -h$ and a boundary between medium 1 and medium 2 is described by a function h(x, y), where h is the variation of the surface height relative to horizontal plane $z = 0$.

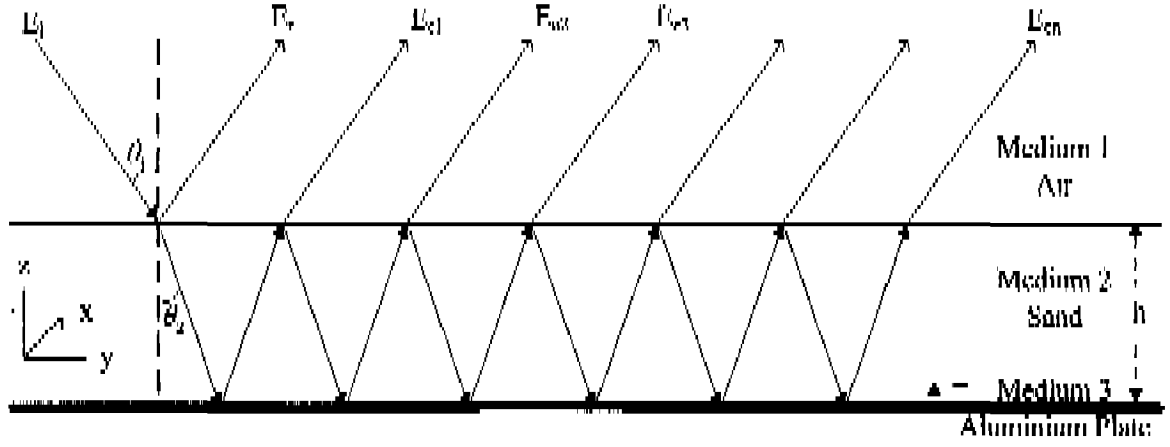

Fig. 3.5. Electromagnetic wave interaction with metal plate.

The Electromagnetic wave propagation for the metal plate assumes that the incoming electromagnetic wave with electrical field E_i is planar, medium 2 is infinite in both directions x and y, and medium 1 and 3 are also effectively infinite in the directions of the z axis and $-z$ axis, respectively. The resultant electric field E_R can be considered as the superposition of the following electrical fields and is given by (3.11).

- The returned electric field at the air sand interface E_r
- The returned electric field after one reflection at the aluminum reflector E_{s1}
- The returned electric field after two or more reflections at the aluminum reflector and at the air sand interface.

$$E_R = E_r + E_{s1} + E_{s2} + \ldots + E_{sn} \tag{3.11}$$

By placing the values of various components in (3.11) it has been shown that the backscattered power is given by (3.12) below [34].

$$E_s = \sqrt{1 - 4k^2\sigma^2\cos\theta_i}\exp\left(-\frac{1}{2}\sin\theta_i\right)\left(\frac{R_{1-2} + R_{2-3}\exp(-2\gamma_2 h)}{1 + R_{1-2}R_{2-3}\exp(-2\gamma_2 h)}\right) \tag{3.12}$$

where k is the wave number, σ is the roughness parameter, θ_i is the incident angle, h is the depth, $R_{1-2} = \frac{\sqrt{\varepsilon_1} - \sqrt{\varepsilon_2}}{\sqrt{\varepsilon_1} + \sqrt{\varepsilon_2}}$ and $R_{2-3} = \frac{\sqrt{\varepsilon_2} - \sqrt{\varepsilon_3}}{\sqrt{\varepsilon_2} + \sqrt{\varepsilon_3}}$, γ is the propagation constant, ε is the relative permittivity and subscripts 1, 2, and 3 are for air, sand and metal plate respectively.

The (3.12) can be used to calculate the electric field at different depths with other factors remaining constant.

3.2.2 Cavity Space In the case of the void in the sand surface due to cavity emplacement the complexity of the problem increases with three layers for interaction. It has been assumed that the cavity has the same constitutive parameters as sand and is infinite in both x and y directions. Thus the reflections at the upper and lower interface of the medium 3 take place as R_{2-3} and R_{3-2} as in case of normal incidence. Thus an additional component of reflection from the lower interface of the cavity, which undergoes transmission at cavity (medium3) sand (medium 2) interface and sand (medium 2) air (medium 1) is added to the superposition of the backscattered power in (3.11) as shown by the red dotted lines along side the blue lines. The higher order reflection and transmissions have not been considered. Thus

3.3.1 Preprocessing of the Backscattered Power Data It involves two main processes.

- *Calibration* To carry out the calibration the system, a flat aluminum sheet was placed over the surface and readings were taken for all the iteration after burying the objects and leveling the sand. This data was used while processing the readings for detection of the buried objects. The raw matrix of observed data is first calibrated [44] using the data matrix obtained for the metal sheet to give the image pixel

$$E_{calibrated} = \frac{E_{observed}}{E_{metal}} \tag{3.14}$$

where $E_{observed}$ is the backscattered power of the buried object and E_{metal} is the backscattered power of the metal plate.

- *Normalization* The calibrated data is range bound by carrying out normalization. This is carried out by using the following equation

$$E_n = \frac{E_{cal} - E_{mean}}{E_{max} - E_{min}} \tag{3.15}$$

where E_{cal}, E_{mean}, E_{min} and E_{max} are the calibrated, mean, minimum and maximum calibrated powers respectively.

3.3.2 Data Enhancement The preprocessed data is then enhanced by reducing the effect of neighboring pixel and filtering in the spatial domain. This involves the process of convolution and filtering.

- *Convolution* As the illuminated area of the antenna is larger than the pixel area size, the normalized image is then required to be convoluted to minimize the effect of the overlapping of the scattered field from the neighboring pixels and the random noise spikes in the image. Convolution is a simple mathematical operation which is fundamental to many common image processing operators. It provides a way of multiplying together two arrays of numbers, generally of different sizes, to produce a third array of numbers of the same dimensionality. This can be used in image processing to implement operators whose output pixel values are

simple combinations of certain input pixel values. One of the input arrays is normally just a gray level image. The second array is usually much smaller, and is also two dimensional (although it may be just a single pixel thick), and is known as the kernel. The convolution is performed by sliding the kernel over the image, generally starting at the top left corner, so as to move the kernel through all the positions where the kernel fits entirely within the boundaries of the image. It uses the extension of the size of the image by zero-padding outside the original image, and this will eliminate the effect of walls as well.

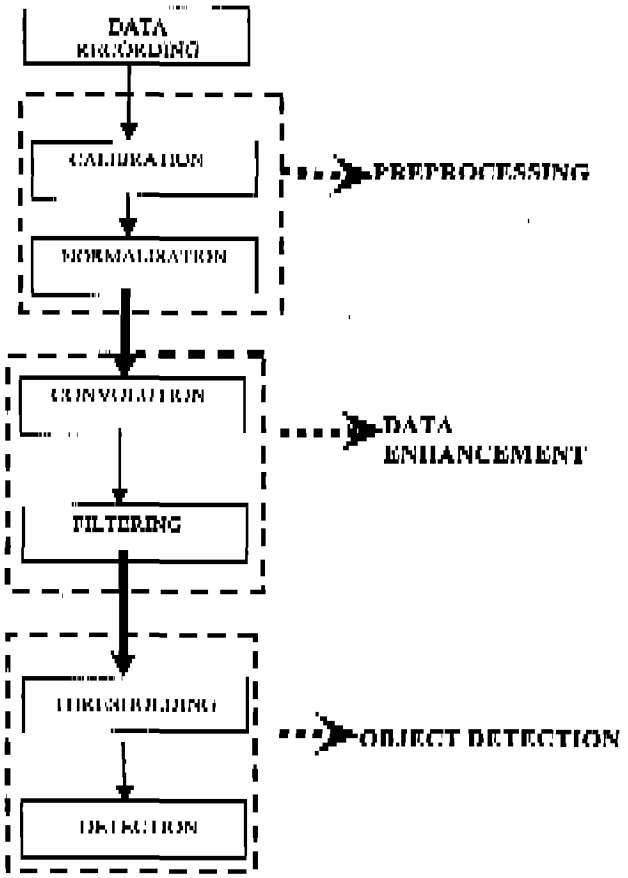

Fig. 3.7. Flow chart for detection.

• *Filtering* Various spatial filters are available in the Image Processing toolbox in MATLAB. The two filters used are the columnwise filter and median filter.

(i) Columnwise filter (colfilter) processes distinct or sliding blocks as columns. It has been used in this work as it converges much faster than the others neighborhood filters with equal accuracy and it has the capability to filter the results around the maximum, minimum and other statistical values like mean and median. Since we have three different interest areas so

the colfilter is used keeping the mean value of the convoluted matrix as the reference. If we were to highlight only the metal object from the back ground the colfilter with maximum value as the reference would have been preferred.

(ii) Another filter used is median filter. Median filtering is similar to using an averaging filter, in that each output pixel is set to an average of the pixel values in the neighborhood of the corresponding input pixel. However, with median filtering, the value of an output pixel is determined by the median of the neighborhood pixels, rather than the mean. The median is much less sensitive than the mean to extreme values.

3.3.3 Detection After minimizing the noise from the data using preprocessing and data enhancement, threshold techniques can be employed to filter out the surface returns and detect the buried objects.

• *Threshold* It is a simple but effective tool to separate objects from the background which has been effectively employed in processing works. However the task of setting a threshold requires careful selection of technique. Different threshold techniques [45] have been developed for different applications. The threshold techniques have been borrowed from image processing for this microwave problem. In image processing the threshold selection methods have been classified into two groups, namely, global methods and local methods. Global threshold technique thresholds the entire image with a single value whereas a local threshold method partitions the given image into a number of sub-images and determines a threshold for each of the sub-images. The output of the threshold operation retains the values above threshold while it makes all the values below the threshold as zero, this image is referred to as foreground pixels (FGP) image while the complementary state will correspond to the background pixels (BGP) where below threshold values have been retained while those above have been set to zero and the image is referred to as BGP image. The histogram based threshold [46] and entropy threshold [47] in spatial domain are the techniques which can be effectively utilized for the detection and localization of the buried objects. In this study only the global threshold technique.

(i) In the gray levels histogram threshold technique as described by Otsu [48], the gray levels histogram of the image pixels is considered without any a priori knowledge. If T, gray

levels {1,2,..., L} are being considered in an image of total N pixels such that the number of pixel at i level is denoted by n_i , then $N = n_1 + n_2 + ... + n_L$. The gray level histogram is normalized and considered as probability distribution such that

$$p_i = n_i/N \quad , p_i \geq 0 \text{ and } \sum_{i=1}^{L} p_i = 1 \tag{3.16}$$

The pixels belonging to the BGP are segregated from the pixels belonging to the object in FGP by a threshold level t. The pixels with levels {1, 2,..., t} denote the background and those above threshold {t+1,..., L}denote the object. Then probability of the back ground and the object are given as

$$\Gamma_B^t = \sum_{i=1}^{t} p_i \quad \Gamma_O^t = \sum_{i=(t+1)}^{L} p_i \tag{3.17}$$

The mean and the variance with the background and the object can be classified as

$$\mu_B^t = \frac{1}{P_B^t} \sum_{i=1}^{t} i p_i \text{ and } \mu_O^t = \frac{1}{P_O^t} \sum_{i=(t+1)}^{L} i p_i \tag{3.18}$$

$$\text{var}_B^t = \frac{1}{P_B^t} \sum_{i=1}^{t} (i - \mu_B^t)^2 p_i \text{ and } \text{var}_O^t = \frac{1}{P_O^t} \sum_{i=(t+1)}^{L} (i - \mu_O^t)^2 p_i \tag{3.19}$$

The global mean of the image is given by

$$\mu = \sum_{i=1}^{L} i p_i \tag{3.20}$$

Two more variances are considered: between class variance and within class.

$$\begin{aligned} \text{var}_{\text{between-class}}^t &= P_B^t(\mu_B^t - \mu)^2 + P_O^t(\mu_O^t - \mu)^2 = P_B^t P_O^t(\mu_B^t - \mu_O^t)^2 \\ \text{var}_{\text{within-class}}^t &= \Gamma_B^t \text{var}_B^t + \Gamma_O^t \text{var}_O^t \end{aligned} \tag{3.21}$$

The threshold value t is so found that it either maximizes the between class variance or equivalently minimizes the within class variance.

(II) The principle of entropy is to use uncertainty as a measure to describe the information contained in a source. The maximum information is achieved when no a priori knowledge is available, in which case, it results in maximum uncertainty. This concept has been extensively used in image processing, since an image can be interpreted as an information source with the probability law given by its image histogram. Using maximum entropy as an

optimal criterion for image threshold was first proposed by Pun [49]. It was later corrected and improved by Kapur *et al.* [50]. The maximization of entropy has been used to set the threshold, t to divide the image into FGP and BGP and hence detect the subsurface buried objects. Let us assume that there M total pixels and p_i be an estimate of the probability of gray level value such that

$$p_i = \frac{n_i}{M} \tag{3.22}$$

where n_i is the total number of pixels having gray value i.

It is then assumed that the two classes of pixels the conditional entropy is defined as

$$H(F) = \sum_{i=0}^{t-1} \frac{p_i}{p(T)} \log_2 \frac{p_i}{p(T)}$$

$$H(B) = -\sum_{i=t}^{L} \frac{p_i}{p(B)} \log_2 \frac{p_i}{p(B)} \tag{3.23}$$

The *information* between the two classes is defined as the sum of their respective entropies H(F) and H(B)

$$I(F, B) = H(F)+H(B) = \varphi(t)$$

The above equation can be rewritten as

$$\varphi(t) = \log_2[p(F) \cdot p(B)] + \frac{H_t}{p(F)} + \frac{H_L - H_t}{p(B)} \tag{3.24}$$

where $H_t = -\sum_{i=0}^{t-1} p_i \log_2 p_i$ and $H_L = \sum_{i=0}^{L} p_i \log_2 p_i$

The threshold t is so chosen that function $\varphi(t)$ is maximized. Thus using the information theory concept the threshold t is set at a level that entropy of the image has to be maximized.

Though both the Otsu and Entropy techniques are setting the threshold level using which they are classifying the pixels as FGP and BGP, the main difference between these techniques is that Otsu technique uses the histogram to form within class and between class variance to maximize the latter to set the threshold while the Entropy method maximizes the entropy of the image to set the threshold. Another difference is that Otsu technique is using histogram while the entropy technique is using the self information concept.

• *Detection* Two threshold setting techniques have been utilized to set the threshold level. All the pixels of the filtered image are then compared to the threshold level. The pixels above the threshold are classified as FGP while those below the threshold are classified as BGP for which two separate images are formed and shown in the results. The unsupervised detection is carried out by using a code written in MATLAB. Since the cavity and metal plate are both buried at the same depth the metal plate will give better return due to which the cluster of pixels with highest return value depict the metal plate. Thus cavity and metal plate are detected and identified separately. To assess the correctness manual comparison is carried out with the actual position of the buried object in the image. To check the efficiency of the methodology detection accuracy and false alarm rate have been calculated.

(i) Detection Accuracy (DA). It is the ratio of the correctly detected pixels after detection to the total number of pixels of the object.

$$DA = \frac{\text{Number of correctly detected pixels}}{\text{Total number of pixels of the objects}} \times 100 \tag{3.25}$$

(ii) False Alarm Rate (FAR). It is the ratio of the incorrectly detected pixels after the threshold process to the number of pixels other than the object in the data.

$$FAR = \frac{\text{Total Incorrectly Detected Pixels}}{\text{Total Pixels} - \text{Number of object pixel}} \times 100 \tag{3.26}$$

CHAPTER 4

Results and Discussion

The processing of the raw data obtained in the experimental work is in form of backscattered power received in a matrix of 24 × 24. This data is processed in a sequential manner as shown in the flow chart in Fig. 3.7 of section 3.3 in the previous chapter. The raw image is subjected to three stages of processing in which the raw image is preprocessed by calibrating and normalization to bring the data into a range. This is followed by image enhancement process wherein the normalized image matrix is convoluted and filtered to enhance the target information. In the last stage of processing the threshold is set and the image pixels are compared with the threshold level to carryout detection of the buried objects.

4.1 Results and Discussion for the Experimental Work at X-band

Table 4.1 Details of analysis and subsection at X-band.

Ser No	Polarization	Buried Object	Depth	Frequency	Subsection
1.	HH	Sand Pit	-	10 GHz	4.1.1
2.	HH	Cavity looking upwards	Surface	10 GHz	4.1.2
3.	HH	Cavity inverted	Surface	10 GHz	4.1.3
4.	HH	Cavity with square plate	1 cm	10 GHz	4.1.4
5.	VV	Cavity with square plate	1 cm	10 GHz	4.1.5
6.	HH	Cavity with triangular plate	1 cm	10 GHz	4.1.6
7.	VV	Cavity with triangular plate	1 cm	10 GHz	4.1.7
8.	HH	Cavity with square plate	5 cm	10 GHz	4.1.8
9.	VV	Cavity with square plate	5 cm	10 GHz	4.1.9
10.	HH	Cavity with triangular plate	5 cm	10 GHz	4.1.10
11	VV	Cavity with triangular plate	5 cm	10 GHz	4.1.11
12.	HH	Cavity with square plate	8 cm	10 GHz	4.1.12
13.	VV	Cavity with square plate	8 cm	10 GHz	4.1.13
14.	HH	Cavity with triangular plate	8 cm	10 GHz	4.1.14
15.	VV	Cavity with triangular plate	8 cm	10 GHz	4.1.15

The details of observations carried out in X-band and the subsections under which the analysis is carried out in given in Table 4.1. The preliminary experimentation in the X band was carried out on sand pit without any buried target. This was followed by observing the backscattered powers for the cavity face open as seen in Fig. 3.4 (c) and then inverted cavity. Then the depth of the cavity and metal plate (square and triangular metal plate) were changed and readings taken in both the HH and VV polarizations at each depth as given in the Table 4.1.

4.1.1 Sand Pit Data The initial investigations were carried out by studying the backscattered powers from the sand pit in HH mode as given in Ser No 1 in Table 4.1. The image plot of raw data of the backscattered power is shown in Fig. 4.1.

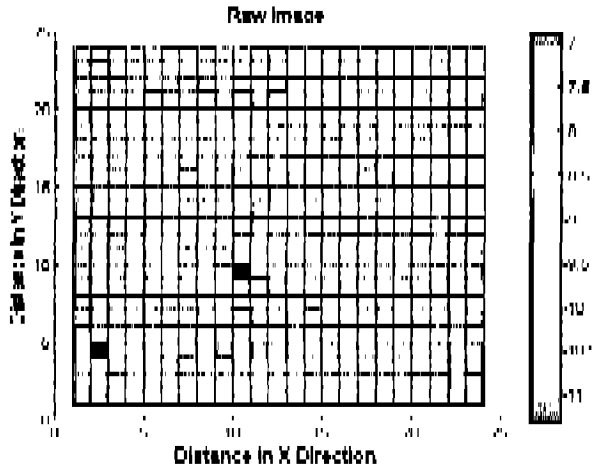

Fig. 4.1. (a) Raw data image.

4.1.2 Cavity Facing Upwards The preliminary study on the cavity was carried out by placing the cavity such that the open end of cavity is at the sand surface with cavity visible (open cavity) when viewed from the top as mentioned in Ser No 2 of the Table 4.1. The raw image has been plotted as shown in Fig. 4.2 (a). Then the image is calibrated and normalized to bring the raw data in a range. After normalization the convolution is carried out as mentioned in the flow chart in Fig. 3.7 of section 3.3. This processing has been done for all the analysis in the remaining subsections. The normalized image is then filtered about the mean as can be seen in Fig. 4.2 (b). The cavity has been marked with the black ring showing the lower power when compared to the surrounding region

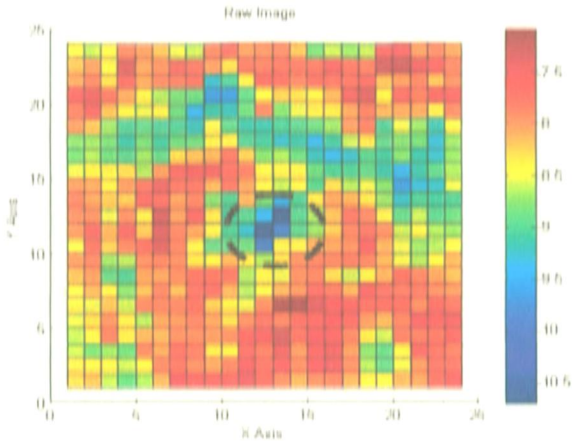

Fig. 4.2 (a) Raw data image.

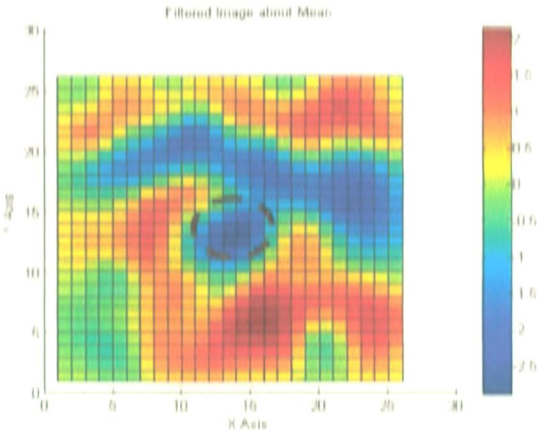

Fig. 4.2 (b) Filtered image about mean.

4.1.3 Inverted Cavity at Surface The cavity was then inverted at the surface such that its open end in buried in sand. Due care was taken to level the sand surface at open face of the cavity when buried in sand. The raw image for this case has been shown in Fig. 4.3 (a). By looking at raw image we do not get much information regarding the placement of the cavity. This was subjected to the process of calibration and normalization before being convoluted and filtered. However post filtering about mean we get a sharp rise around the cavity region as shown in Fig. 4.3 (b) as anticipated.

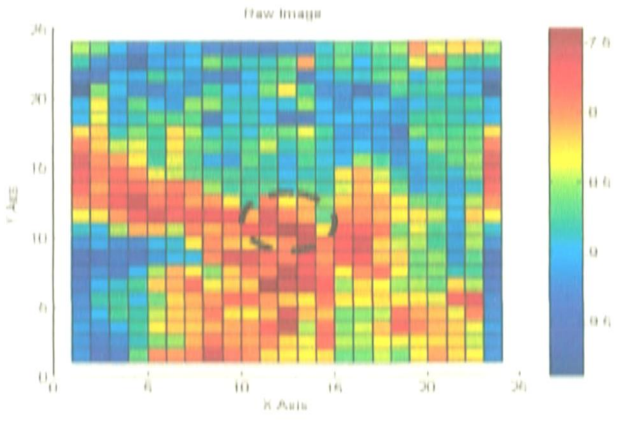

Fig. 4.3 (a) Image of raw data.

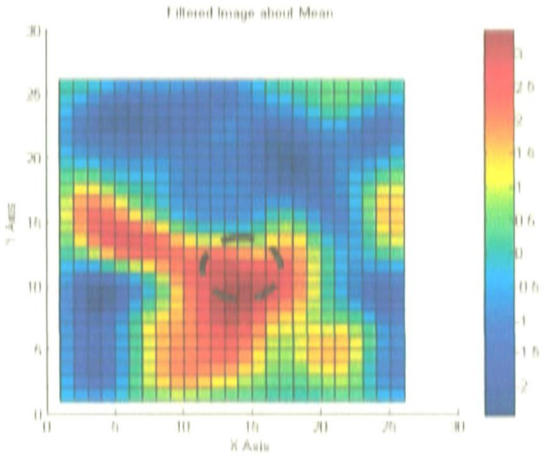

Fig. 4.3 (b) Filtered image about mean.

4.1.4 Inverted Cavity with Square Metal Plate Buried at 1 cm Depth The cavity and metal plate (in this instance square plate) were buried at the depth of 1 cm and the observations are carried out with HH polarization. The processing has been carried out as given in the flow chart in Fig. 3.7. On completion of the preprocessing the normalized plot is obtained and shown in Fig. 4.4. Two peaks of different intensities are observed in the figure indicating the presence of cavity and metal plate. Owing to higher reflectivity the metal plate should have the higher peak while the lower peak should be representing the cavity. To analyze the data more critically further processing has been carried out.

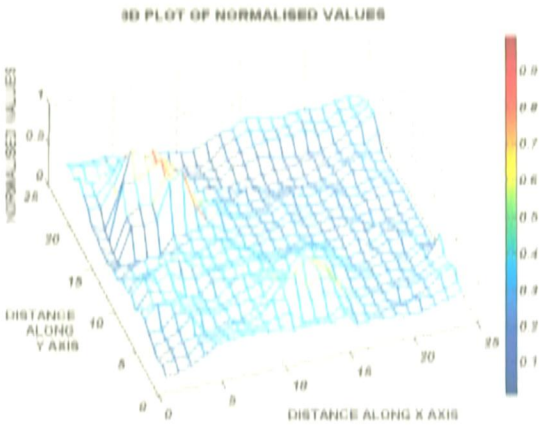

Fig. 4.4. Normalized 3D plot.

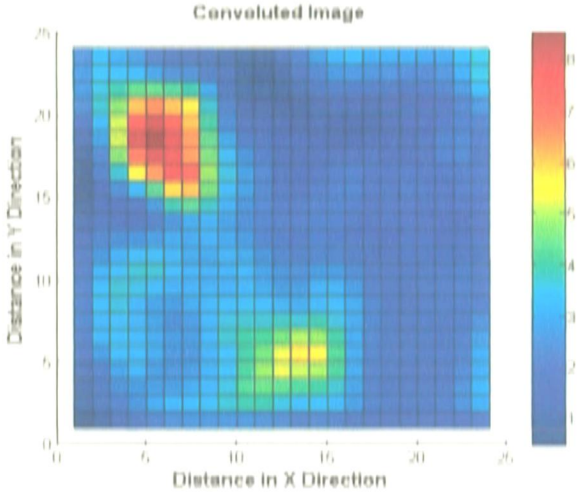

Fig. 4.5. Convoluted image.

The normalized data is then convoluted as described in section 3.2.2 to minimize the effect of neighboring pixels on pixel strength. In this image the higher intensity variation can be easily identified but it is difficult to infer the kind of target.

To enhance the target information filter application is required. As discussed the column filter with various statistical data like maximum, minimum, mean and median has been checked. It is found that the column filter with mean gives better results as shown in Fig. 4.6. (a). To analyze the process of filtering, median filter has been applied as shown in Fig. 4.6. (b). On comparing the convoluted image in Fig. 4.5. with the filtered images in Fig. 4.6. (a), (b) we can observe the presence of buried objects (cluster of red color and yellow color pixels). It is observed that the range of value in unfiltered is from 0-9 while that of filtered images if from 0-7.

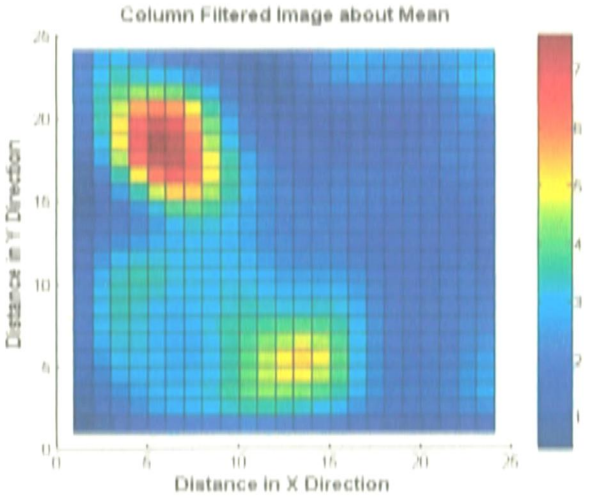

Fig. 4.6 (a) Filtered image using Column filter.

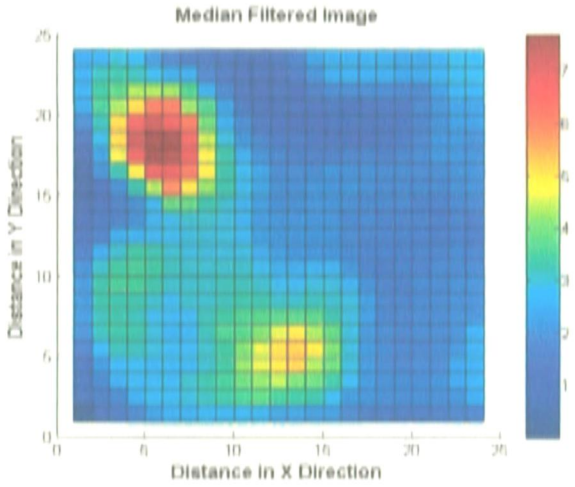

Fig. 4.6 (b) Median filtered image.

This image is now ready for detection after setting and applying threshold. On applying the threshold, we divide this image into FGP and BGP. Two threshold techniques have been applied: Otsu and Entropy threshold.

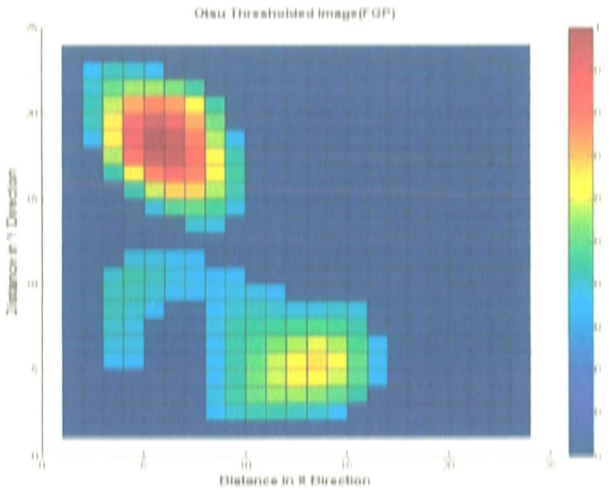

Fig. 4.7. (a)

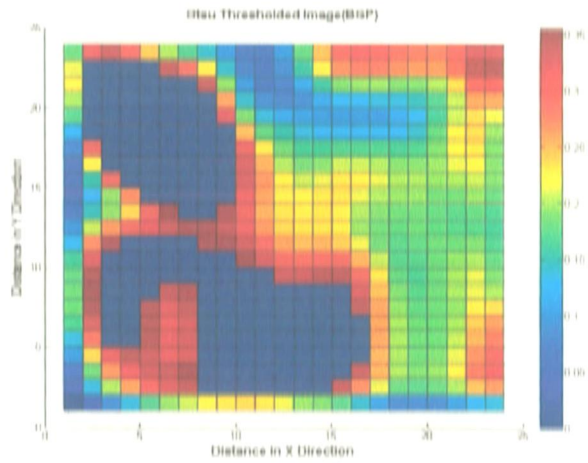

Fig. 4.7. (b)

Fig. 4.7. (a) Threshold image using Otsu threshold showing FGP.

Fig. 4.7. (b) Threshold image using Otsu threshold showing BGP.

It can be seen from Fig. 4.7. (a) that both the cavity and the metal plate have been detected when the Otsu thresholding is applied. A total 146 pixels were observed of which 56 pixels were accurately detected while the remaining were false alarm. Thus a 100% detection

accuracy with 17.31% false alarm was observed using Otsu threshold. A total of 18 pixels were detected for the metal plate giving a total detection accuracy of 32%. However no false alarm was observed in this case.

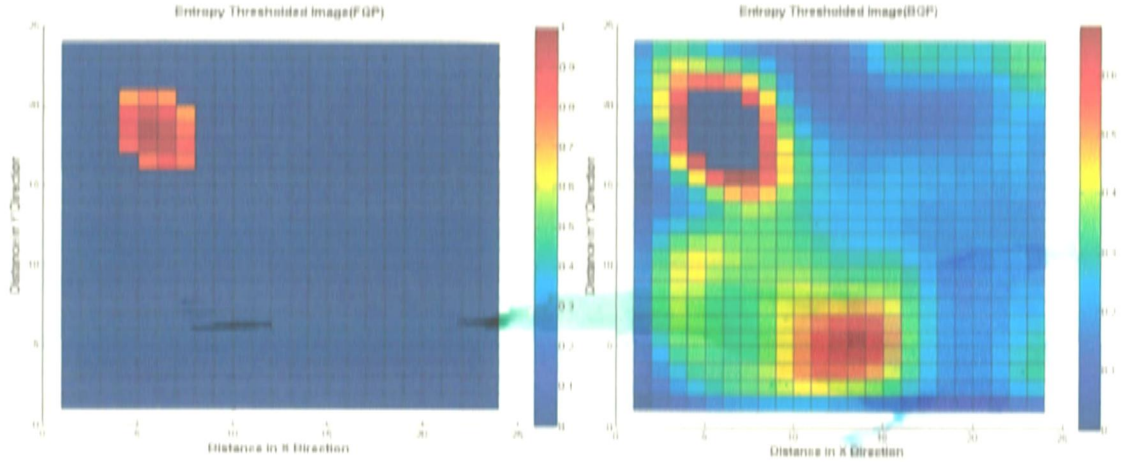

Fig. 4.8. (a) Fig. 4.8. (b)

Fig. 4.8. (a) Entropy threshold indicating FGP.

Fig. 4.8. (b) Entropy threshold indicating BGP.

The Otsu threshold FGP image was plotted using histogram as shown in Fig. 4.9. Since in this image has maximum number of pixels at 0 intensity the image was scaled on the x axis from 30%. It can be observed in Fig. 4.7. (a) that the maximum false alarm pixels were just above the threshold level, they can be eliminated using the histogram as the initial peak is of those pixels. The range bins in the histogram for the metal plate are at the highest threshold values while the interim peaks indicate the cavity.

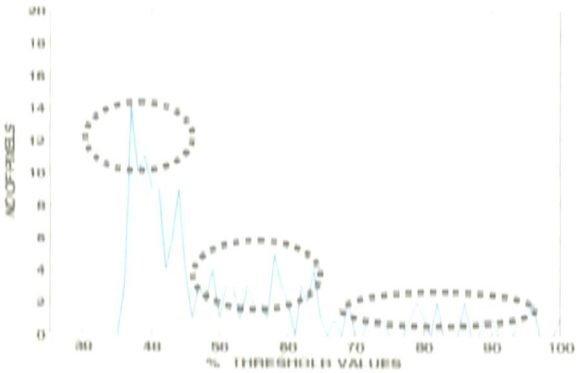

Fig. 4.9. Histogram plot of Otsu threshold image.

4.1.5 Inverted Cavity with Square Metal Plate Buried at 1 cm Depth The cavity and square metal plate were buried at the depth of 1 cm and the observations are carried out with VV polarization as mentioned in Ser No 5 of Table 4.1.

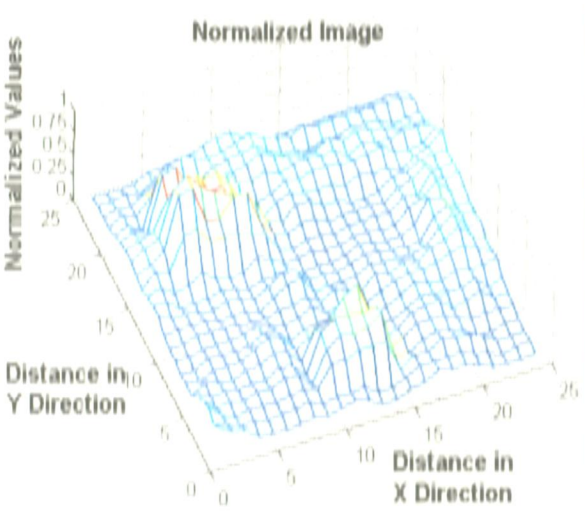

Fig. 4.10. Normalized 3D plot.

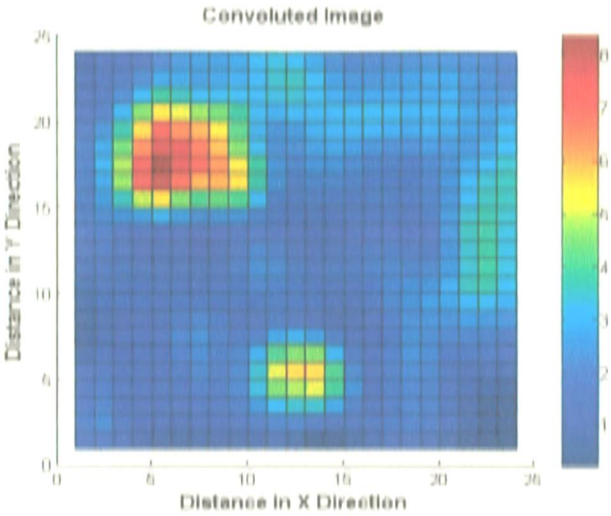

Fig. 4.11. Convoluted image.

The normalized image shown in Fig. 4.10. indicates the presence of two prominent regions which indicate the presence of the metal plate and the cavity in sand in the decreasing order of reflectivity as discussed in the previous subsection. This normalized image is then convoluted to minimize the effect of neighboring pixels as a process of image enhancement. In the convoluted image as seen in Fig. 4.11., we are able to view two prominent groups of pixels.

Filtering is carried out to improve the target pixel enhancement. The columnwise filtered image about the mean and the median filtered image are obtained. The two filtered images are shown in Fig. 4.12. (a), (b). On critically observing the convoluted and filtered images it can be noticed that the boundary pixels in the region of the two bright clusters have been enhanced during filtering. The range values of the convoluted image ranges from 0-8.5 while that for filtered images range from 0-7.5 as can be viewed from the colour bar in the image plots. Thus filtered images are enhanced and are ready for the setting and application of the threshold in the next stage of image processing.

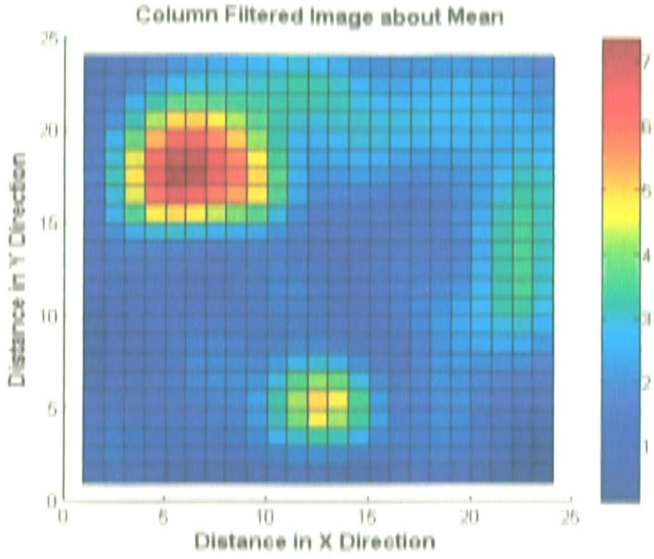

Fig. 4.12. (a) Filtered image using Column filter.

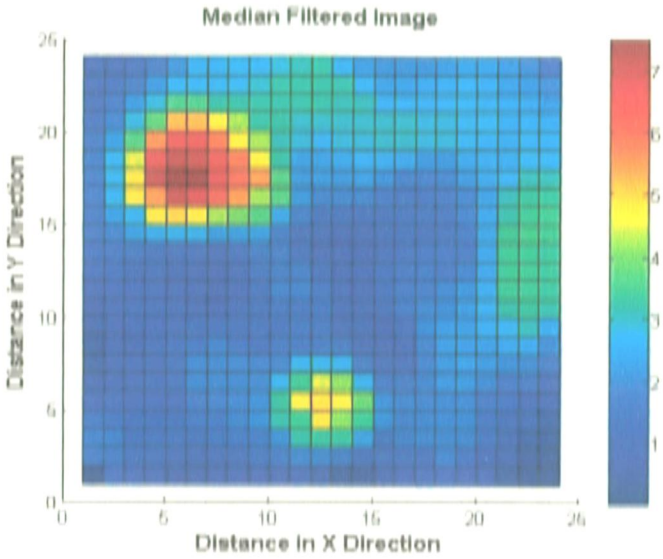

Fig. 4.12. (b) Median filtered image.

The threshold is set based on Otsu and Entropy techniques which are set at 0.349 and 0.621 respectively. It can be clearly seen from Fig. 4.13. (a) and Fig. 4.14. (a) and threshold levels so obtained that entropy threshold technique is more stringent. A total of 154 and 29 pixels were detected in Otsu and Entropy threshold giving the DA of 94.64% and 44.64% and FAR of 18.85% and 0.77%. It can be seen clearly that both the cavity and the metal plate at this depth have been detected and distinguished with reasonably high accuracy.

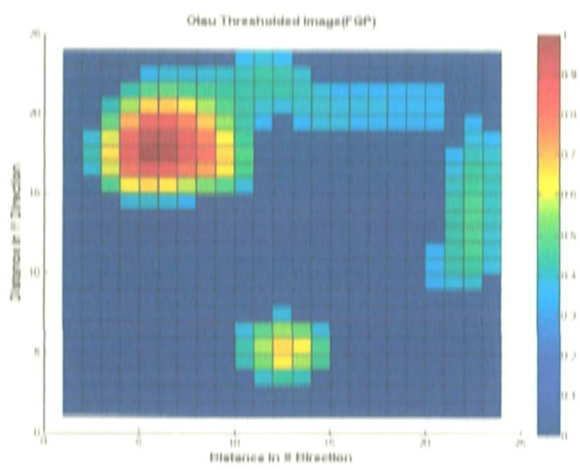

Fig. 4.13. (a) Otsu threshold image (FGP).

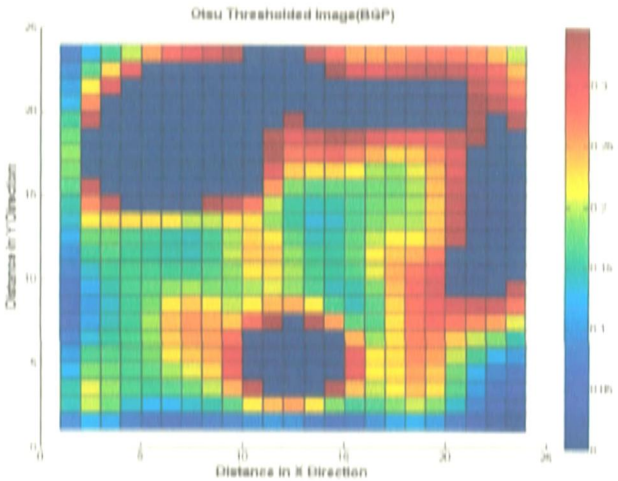

Fig. 4.13. (b) Otsu threshold image (BGP).

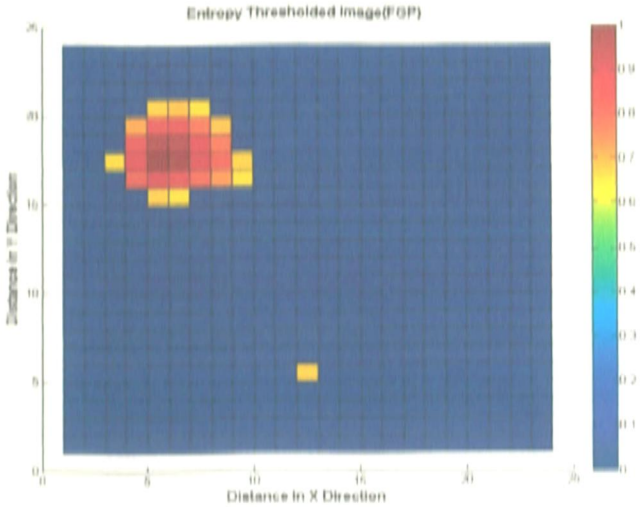

Fig. 4.14. (a) Entropy threshold image (FGP).

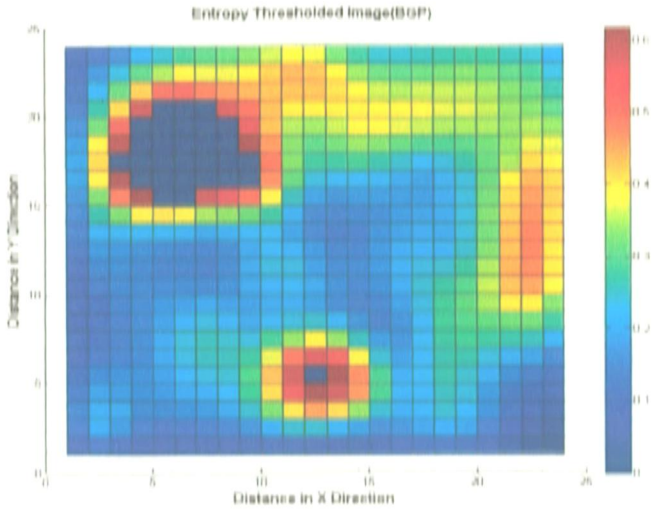

Fig. 4.14. (b) Entropy threshold image (BGP).

4.1.6 Inverted Cavity with Triangular Metal Plate Buried at 1 cm Depth The cavity and triangular metal plate were buried at the depth of 1 cm and the observations were carried out with HH polarization as mentioned in Ser No 6 of Table 4.1.

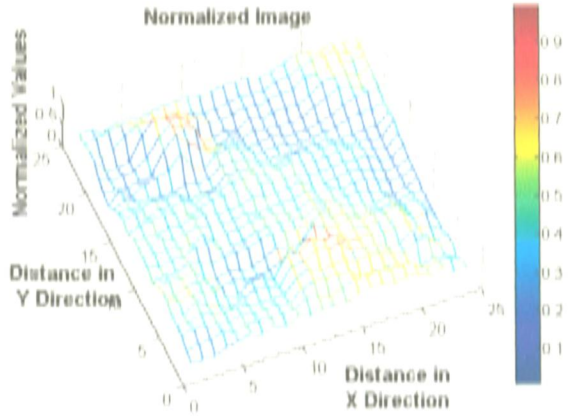

Fig. 4.15. Normalized 3D plot.

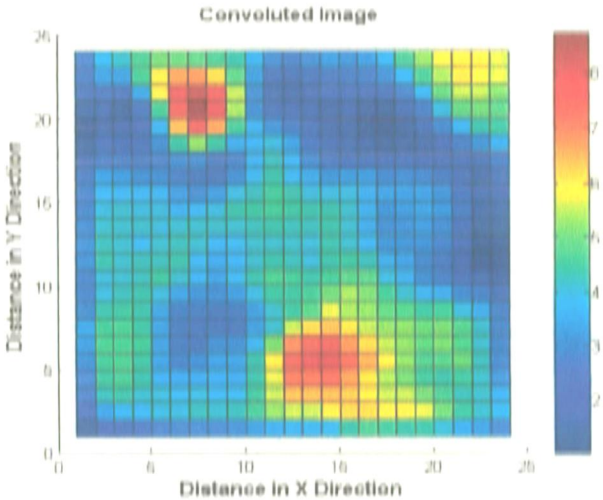

Fig. 4.16. Convoluted image.

The resultant of the preprocessed image after calibration and normalization is shown in Fig. 4.15. which points towards two bright regions indicating the presence of targets. However definite information about the target cannot be inferred at this stage. The normalized image is then subjected to the next level of processing in the sequence.

The convolution is carried out using the 3 × 3 convolution kernel. The image plot of the convoluted data is shown in Fig. 4.16. which shows three clusters, two of which are towards higher range while one cluster is towards the lower range. The convoluted image is in the range of 0-8.5 in this case.

To achieve tangible information from this data set the process of filtration is carried out using the two techniques. From the filtered image plots seen in Fig. 4.17. (a), (b) it can be seen that the third group of blue coloured pixels have been elevated and hence merged with the background thereby eliminating the chances of confusing this group being a desired target. Thus the filtered images are ready for threshold and detection.

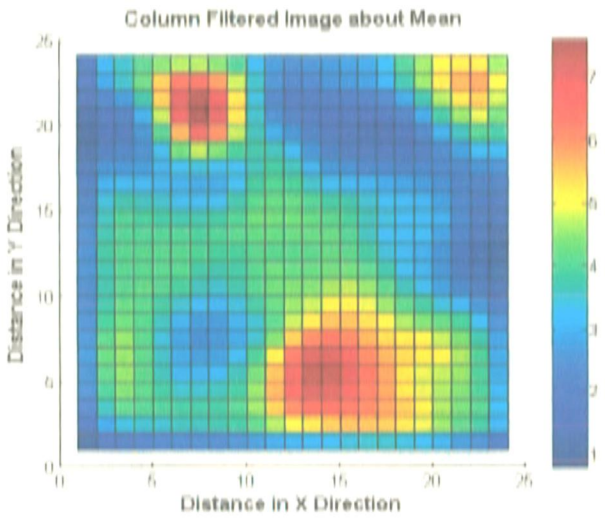

Fig. 4.17. (a) Filtered image using Column filter.

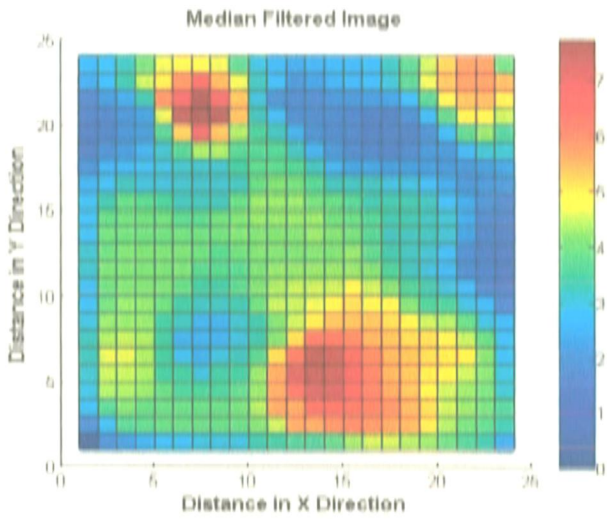

Fig. 4.17. (b) Median filtered image.

On application of the threshold 288 pixels were detected in Otsu technique achieving the DA of 97.5% with a high FAR of 46%. Similarly with Entropy threshold 222 pixels are detected to provide a DA of 97.5% and FAR of 44%. Thus in this iteration maximum FAR has been found at this depth.

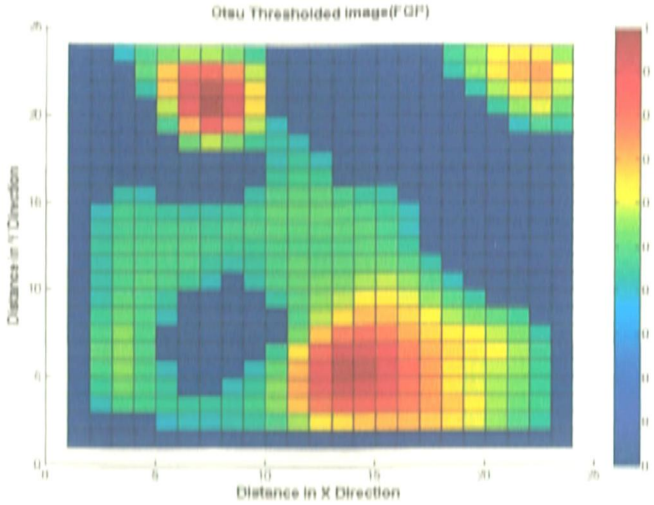

Fig. 4.18. (a) Otsu threshold image (FGP).

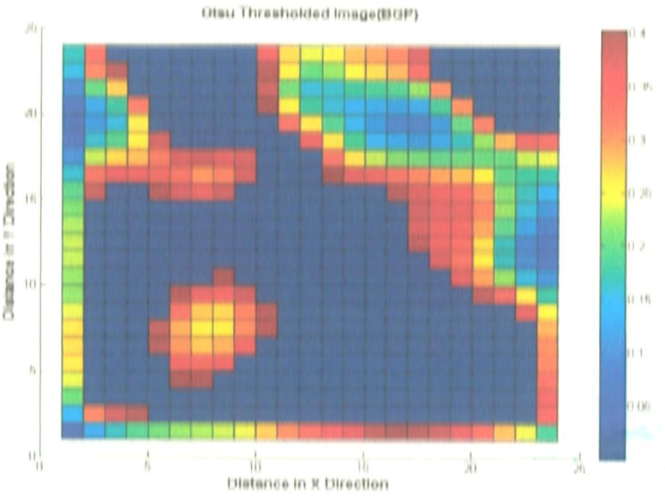

Fig. 4.18. (b) Otsu threshold image (BGP).

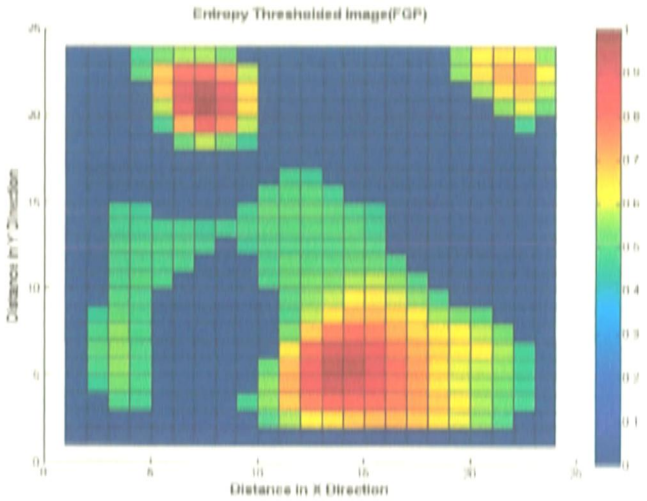

Fig. 4.19. (a) Entropy threshold image (FGP).

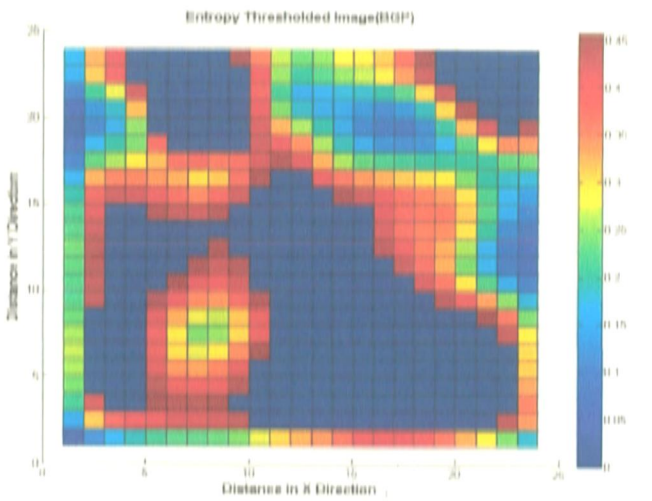

Fig. 4.19. (b) Entropy threshold image (BGP)

4.1.7 Inverted Cavity with Triangular Metal Plate Buried at 1 cm Depth The cavity and metal plate ' were buried at the depth of 1 cm and the observations are carried out with VV polarization as mentioned in Ser No 7 of Table 4.1.

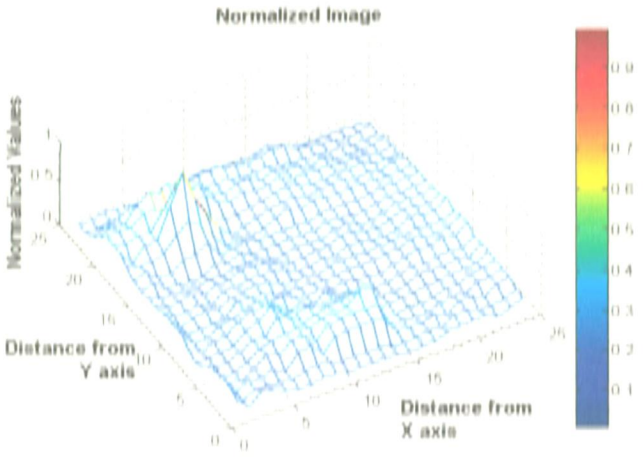

Fig. 4.20. Normalized 3D plot.

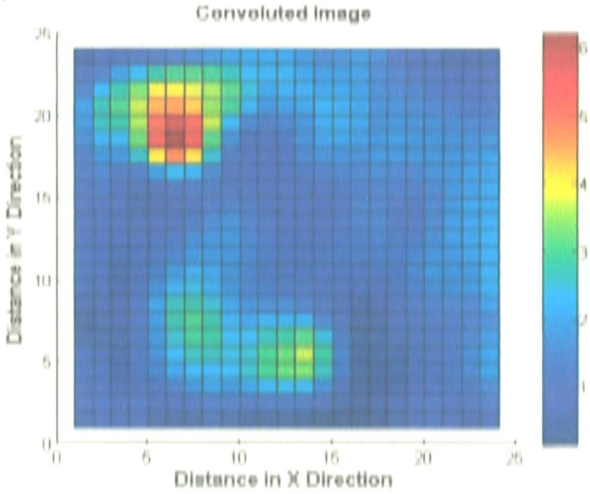

Fig. 4.21. Convoluted image.

On being calibrated and normalized the backscattered data indicates in Fig. 4.20, a reasonably high peak with two lesser dimensioned peaks lying adjacent to each other.

Convolution is carried out next in the processing sequence. The only discernible information from Fig. 4.21. is that the bright red coloured cluster of pixels might be that of the metal plate for its high reflectivity. The convoluted image is then filtered with both the techniques. The range of values in case of filtered images has dropped to 0-5 when compared to 0-6 of the convoluted image plot.

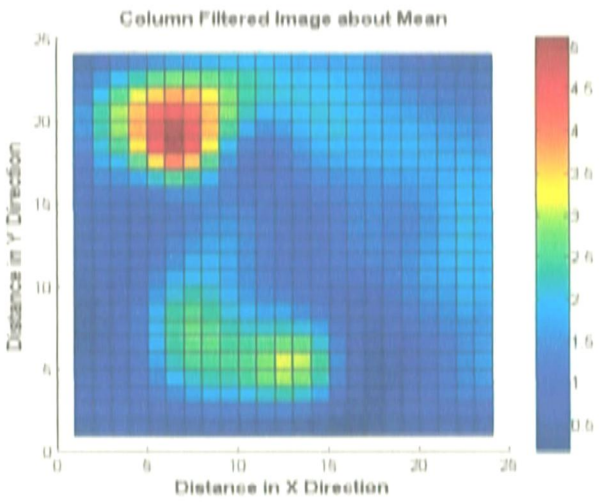

Fig. 4.22. (a) Column filtered image.

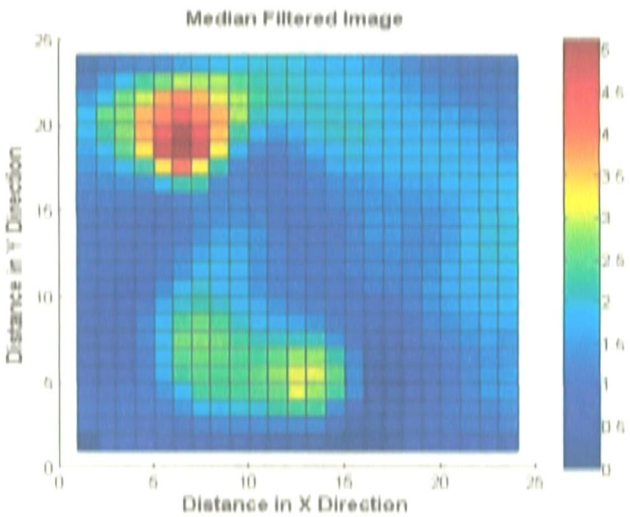

Fig. 4.22. (b) Median filtered image.

The stage is now set for setting the threshold and comparing the image pixels with the threshold to carry out the detection of the desired targets. A total 115 pixels were detected in Otsu thresholding as seen in Fig. 4.23. (a)with the DA of 100% and FAR of 13.98%. Similarly using entropy thresholding a total of 28 pixels were accurately detected with DA of 70% and FAR of 0%. Hence the cavity and metal plate are both detected in the Otsu threshold while in Entropy threshold the cavity pixels fall on the borderline and can be seen in FGP image and BGP image, Fig. 4.24. (a), (b).

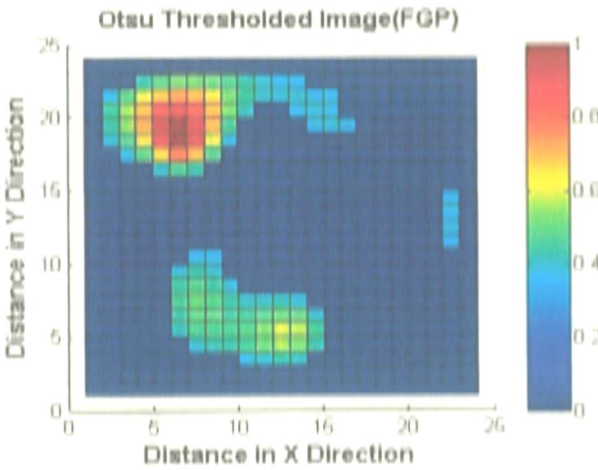

Fig. 4.23. (a) Otsu threshold (FGP).

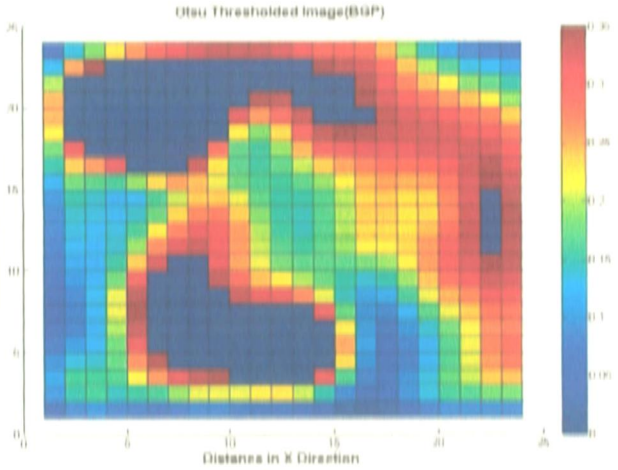

Fig. 4.23. (b) Otsu threshold (BGP).

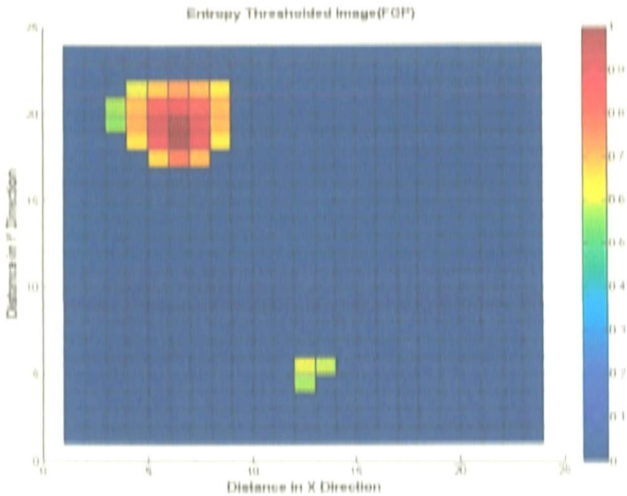

Fig. 4.24. (a) Entropy threshold (FGP).

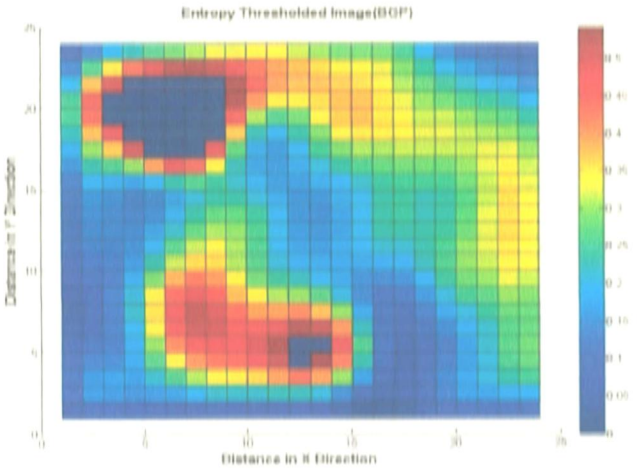

Fig. 4.24. (b) Entropy threshold (BGP).

. It can be observed from these results for cavity and object buried at 1cm depth that both the cavity and object are detected and distinguished with Otsu threshold with reasonable

DA and low FAR. The only exception is of triangular metal plate wherein the FAR is high. However with entropy threshold few cavity pixels are visible due to high threshold value but FAR is low.

The received power levels and statistics involved with the threshold images for the iterations carried out at 1 cm depth have been tabulated in Table 4.2 below

Table 4.2 Power values and threshold statistics for different objects at 1 cm depth.

SER NO	TGT	POL	DEPTH	UNCAL POWER			CAL POWER			THRESHOLD LEVEL a (Otsu) b (Entropy)	DET FIG	NO OF PIXELS	DETECTION ACCURACY (DA) IN %	FALSE ALARM RATE(FAR) IN %
				AVG	MAX	MIN	AVG	MAX	MIN					
1.	Sq Plate	HH	1 cm	-14.96	-10.91	-18.12	0.1034	0.25	.0482	0.3569 a	104.42	146	100	17.31
										0.7063 b	206.18	18	32.14	0
2.	Sq Plate	VV	1 cm	-15.43	-10.48	-18.88	0.173	0.5082	0.0735	0.349 a	105.57	154	94.64	18.85
										0.621 b	190.57	29	44.64	0.77
3.	Tri Plate	HH	1 cm	-14.76	-12.04	-17.86	0.1073	0.1952	0.0512	0.4839 a	77.22	288	97.5	46
										0.4584 b	78.27	222	97.5	44
4.	Tri Plate	VV	1 cm	-16.13	-9.84	-19.47	0.1468	0.5888	0.0641	0.3510 a	116.15	115	100	14
										0.549 b	188.53	28	70	0

* TGT : Target Buried with cavity ; POL: Polarization ; UNCAL and CAL : Received Power and Calibrated Received Power respectively ;

AVG : Average ; MAX: Maximum ; MIN: Minimum ; DET FIG : Detection Figure; Sq : Square ; Tri : Triangle

4.1.8 Inverted Cavity with Square Metal Plate Buried at 5 cm Depth The cavity and metal plate (in this instance square plate) were buried at the depth of 5 cm and the observations are carried out with HH polarization as mention in Ser No 8 of Table 4.1. On completing the preprocessing as per the flow chart in Fig. 3.7 the normalized image is obtained as shown in Fig. 4.25 showing a solitary peak. Carrying on further enhancement the convoluted image in Fig. 4.26 also indicates a high intensity variation but it is difficult to infer the target.

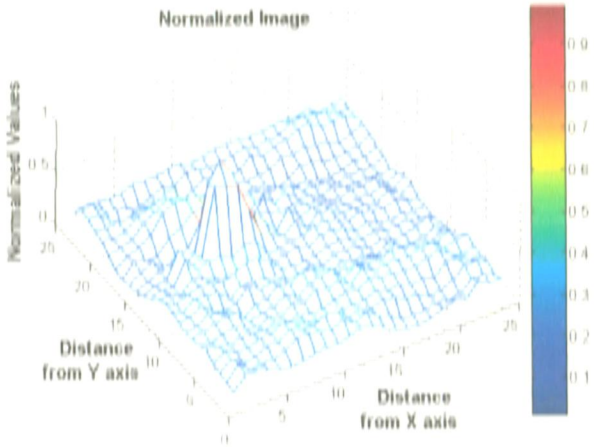

Fig. 4.25. Normalized 3D plot.

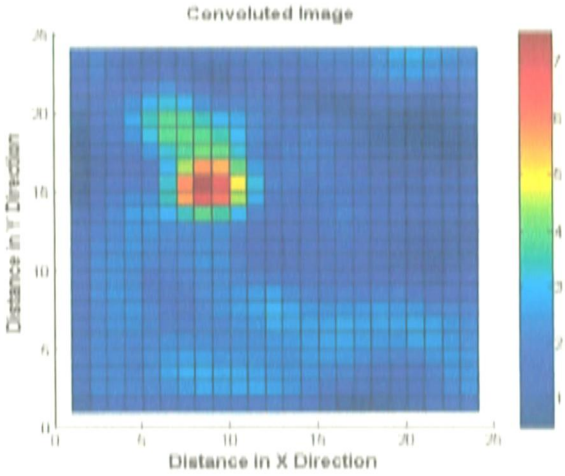

Fig. 4.26. Convoluted image.

To enhance the target information filter, columnwise filter about mean and median filter are applied to the convoluted image. On comparing the convoluted image in Fig. 4.26. with the filtered images in Fig. 4.27. (a), (b) we can observe the presence of buried objects (cluster of red color and pale green color pixels). It is observed that the range of value in unfiltered is from 0-8 while that of filtered images if from 0-6.

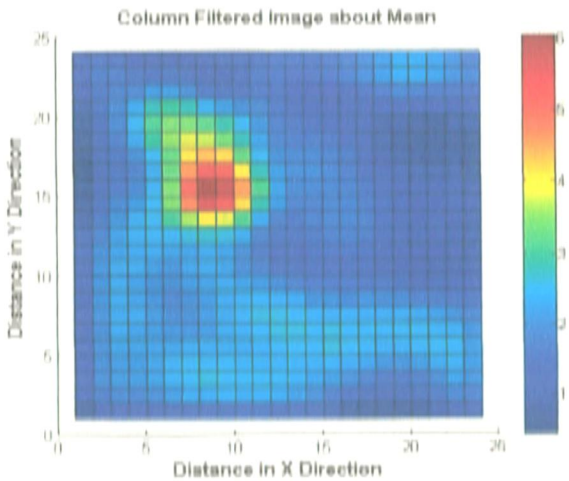

Fig. 4.27. (a) Column filtered image.

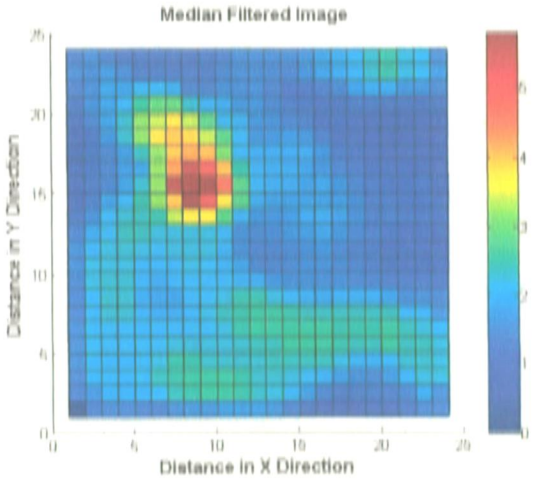

Fig. 4.27. (b) Median filtered image.

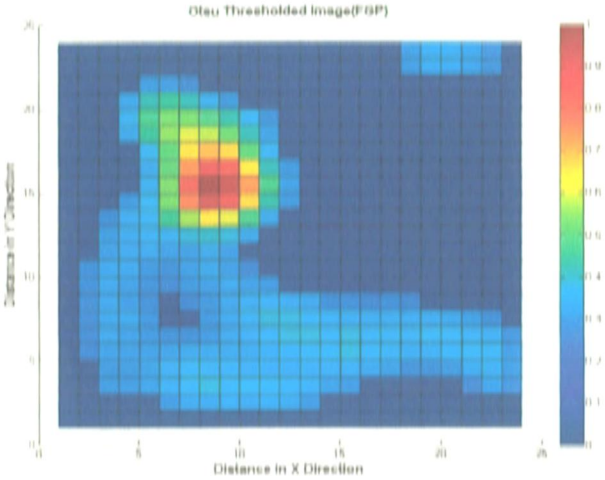

Fig. 4.28. (a) Otsu threshold (FGP).

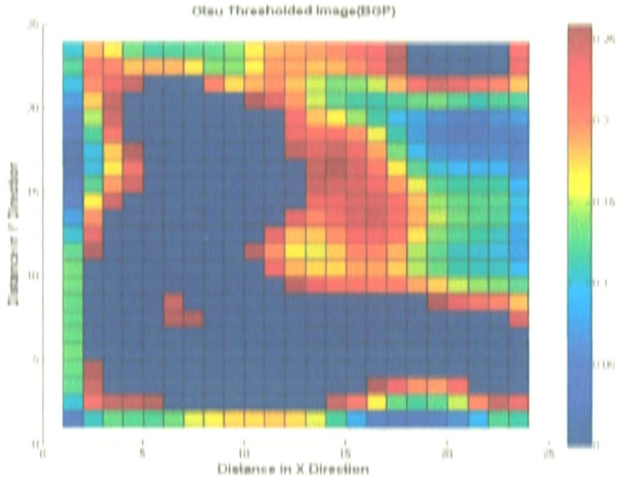

Fig. 4.28. (b) Otsu threshold (BGP).

Further to segregate the target Otsu and Entropy threshold techniques are applied. From the Otsu threshold technique in Fig. 4.28. (a) a total of 234 pixels were detected in which the metal target has been clearly identified which is ratified by the Entropy FGP image, Fig. 4.29. (a) wherein only 13 pixels have been detected. The cavity pixels have also been rightly identified in Fig. 4.28. (a) and can be seen in Fig. 4.29. (b) as yellow pixels giving a DA of 100% and 94% with high FAR of 34.23% and 0% for the two threshold techniques.

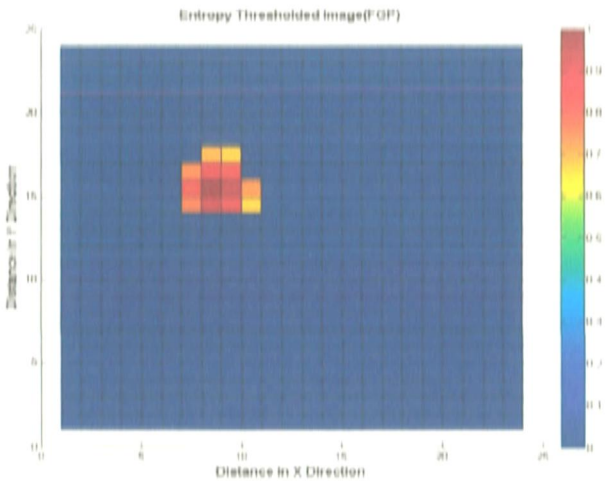

Fig. 4.29. (a) Entropy threshold (FGP).

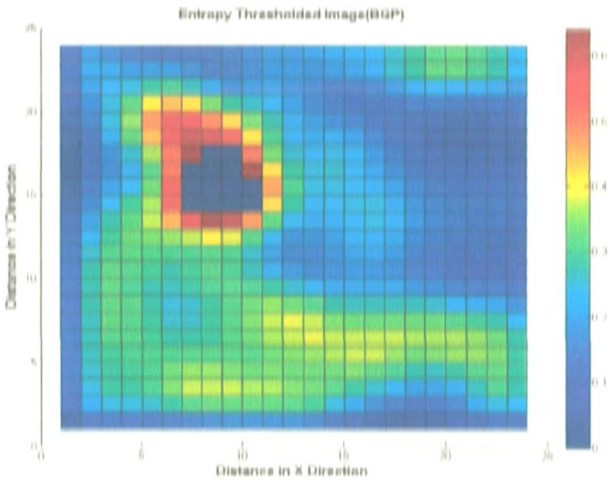

Fig. 4.29. (b) Entropy threshold (BGP).

4.1.9 Inverted Cavity with Square Metal Plate Buried at 5 cm Depth The cavity and metal plate (in this instance square plate) were buried at the depth of 5 cm and the observations are carried out with VV polarization as marked in Ser No 9 of Table 4.1. The preprocessing was carried out by calibrating the data with the metal plate and then normalizing it to bring the data into range as can be seen in Fig. 4.30. where a single peak of metal plate with high reflectivity is seen with few small peaks.

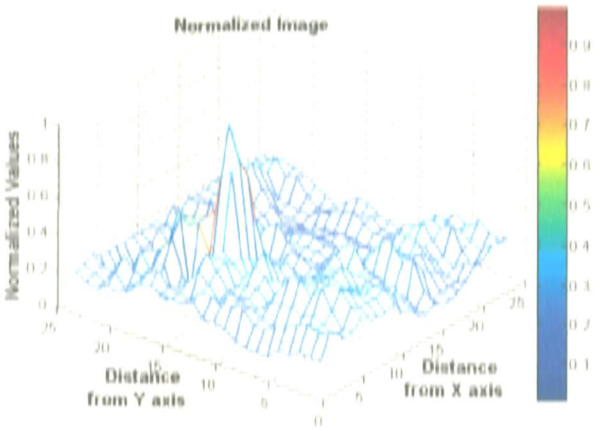

Fig. 4.30. Normalized 3D plot.

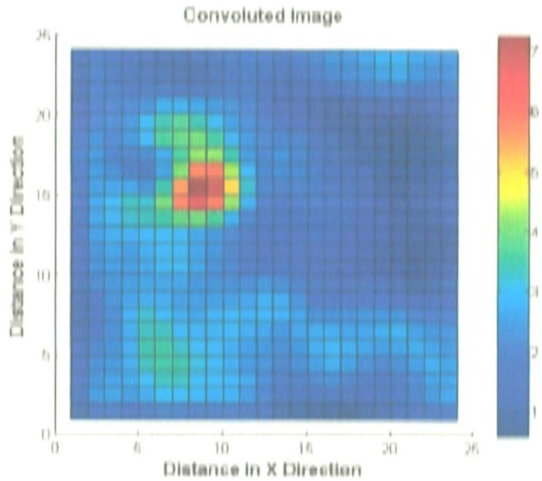

Fig. 4.31. Convoluted image.

In the step of image enhancement the normalized data was convoluted. Only one group of red pixels indicating high reflectivity returns from metal are clearly visible. To enhance the information of the target the two filters were applied. On comparing the convoluted and filtered images from Fig. 4.31. and Fig. 4.32.(a), (b) we can see the target better identified in the latter. The range of data has dropped to 0-6 in the filtered images.

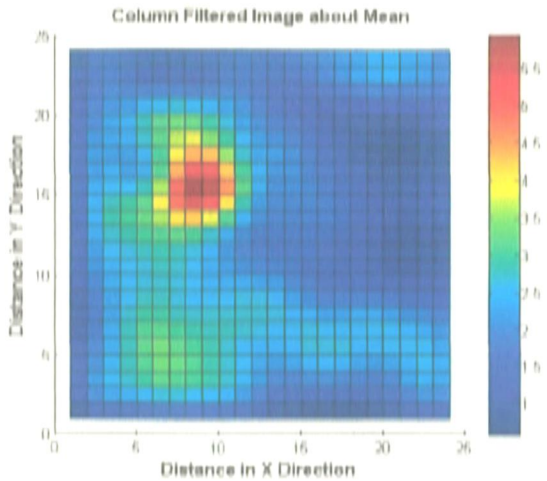

Fig. 4.32. (a) Column filtered image.

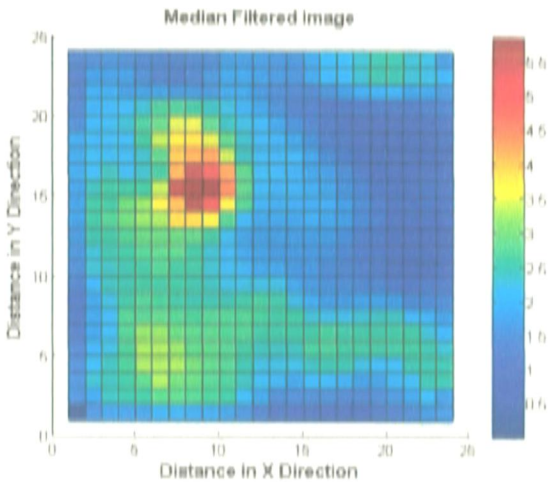

Fig. 4.32. (b) Median filtered image.

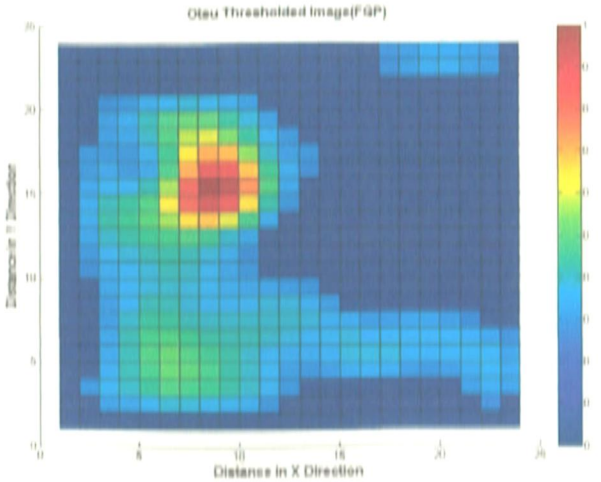

Fig. 4.33. (a) Otsu threshold (FGP).

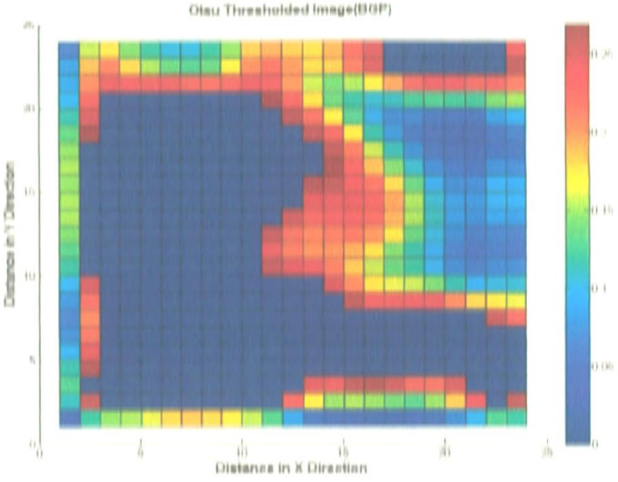

Fig. 4.33. (b) Otsu threshold (BGP).

The filtered images are then used to set the threshold by applying the threshold techniques. A low threshold value of 0.2706 was obtained for the Otsu technique in which a total of 251 pixels were detected a shown in Fig. 4.33. (a) giving a DA of 96.43% with a high FAR of 37.5%. In the entropy technique shown by Fig. 4.3.4 (a) only 16 pixels were detected owing to a high threshold value of 0.625 with DA of 28.57% and 0% FAR. Thought the cavity pixels have been detected accurately but stronger cluster of green pixel is present adjacent to it.

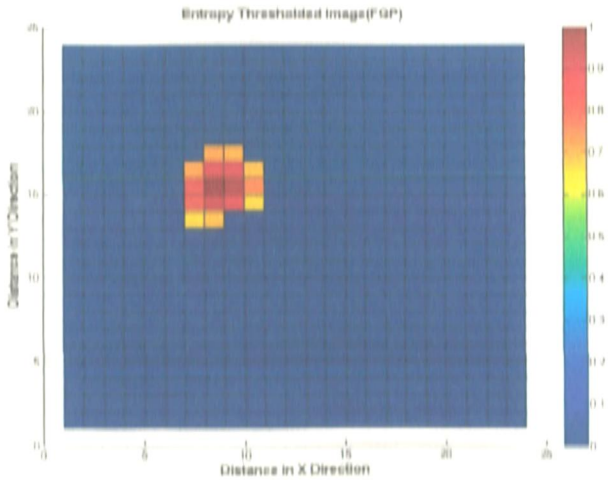

Fig. 4.34. (a) Entropy threshold (FGP).

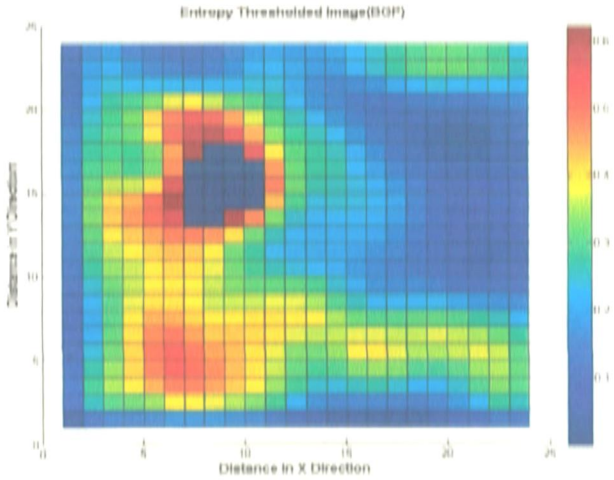

Fig. 4.34. (b) Entropy threshold (BGP).

4.1.10 Inverted Cavity with Triangular Metal Plate Buried at 5 cm Depth In this iteration the cavity and metal plate were buried at a depth of 5 cm below the surface. The metal plate used in the discussion below is a triangular plate with antenna orientation as HH. This image is preprocessed by calibrating with the metal plate reading and normalization for which the 3-D plot is given in Fig. 4.35. Three higher intensity regions can be seen in this plot.

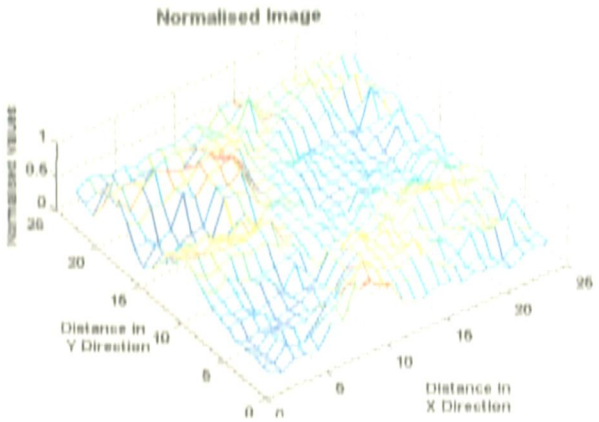

Fig. 4.35. Normalized 3D plot.

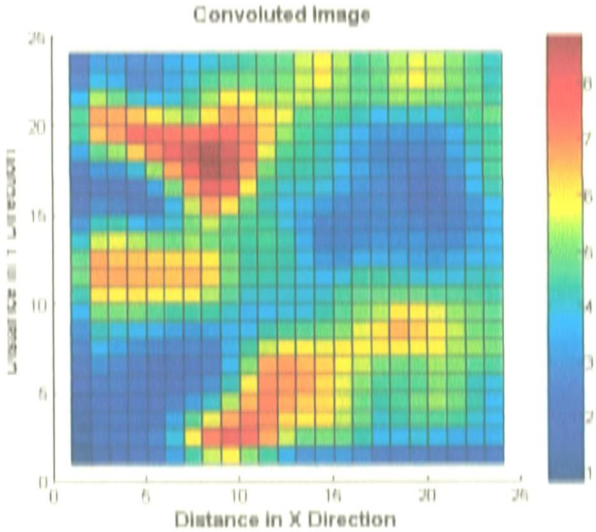

Fig. 4.36. Convoluted image.

To enhance the target information, convolution of the normalized data is carried out as shown in Fig. 4.36. wherein higher intensity variation is clearly visible but it is difficult to infer the kind of target at this stage. The column filter about the mean value and median filters are then used to minimize the noise as can be seen in Fig. 4.37. (a) and 4.37. (b) respectively. The range of filtered values has reduced to 0-8 in the filtered image from 0-9 in the convoluted image.

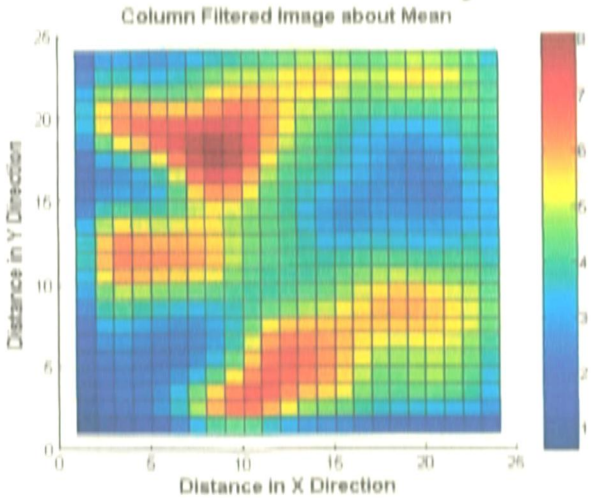

Fig. 4.37. (a) Column filtered image.

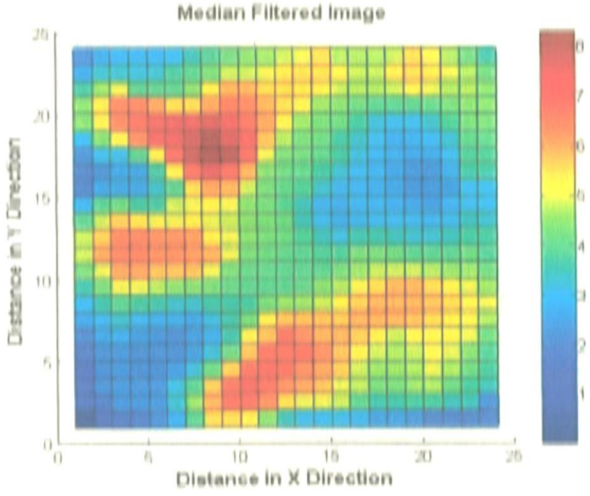

Fig. 4.37. (b) Median filtered image.

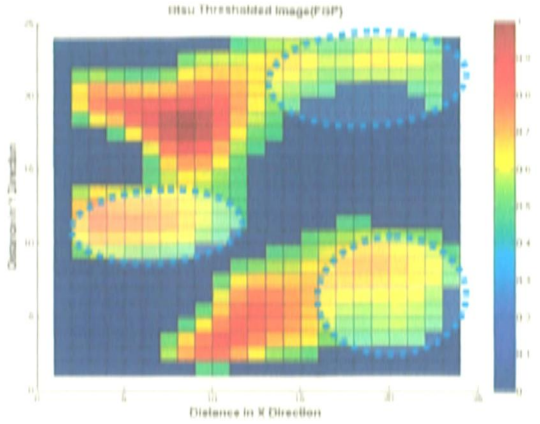

Fig. 4.38. (a) Otsu threshold (FGP).

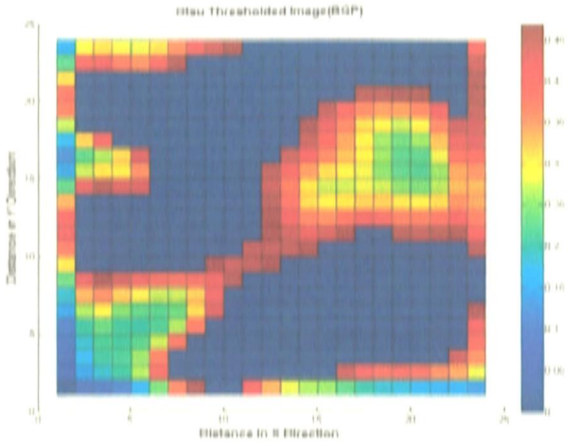

Fig. 4.38. (b) Otsu threshold (BGP).

This smoothened image is then subjected to thresholding with the same techniques as used in previous section. With the Otsu threshold image 282 pixels were detected as against 44 actual pixels (20 for the cavity and 24 for the plate). DA of 100% and FAR of 45.16 % has been achieved for Otsu Threshold while for 202 detected pixels Entropy threshold the values lay at 90% and 30.22%. It can be seen that as the DA is increasing the FAR is also increasing. However both the cavity and the metal plate pixels have been detected with reasonable accuracy.

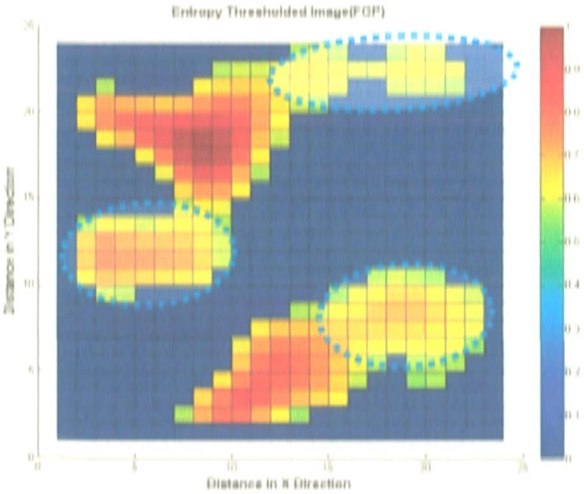

Fig. 4.39. (a) Entropy threshold (FGP).

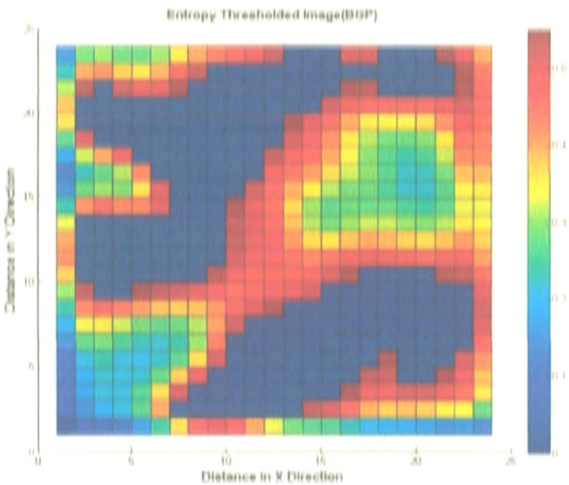

Fig. 4.39. (b) Entropy threshold (BGP).

4.1.11 Inverted Cavity with Triangular Metal Plate Buried at 5 cm Depth The cavity and metal plate were buried at the depth of 5 cm and the observations are carried out with VV polarization as mentioned in Ser No 11 of Table 4.1. The preprocessed image is shown in Fig. 4.40. after calibrating with the metal plate and normalizing the reading. Two peaks are visible of varying intensities indicating the presence of higher reflectivity

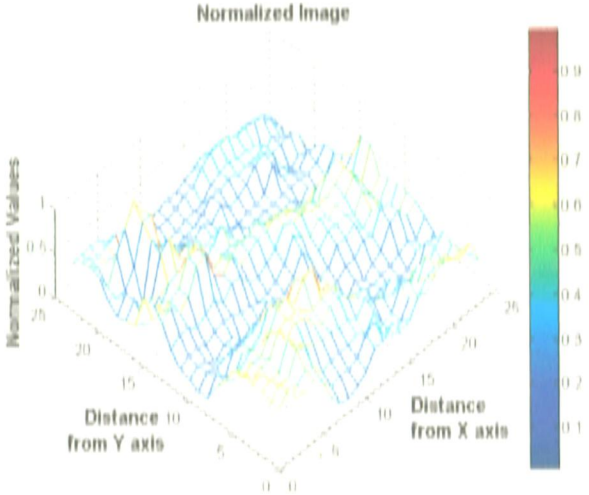

Fig. 4.40. Normalized 3D plot.

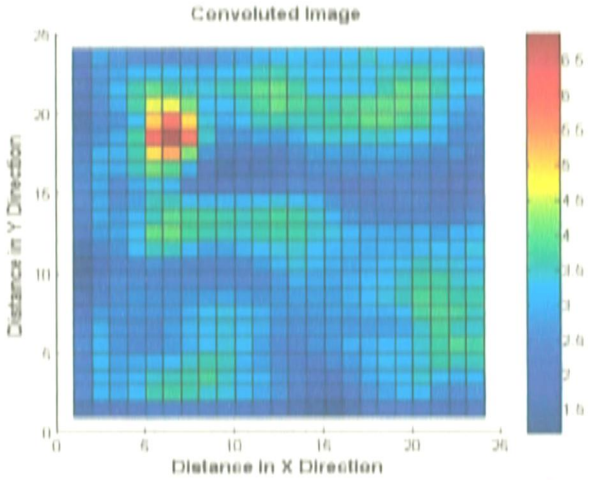

Fig. 4.41. Convoluted image.

To enhance the target information as per the sequence in Fig. 3.7. convolution is carried. The convoluted image in Fig. 4.41. indicates the presence of at least one target but it is difficult to infer about the kind of target. This convoluted image is then processed further with the application of the columnwise filter about the mean and median filter as seen in Fig. 4.42. (a), (b). It can be seen that the level of pixels has been enhanced while the range of values has dropped to 0-6 as compared to the 0-7 in convoluted image.

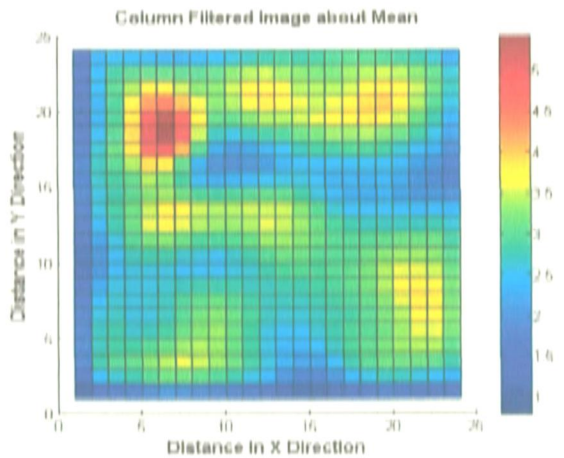

Fig. 4.42. (a) Column filtered image.

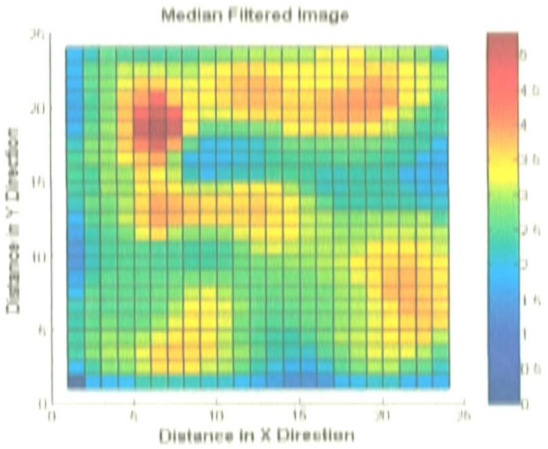

Fig. 4.42. (b) Median filtered image.

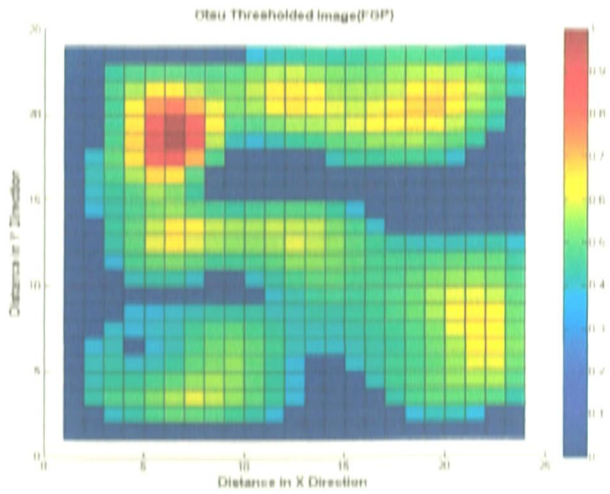

Fig. 4.43. (a) Otsu threshold (FGP).

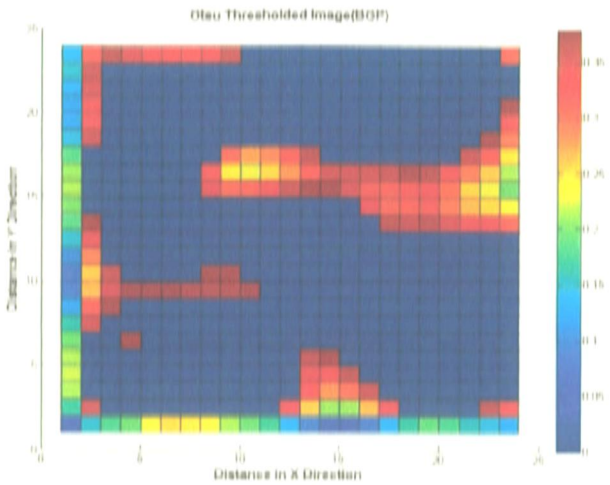

Fig. 4.43. (b) Otsu threshold (BGP).

The threshold is set based on Otsu and Entropy techniques which are set at and respectively. A total of 419 and 318 pixels were detected in Otsu and Entropy threshold giving the DA of 63.63% and 68.2% with FAR of 74% and 53.75%. It can be seen in both the cases that the metal plate pixels have been detected with reasonably high accuracy. However the FAR rates are very high.

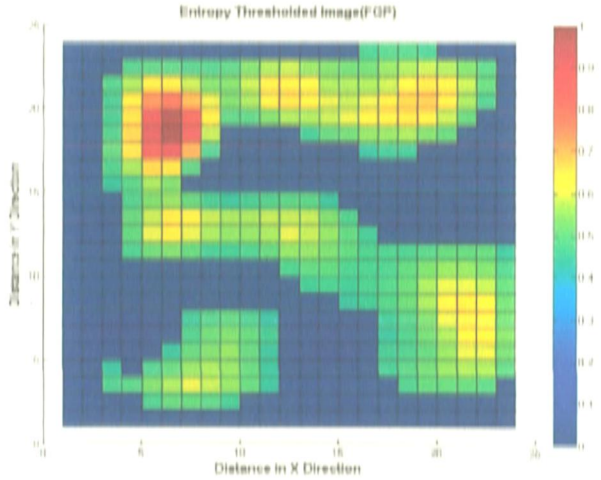

Fig. 4.44. (a) Entropy Threshold (FGP).

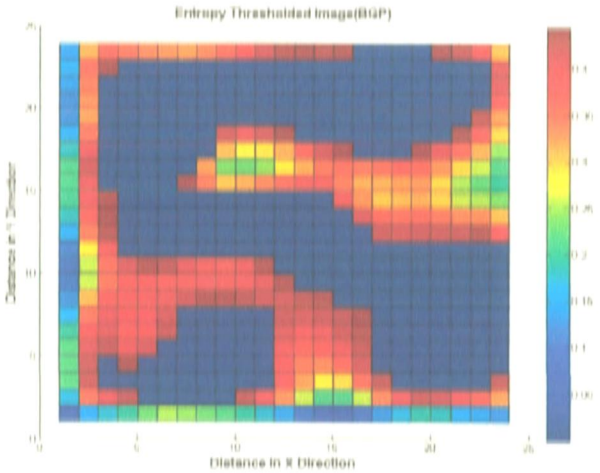

Fig. 4.44. (b) Entropy Threshold (BGP).

At 5cm depth in square metal plate iterations, cavity was detected in HH mode but could not be clearly distinguished while in VV mode wherein only 6 pixels of the cavity were detected while using Otsu threshold. No cavity pixels could be detected using Entropy threshold. In case of the iterations of the triangular metal plate the DA and FAR

are high in HH mode while in the VV mode the DA and FAR have reduced for Otsu threshold. Metal plate detection has been carried out with reasonable accuracy.

The received power levels and statistics involved with the threshold images for the iterations carried out at 5 cm depth have been tabulated in Table 4. 3

Table 4.3 Power values and threshold statistics for different objects at 5 cm depth.

SER NO	TGT	POL	DEPTH	UNCAL POWER (in dBm)			CAL POWER			THRESHOLD LEVEL * a (Otsu) b (Entropy)	DET FIG	NO OF PIXELS	DETECTION ACCURACY (DA) IN %	FALSE ALARM RATE(FAR) IN %
				AVG	MAX	MIN	AVG	MAX	MIN					
1.	Sq Plate	HH	5 cm	-12.34	-7.43	-15.05	0.1975	0.5943	0.1028	0.2588 a	91.81	234	94.64	34.23
										0.6523 b	242.16	13	23.21	0
2.	Sq Plate	VV	5 cm	-12.22	-7.24	-15.53	0.4532	1.3804	0.2046	0.2706 a	100.77	251	43	37.5
										0.625 b	212.75	16	28.57	0
3.	Tri Plate	HH	5 cm	-12.39	-10.44	-14.84	0.1296	0.2972	0.1079	0.4706 a	67.79	282	100	45.16
										0.5515 b	68.75	202	90	30.22
4.	Tri Plate	VV	5 cm	-13.98	-10.73	-17.24	0.31	0.6080	0.138	0.2864 a	93.8	419	63.63	38.14
										0.3272 b	99.54	318	68.20	53.75

4.1.12 Inverted Cavity with Metal Plate at 8 cm Depth The cavity and metal plate (in this instance square plate) were buried at the depth of 8 cm and the observations are carried out with HH polarization as marked in Ser No 12 of Table 4.1. The preprocessing was carried out by calibrating the data with the metal plate and then normalizing it to bring the data into range as can be seen in Fig. 4.45. where a single peak of metal plate with high reflectivity is seen with few small peaks adjacent to it.

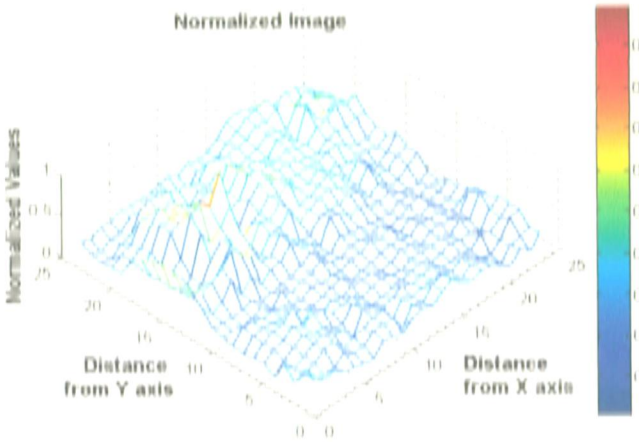

Fig. 4.45. Normalized 3D plot.

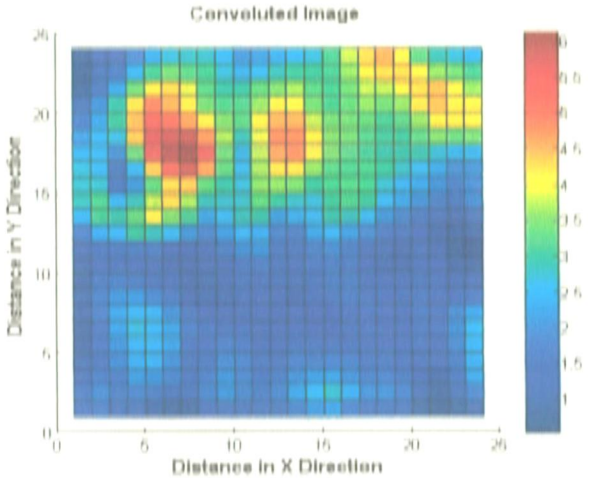

Fig. 4.46. Convoluted image.

The normalized data is then convoluted as described in section 3.2.2 to minimize the effect of neighboring pixels on pixel strength as seen in Fig. 4.46. In this image the higher intensity variation can be easily identified but it is difficult to infer the kind of target. To enhance the target information filter application is required. As discussed the column filter with mean and the median filter have been applied and image plot obtained

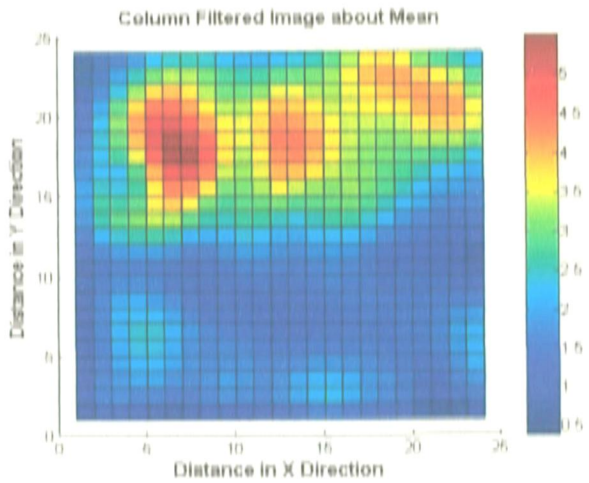

Fig. 4.47.(a) Column filtered image.

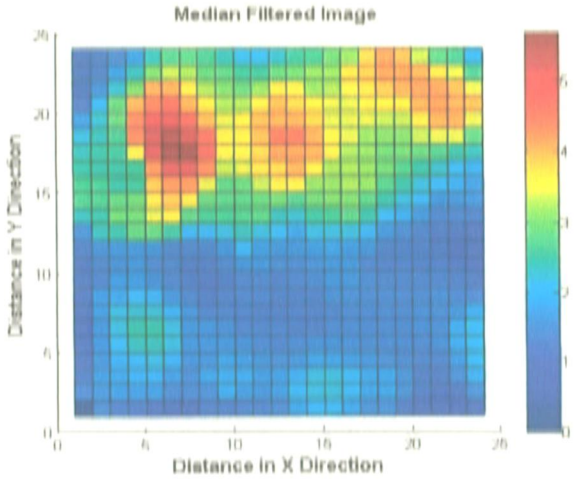

Fig. 4.47.(b) Median filtered image.

as seen in Fig. 4.47. (a), (b). The reduction in the range of values from 0-7 in convoluted image to 0-6 has been observed in the filtered image.

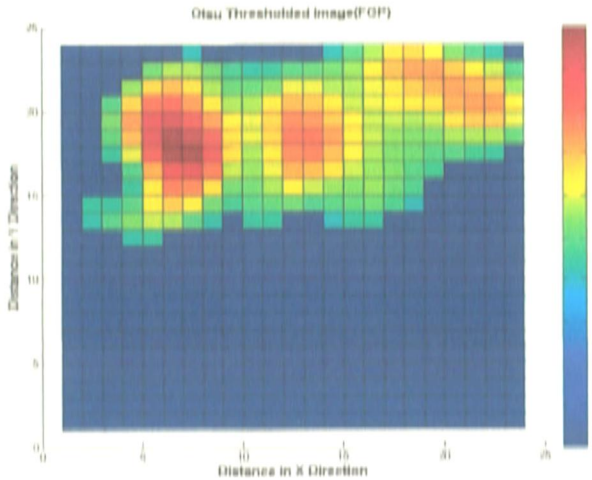

Fig. 4.48. (a) Otsu threshold (FGP).

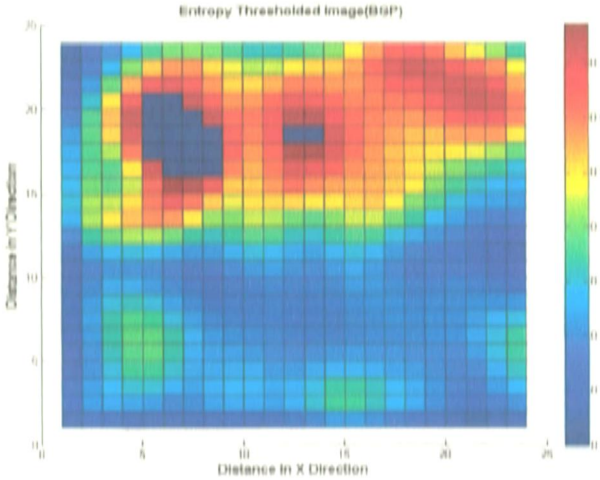

Fig. 4.48. (b) Otsu threshold (BGP).

Further to segregate the target Otsu and Entropy threshold techniques are applied. From the Otsu threshold technique in Fig. 4.48. (a) a total of 194 pixels were detected in which the metal target has been clearly identified which is ratified by the Entropy FGP image, Fig. 4.49. (a) wherein only 18 pixels have been detected. The cavity pixels have been suppressed in both the techniques as seen in Fig. 4.48. (a) and Fig. 4.49. (b). The two images provide DA of 64.31% and 28.57% with high FAR of 30.38% and 0% for the two threshold techniques.

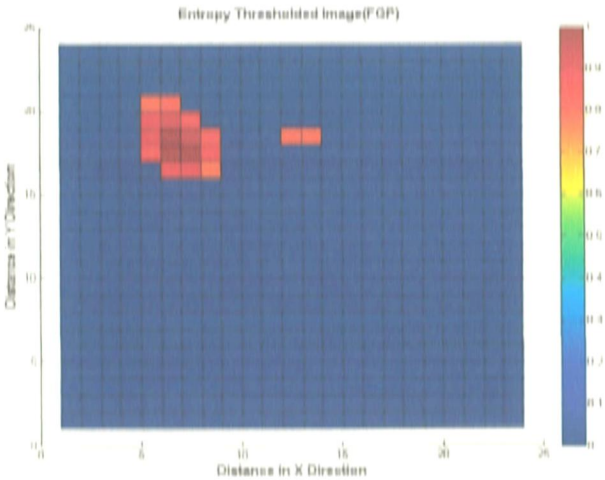

Fig. 4.49. (a) Entropy threshold (FGP).

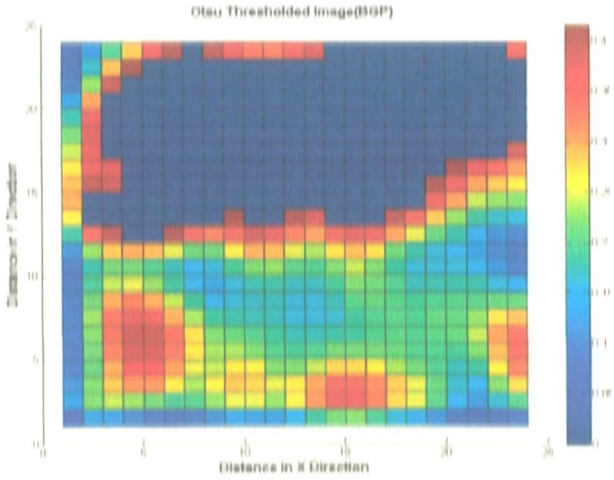

Fig. 4.49. (b) Entropy threshold (BGP).

4.1.13 Inverted Cavity with Square Metal Plate Buried at 8 cm Depth The cavity and metal plate (in this instance square plate) were buried at the depth of 8 cm and the observations are carried out with VV polarization as marked in Ser No 13 of Table 4.1. The preprocessing was carried out by calibrating the data with the metal plate and then normalizing it to bring the data into range as can be seen in Fig. 4.50. where a solitary sharp peak is seen.

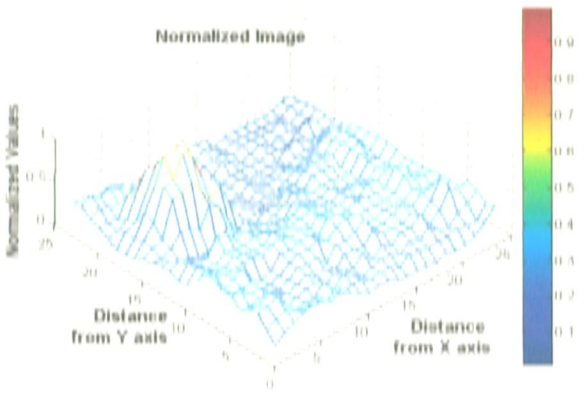

Fig. 4.50. Normalized 3D plot.

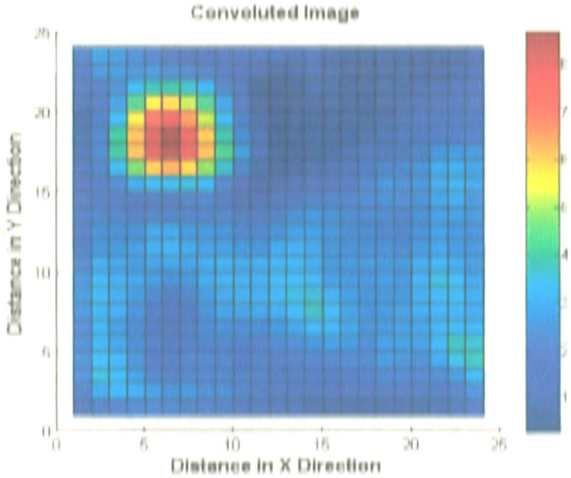

Fig. 4.51. Convoluted image.

The normalized image is then subjected to the next level of processing in the sequence laid out in the Fig. 3.7. The convolution is carried out using the 3 × 3 convolution kernel. The image plot of the convoluted image shown in Fig. 4.51. indicates a single cluster of bright pixels.

To enhance the target information from this data set the process of filtration is carried out using the two techniques. From the filtered image plots seen in Fig. 4.52. (a), (b) only a

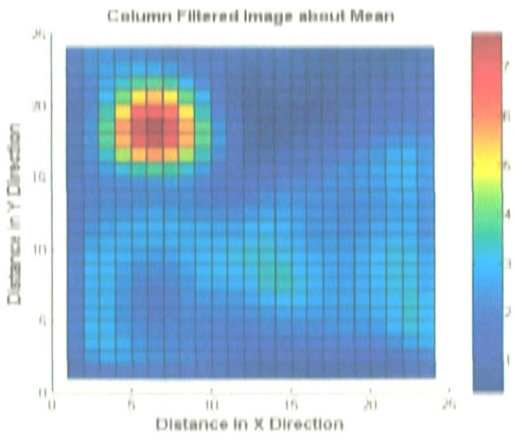

Fig. 4.52. (a) Column filtered image.

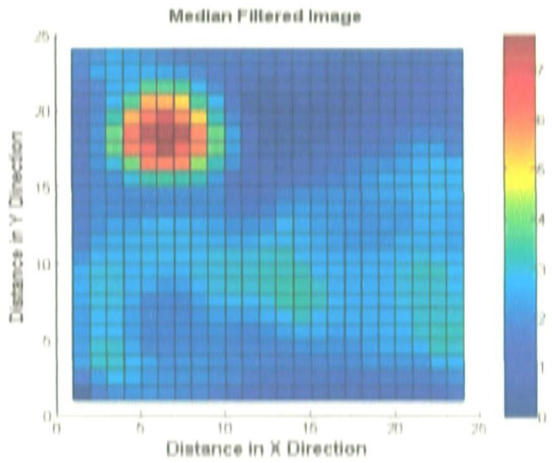

Fig. 4.52. (b) Median filtered image.

single target seems to be present. However post filtering, the range of pixel values has dropped to 0-8 from the 0-9 in the convoluted case. The filtered images are ready for the application of the threshold in the next stage of image processing.

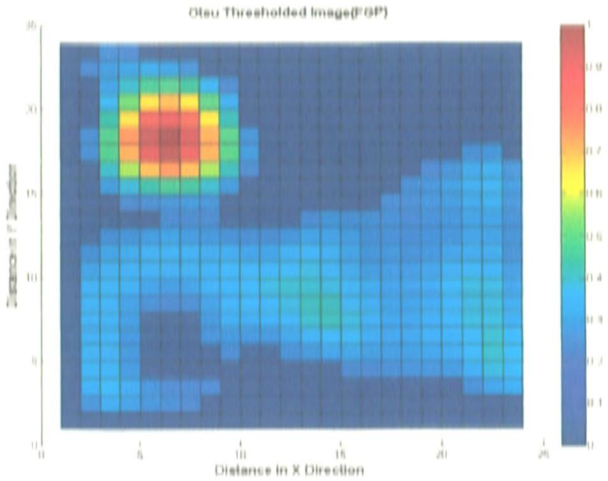

Fig. 4.53. (a) Otsu threshold image (FGP).

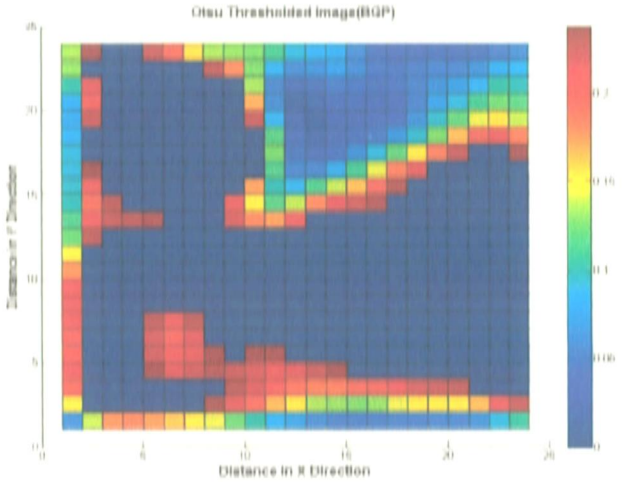

Fig. 4.53. (b) Otsu threshold image (BGP).

The threshold is set based on Otsu and Entropy techniques which are set at 0.2392 and 0.7269 respectively. It can be clearly seen from Fig. 4.53. (a) and Fig. 4.54. (a) and threshold levels so obtained that entropy threshold technique is more stringent. A total of 292 and 11 pixels were detected in Otsu and Entropy threshold giving the DA of 64.28% and 19.64% with FAR of 47.31% and 0%. It can be seen in both the cases that cavity pixels have been suppressed while the metal plate pixels have been detected with reasonably high accuracy.

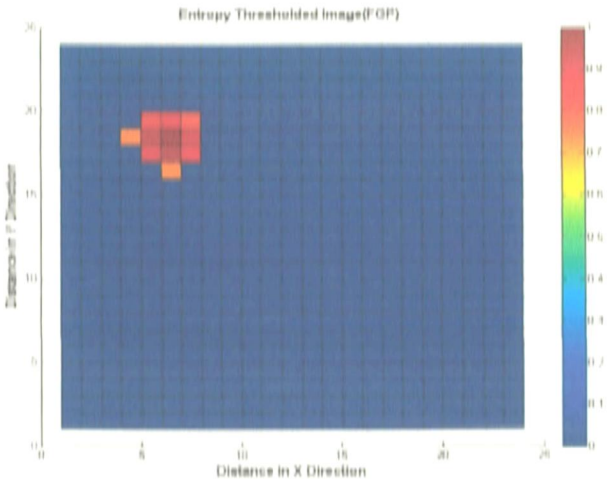

Fig. 4.54. (a) Entropy threshold image (FGP).

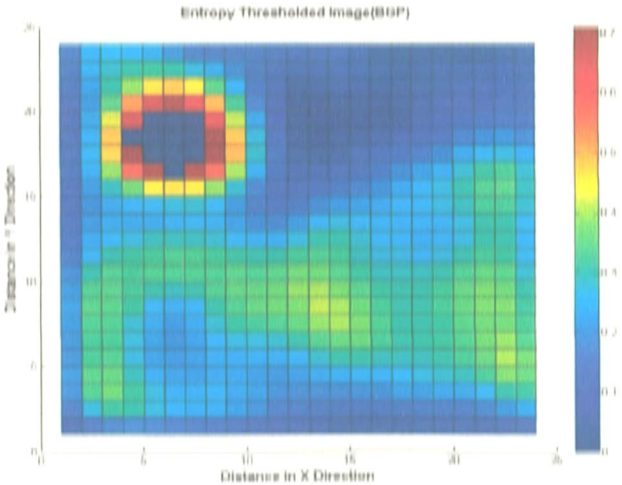

Fig. 4.54. (b) Entropy threshold image (BGP).

4.1.14 Inverted Cavity with Metal Plate Buried at 8 cm Depth In this iteration the triangular plate and cavity buried subsurface at the depth of 8 cm and data collection is carried out in HH orientation, the received power lies in the range of −11.39 to −17.88 dBm. The preprocessed normalized plot shown in Fig. 4.55. indicates the presence of single sharp peak.

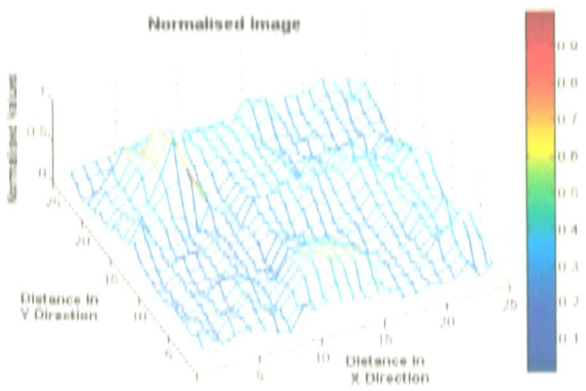

Fig. 4.55. Normalized 3D plot.

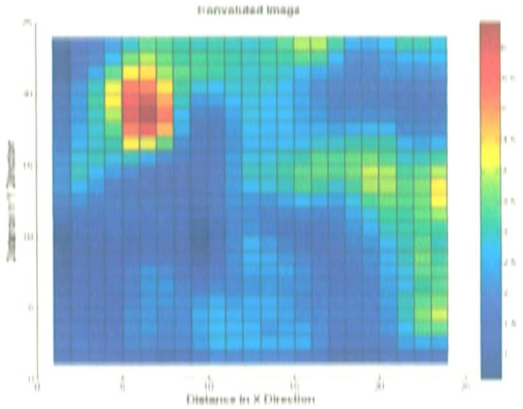

Fig. 4.56. Convoluted image.

This normalized image is then convoluted to minimize the effect of neighboring pixels as a process of image enhancement. In the convoluted image as seen in Fig. 4.56. we are able to view a prominent group of pixels.

Filtering is carried out to improve the target pixel improvement. The columnwise filtered image about the mean and the median filters are used. The two filtered images are shown in Fig. 4.57. (a), (b). Observing the convoluted and filtered images it can be noticed that the boundary pixels in the region of the bright cluster has been enhanced.

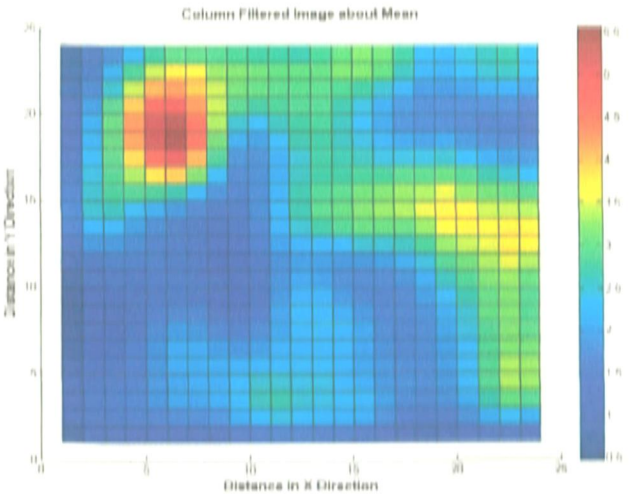

Fig. 4.57. (a) Column filtered image.

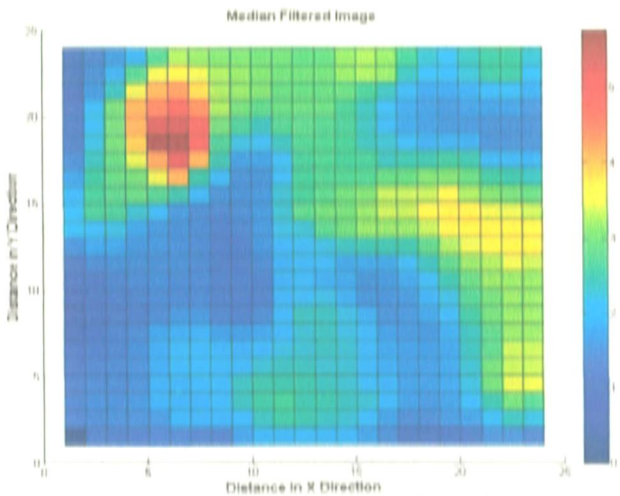

Fig. 4.57. (b) Median filtered image.

The range values of the convoluted image ranges from 0-6.5 while that for filtered images range from 0-5.5 as can be viewed from the colour bar in the image plots. Thus filtered images are enhanced and are ready for the setting and application of the threshold in the next stage of image processing.

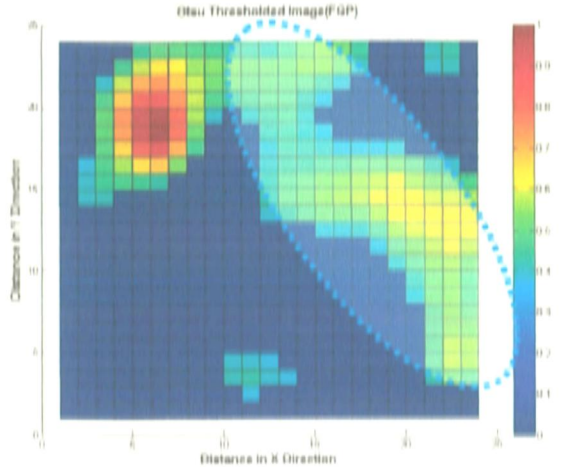

Fig. 4.58. (a) Otsu threshold image (FGP).

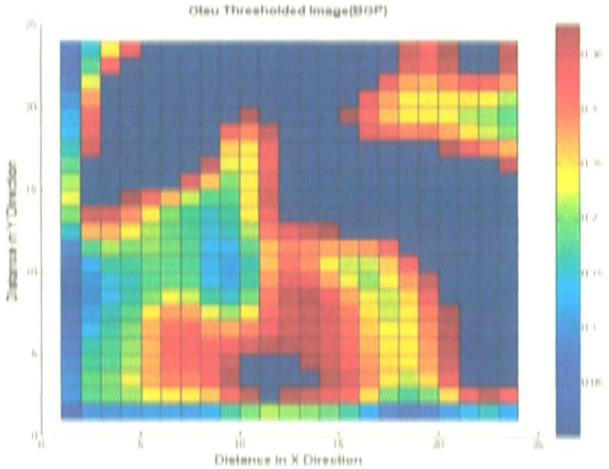

Fig. 4.58. (b) Otsu threshold image (BGP).

The threshold is then applied to the segregate the FGP highlighting the cavity and metal plate. The detection level for Otsu and Entropy threshold is 0.3804 and 0.5965 respectively. The detection accuracy of 57.5% and 40% with FAR of 34.14% and 3.35% were achieved for respective threshold. It can be seen that only 8 of the 20 pixels of the cavity are detected with Otsu threshold. An additional cluster of pixels is formed which has levels between the metal plate and the cavity.

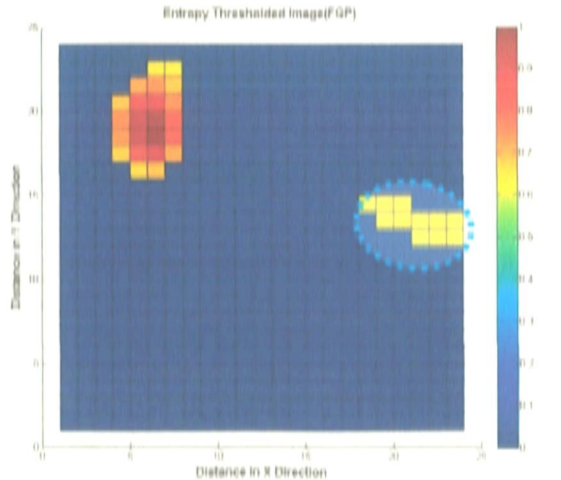

Fig. 4.59.(a) Entropy threshold image (FGP).

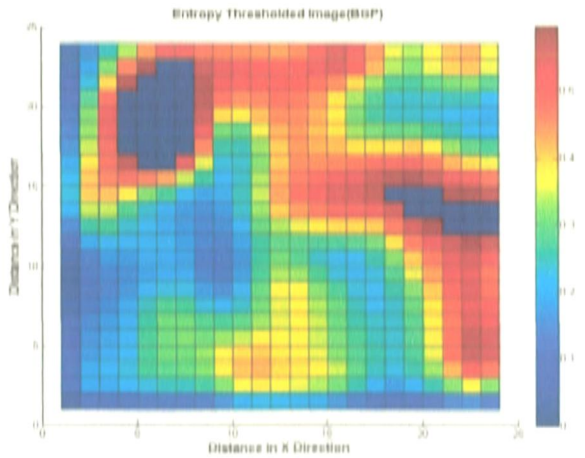

Fig. 4.59.(b) Entropy threshold image (BGP).

No pixel of the cavity is detected in the Entropy threshold FGP, however we can detect the metal plate in the FGP in Entropy threshold image Fig. 4.16. (a). Also seen in the former image is a cluster of yellow pixels which is a false alarm. It is seen that the detection accuracy at the greater depth has reduced for the cavity as well as the metal plate while the FAR has increased.

4.1.15 Inverted Cavity with Triangular Metal Plate Buried at 8 cm Depth In this iteration the triangular plate and cavity buried subsurface at the depth of 8 cm and data collection is carried out VV orientation of the antenna as given in Ser No 15 of Table 4.1. On being calibrated and normalized the backscattered data indicates in Fig. 4.59, a high peak with another lesser dimensioned peaks.

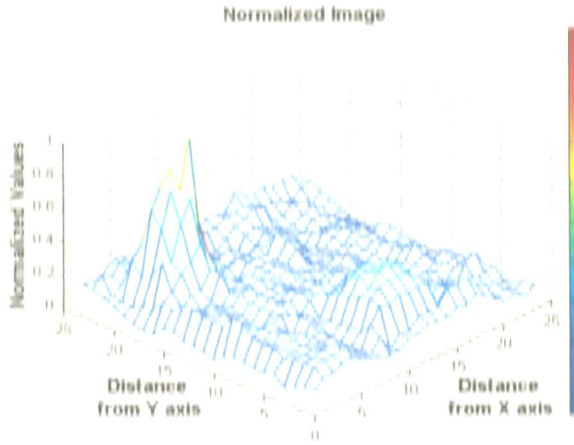

Fig. 4.60. Normalized 3D plot.

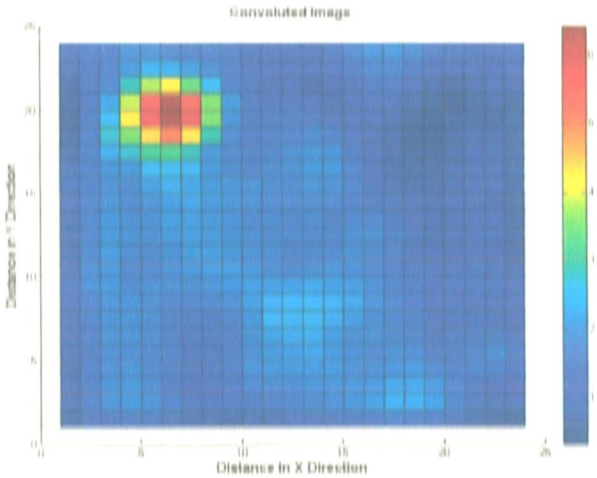

Fig. 4.61. Convoluted image.

Convolution is carried out next in the processing sequence. The only discernible information from Fig. 4.60, is that the bright red coloured cluster of pixels might be that of the metal plate for its high reflectivity. To enhance the target data the convoluted image is then filtered with both the techniques as shown in Fig. 4.61. (a), (b). The range of values in case of filtered images has dropped to 0-5 to 0-6 of the convoluted image plot when the convoluted and filtered image plots are compared. Thus the filtered images are ready for the next stage of image processing where the threshold will be calculated and detection carried out.

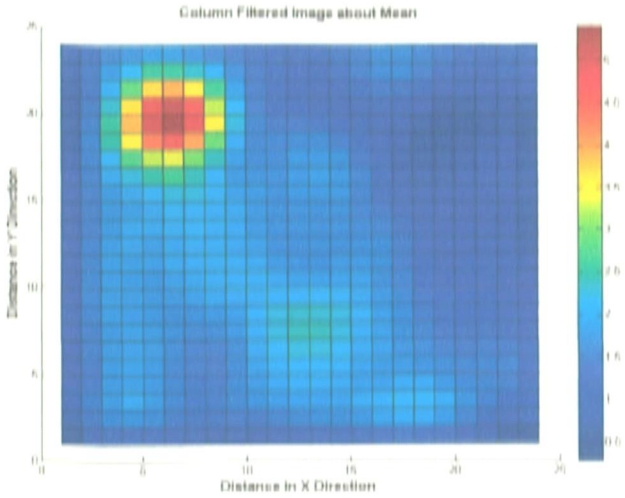

Fig. 4.62. (a) Column filtered image.

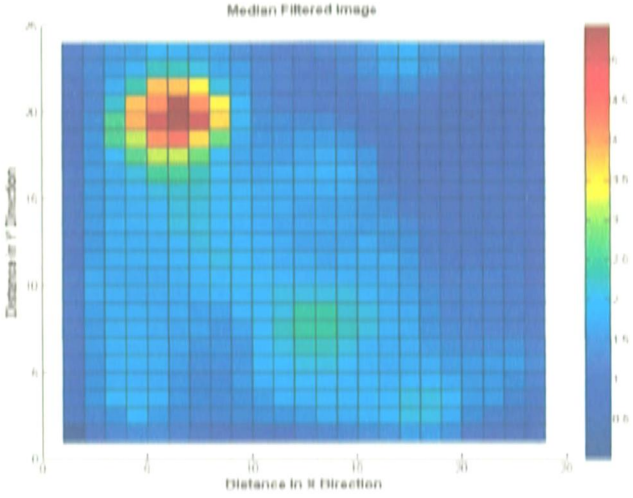

Fig. 4.62. (b) Median filtered image.

With the Otsu threshold image 287 pixels are detected as against 44 actual pixels (20 for the cavity and 24 for the plate). DA of 100% and FAR of 46.1 % has been achieved for Otsu Threshold. Both the metal plate and cavity pixels have been detected but due to high FAR it is difficult to segregate the cavity pixels from the neighbors. Only 11 pixels have been detected in Entropy threshold giving a DA of 20% with FAR of 0.56%. The cavity pixels have totally been suppressed due to high threshold value. It can be seen that as the DA is increasing the FAR is also increasing.

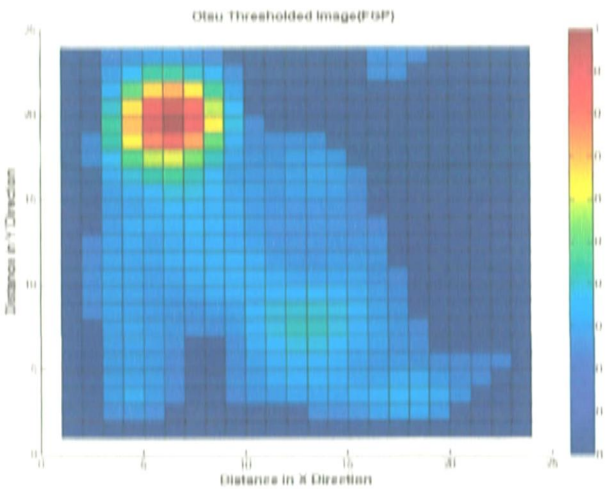

Fig. 4.63. (a) Otsu threshold image (FGP).

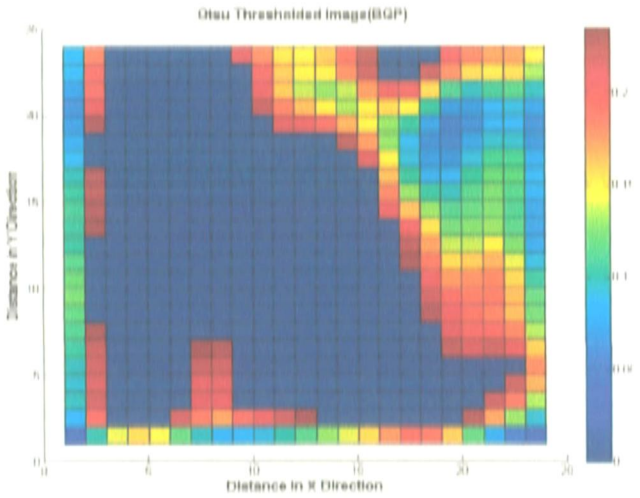

Fig. 4.63. (b) Otsu threshold image (BGP).

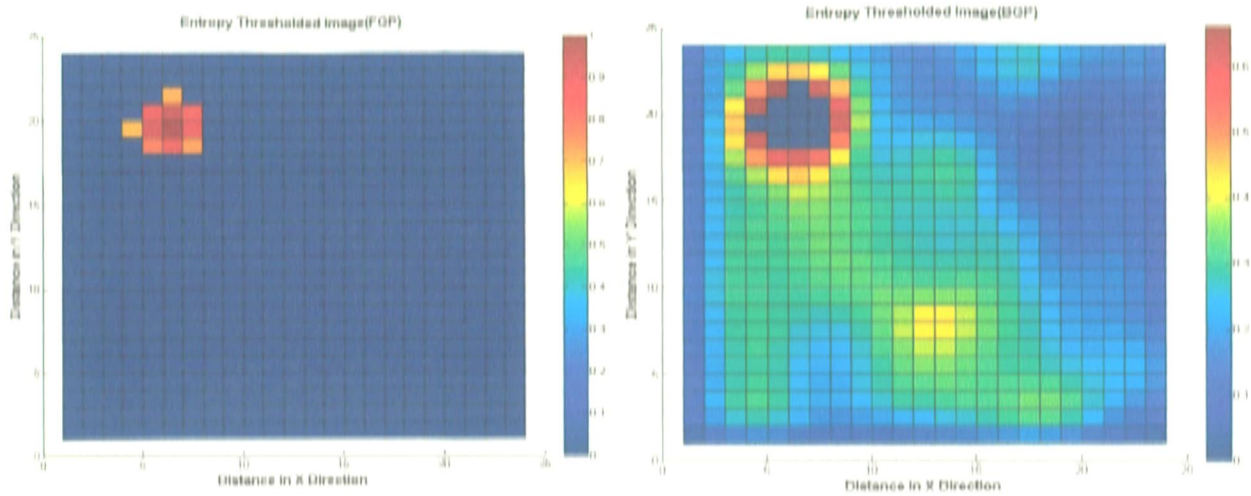

Fig. 4.64. (a) Entropy threshold image (FGP). Fig. 4.64. (b) Entropy threshold image (BGP).

At the depth of 8cm the cavity has not been detected in the iteration with the square plate. However in HH orientation for the triangular plate buried with the cavity 7 pixels of the cavity were visible. However we can safely claim that the chances of detection of the cavity at this depth are remote.

Also while using the Otsu threshold, the DA has dropped when compared to previous depths but FAR have increased. The DA and FAR for Entropy threshold are low as can be seen from the data in Table 4.4

The received power levels and statistics involved with the threshold image have been tabulated in Table 4.4 below.

Table 4.4 Power values and threshold statistics for different objects at 8 cm depth.

SER NO	TGT	POL	DEPTH	UNCAL POWER			CAL POWER			THRESHOLD LEVEL * a (Otsu) b (Entropy)		DET FIG	NO OF PIXELS	DETECTION ACCURACY (DA) IN %	FALSE ALARM RATE(FAR) IN %
				AVG	MAX	MIN	AVG	MAX	MIN						
1.	Sq Plate	HH	8 cm	-15.40	-11.39	-17.88	0.0952	0.2323	0.0521	0.4157	a	107.09	194	64.31	30.38
										0.775	b	150.25	18	28.57	0
2.	Sq Plate	VV	8 cm	-16.52	-11.42	-20.21	0.1534	0.4667	0.0617	0.2392	a	94.2	292	64.28	47.31
										0.7269	b	267	11	19.64	0
3.	Tri Plate	HH	8 cm	-15.11	-10.98	-17.88	0.1012	0.2553	0.0521	0.3804	a	81.46	206	57.5	34.14
										0.5965	b	120.48	34	40	3.35
4.	Tri Plate	VV	8 cm	-16.59	-9.56	-21.67	0.1512	0.7161	0.0041	0.2353	a	85.68	287	100	46.1
										0.6938	b	259.28	11	20	0.56

4.2 Results for the Experimental Work at C-band

The experimentation in the C-band was carried out using the cavity buried at three different depths in HH polarizations with square and triangular metal plate. It may be noted that as the antenna is placed at 40 cm above the sand surface the reflected power levels are stronger due to which the range of signal power is limited to within 1 dBm of power unlike the X-band case. The details of observations carried out in C-band and the subsections under which the analysis is carried out is given in Table 4.5

Table 4.5 Details of analysis and subsection at C-band.

Ser No	Polarization	Buried Object	Depth	Frequency	Subsection
1.	HH	Cavity with square plate	2 cm	6 GHz	4.2.1
2.	HH	Cavity with triangular plate	2 cm	6 GHz	4.2.2
3.	HH	Cavity with square plate	5 cm	6 GHz	4.2.3
4.	HH	Cavity with triangular plate	5 cm	6 GHz	4.2.4
5.	HH	Cavity with square plate	10 cm	6 GHz	4.2.5
6.	HH	Cavity with triangular plate	10 cm	6 GHz	4.2.6

4.2.1 Inverted Cavity with Square Metal Plate Buried at 2 cm Depth The cavity and metal plate (in this instance square plate) were buried at the depth of 2 cm and the observations are carried out with HH polarization. The processing has been carried out as given in the flow chart in Fig. 3.7. On completion of the preprocessing the normalized plot is obtained and shown in Fig. 4.64. Two peaks of different intensities are observed in

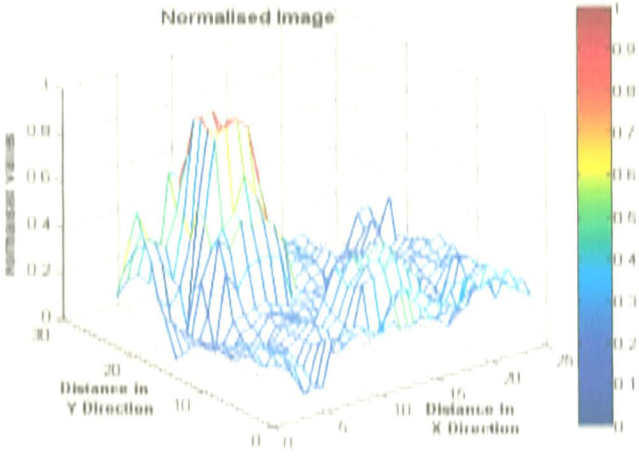

Fig. 4.65. Normalized 3D plot.

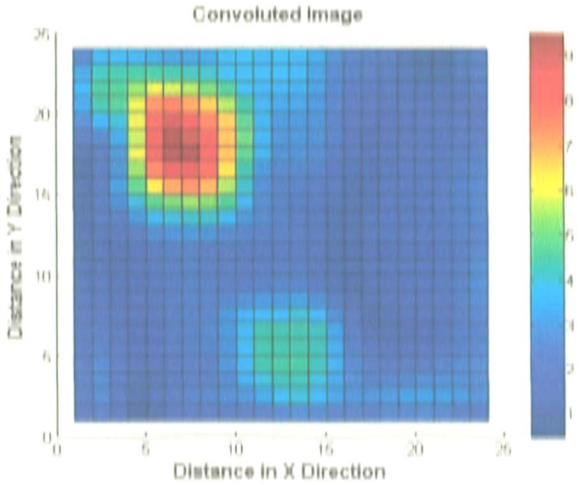

Fig. 4.66. Convoluted image.

the figure indicating the presence of cavity and metal plate. As a result of higher reflectivity the metal plate should have the higher peak while the lower peak should be representing the cavity. To analyze the data more critically further processing has been carried out.

The normalized data is then convoluted as described in section 3.2.2 to minimize the effect of neighboring pixels on pixel strength with the similar 3 × 3 convolution kernel. In convoluted image seen in Fig. 4.65, the higher intensity variation can be easily identified but it is difficult to infer the kind of target.

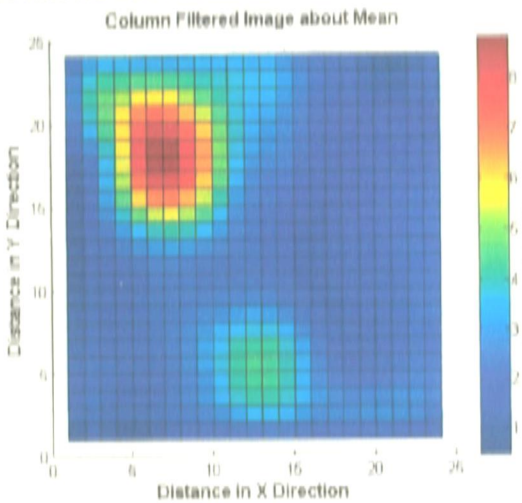

Fig. 4.67. (a) Column filtered image.

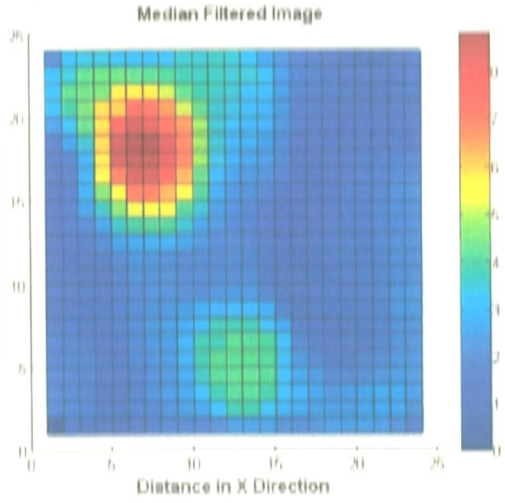

Fig. 4.67. (b) Median filtered image.

Filtering is carried out to improve the target pixel improvement. The columnwise filtered image about the mean and the median filters are used. The two filtered images are shown in Fig. 4.67. (a), (b). The smoothening of the convoluted data has taken place while the pixel range values in filtered image have dropped from a range of 0-8 from 0-9 as in case of the convoluted image. Thus the filtered image is ready for further processing.

Threshold is then applied to the filtered image by using the Otsu and Entropy threshold technique. While using the Otsu threshold (threshold level of 0.3725), as seen in Fig. 4.28. (a), two prominent regions have been identified in the FGP with 17 pixels accurately for the cavity and 34 for the metal plate to achieve a detection accuracy of 94.69% with a FAR of 8.36%.

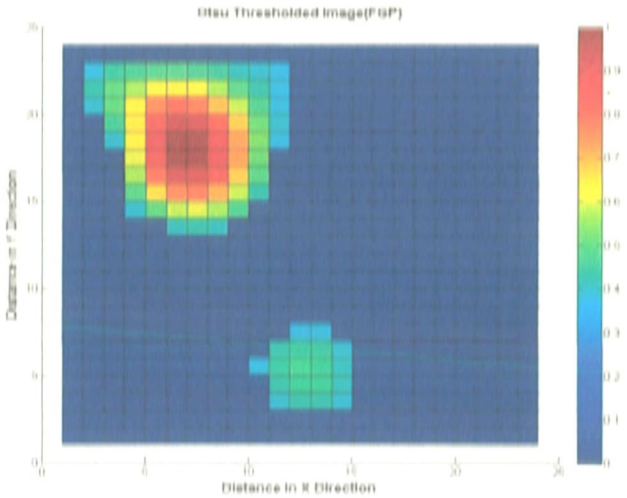

Fig. 4.68. (a) Otsu threshold (FGP).

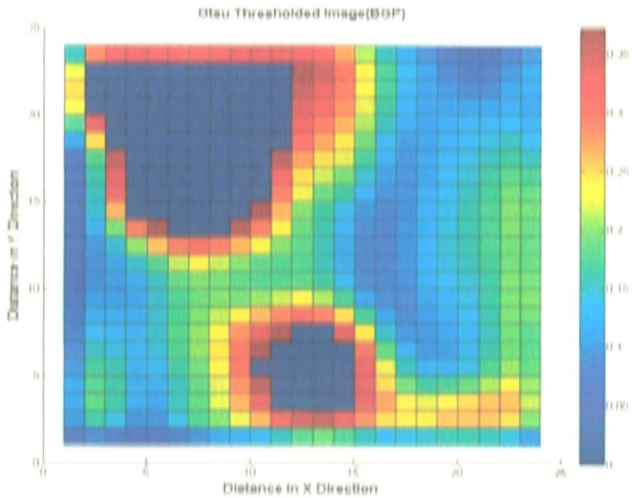

Fig. 4.68. (b) Otsu threshold (BGP).

While using the Entropy threshold technique, the value of threshold is set high at a figure of 0.8014 due to which only the 16 pixels of metal plate are observed in the FGP as seen in Fig. 4.29. (a) to achieve a DA of 28.57% and a false alarm of 0% as no pixel is falsely detected. However such a high threshold level masks the detection of the cavity which is undesirable. However the cavity is visible in the BGP image.

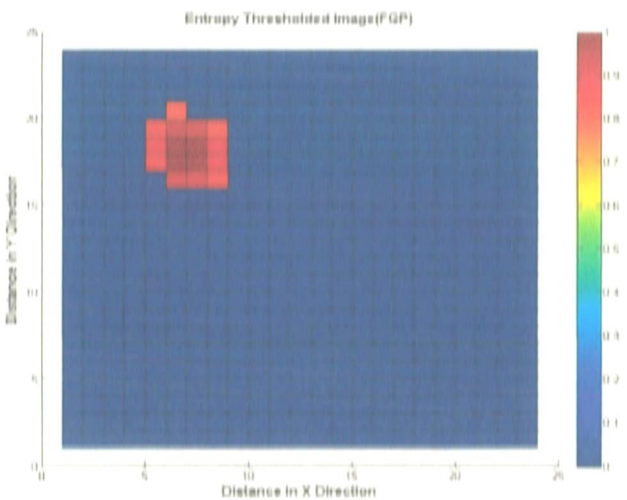

Fig. 4.69. (a) Entropy threshold (FGP).

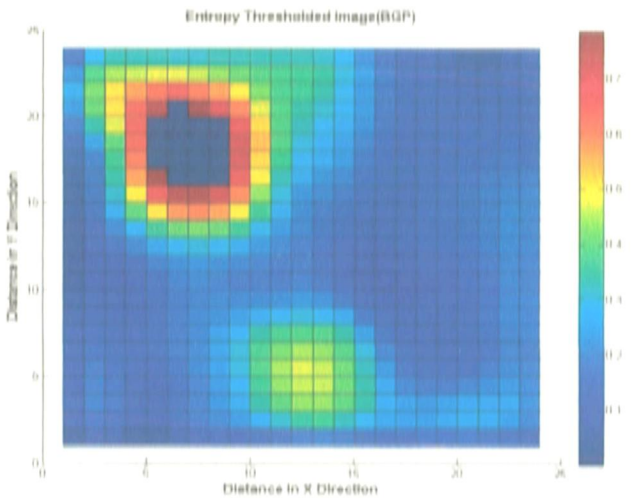

Fig. 4.69. (b) Entropy threshold (BGP).

4.2.2 Inverted Cavity with Triangular Metal Plate Buried at 2 cm Depth The cavity and triangular metal plate were buried at the depth of 2 cm and the observations are carried out with HH polarization as mentioned in Ser No 2 of Table 4.5.

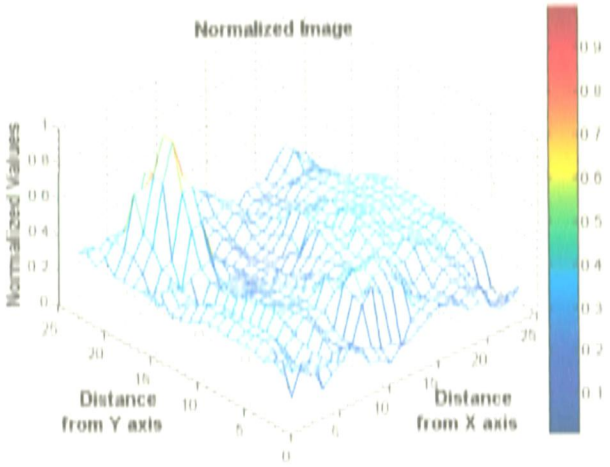

Fig. 4.70. Normalized 3D plot.

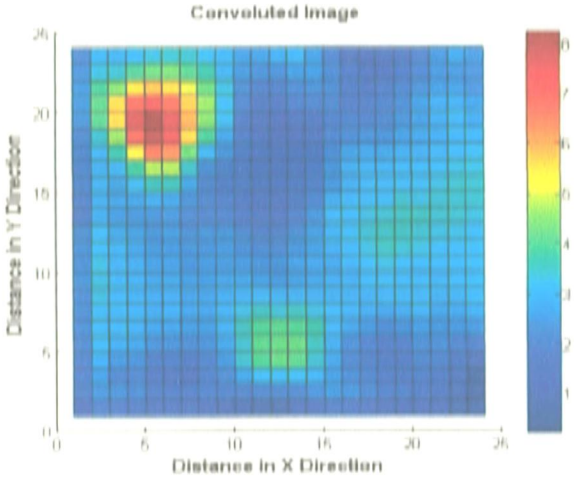

Fig. 4.71. Convoluted image.

The resultant of the preprocessed image after calibration and normalization is shown in Fig. 4.70. which points towards two bright regions indicating the presence of targets. However definite information about the target cannot be inferred at this stage. The normalized image is then subjected to the next level of processing in the sequence.

The convolution is carried out using the 3 × 3 convolution kernel. The image plot of the convoluted image shown in Fig. 4.71. shows three clusters of which one is towards higher range while two clusters are in the lower range. The convoluted image is in the range of 0-8 in this case.

To achieve desired target information from this data set the process of filtration is carried out using the two techniques. From the filtered image plots seen in Fig. 4.72. (a), (b) it can be seen that the third group of green coloured pixels have been elevated to level close to that of the second group which might be the cavity pixels. Thus the filtered images are ready for the next stage of image processing where in the threshold level will be set and compared to that of filtered image to carry out detection.

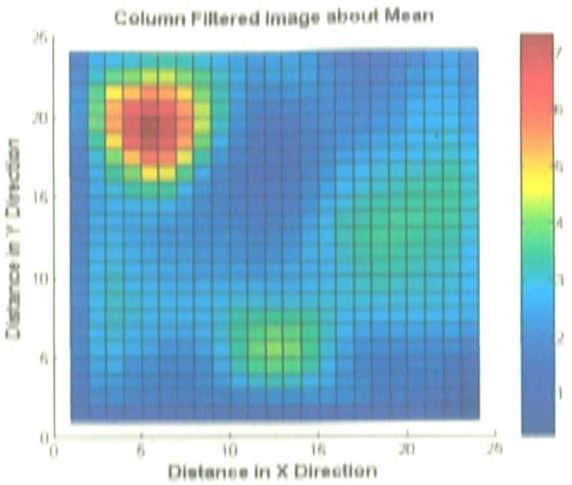

Fig. 4.72. (a) Column filtered image.

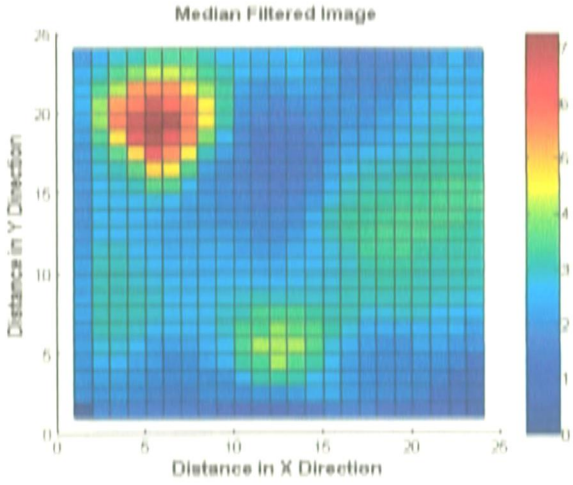

Fig. 4.72. (b) Median filtered image.

On application of the Otsu technique threshold level of 0.3412, 232 pixels were detected in Otsu technique achieving the DA of 97.73% with a FAR of 35.32%. Similarly with Entropy threshold of 0.6629, only 20 pixels are detected to provide a DA of 45.45% and FAR of 1.88%. Thus both the cavity and the metal plate have been detected with reasonable accuracy using the Otsu technique while the metal plate is easily detected in FGP image of entropy technique but cavity can be found in the BGP image as can be seen in Fig. 4.74. (b).

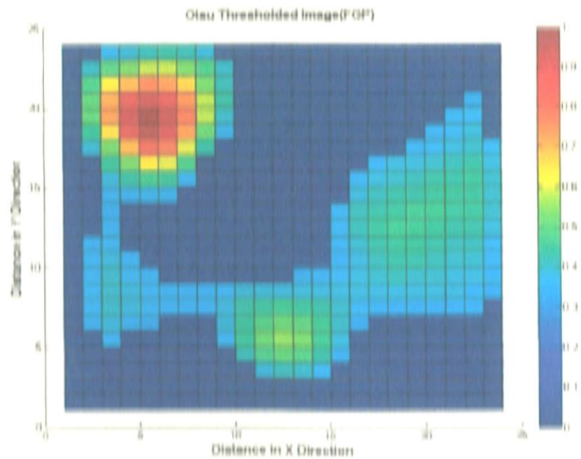

Fig. 4.73. (a) Otsu threshold (FGP).

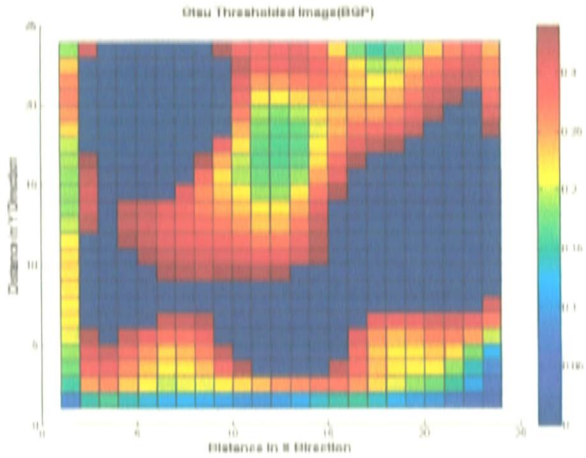

Fig. 4.73. (b) Otsu threshold (BGP).

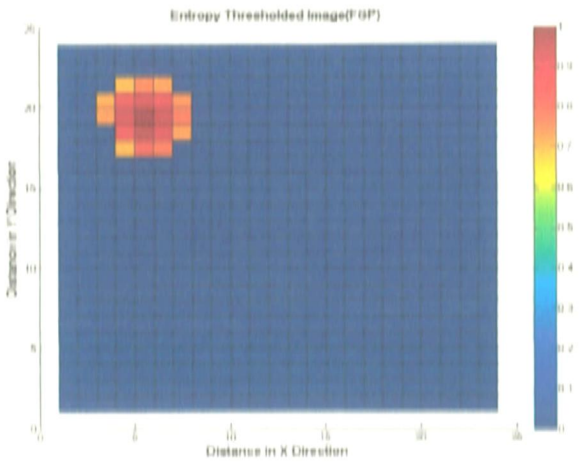

Fig. 4.74. (a) Entropy threshold (FGP).

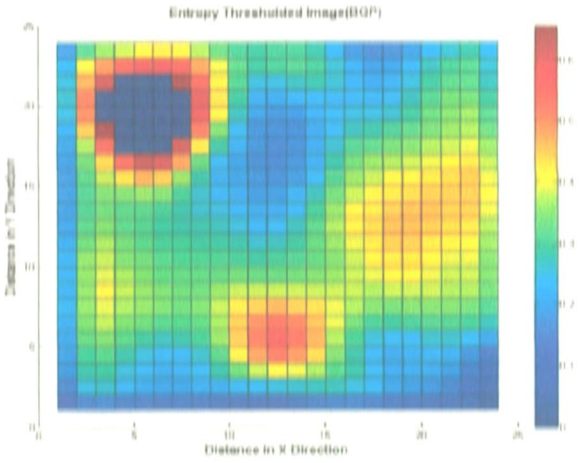

Fig. 4.74. (b) Entropy threshold (BGP).

4.2.3 Inverted Cavity with Square Metal Plate Buried at 5 cm Depth The cavity and metal plate (in this instance square plate) were buried at the depth of 5 cm and the observations are carried out with HH polarization. The processing has been carried out as given in the flow chart in Fig. 3.7. On completion of the preprocessing the normalized plot is obtained and shown in Fig. 4.75. Two peaks can be clearly seen of which the higher peak would be for metal plate for its better reflectivity

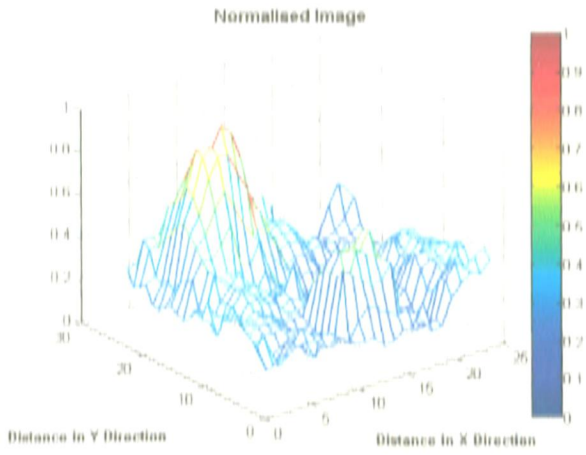

Fig. 4.75. Normalized 3D plot.

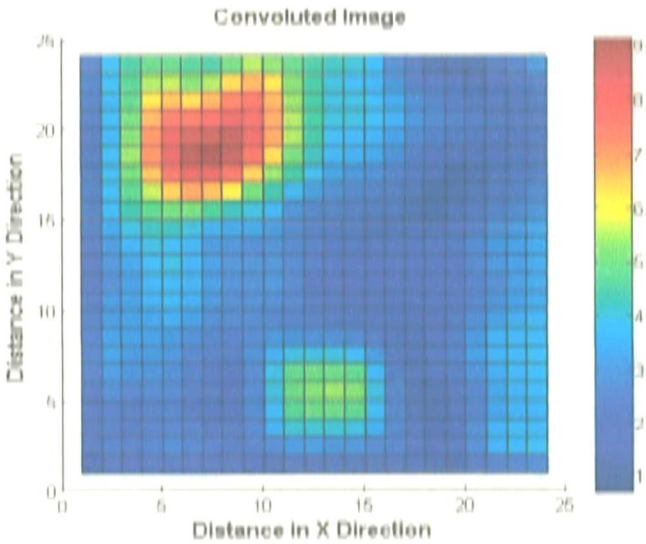

Fig. 4.76. Convoluted image.

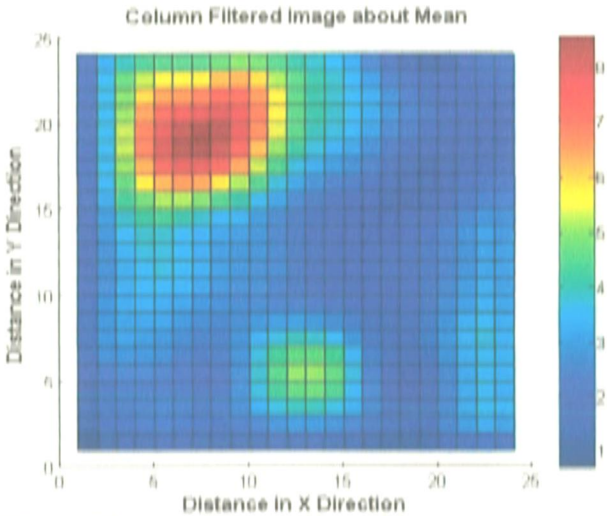

Fig. 4.77. (a) Column filtered image.

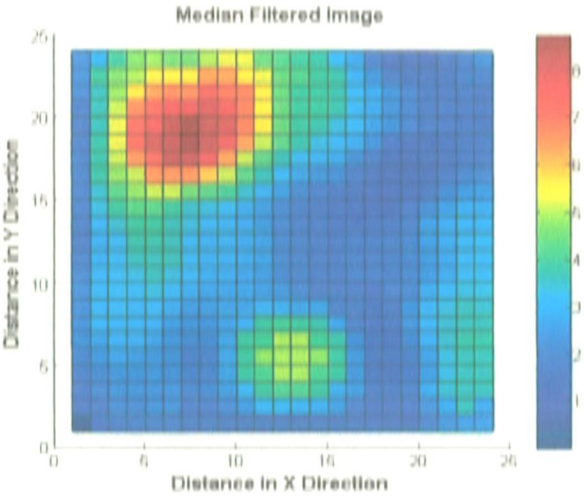

Fig. 4.77. (b) Median filtered image.

The next step involves convolution for enhancement of the filtered image. The convoluted image Fig. 4.76. also indicates a high intensity variation but it is difficult to infer the target. The next step of image enhancement is filtering in which the two filters are applied. The filtered images Fig. 4.77. (a), (b) indicate two clear cluster of pixels.

On applying the threshold we can see from the Fig. 4.33. (a) that using Otsu technique (threshold level of 0.4314) the cavity and metal plate have been detected with DA of 71.43% and FAR of 10.96%

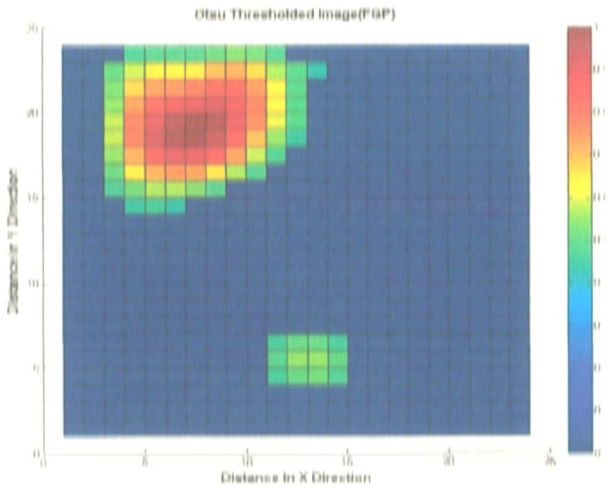

Fig. 4.78. (a) Otsu threshold (FGP).

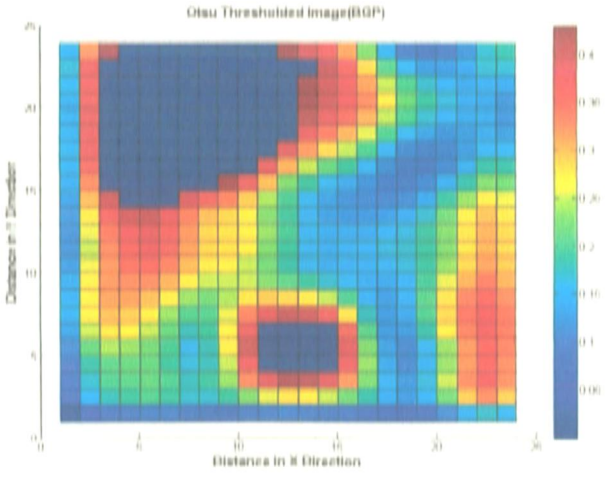

Fig. 4.78. (b) Otsu threshold (BGP).

However with entropy level at 0.2429 total 289 pixels were detected as can be seen in Fig. 4.34. (a). Besides cavity and metal plate another region of pixels has been detected which is a false alarm. The DA of 98.21% with FAR of 44.49% is achieved with Entropy threshold. Such a high level of FAR is due to a very low threshold value.

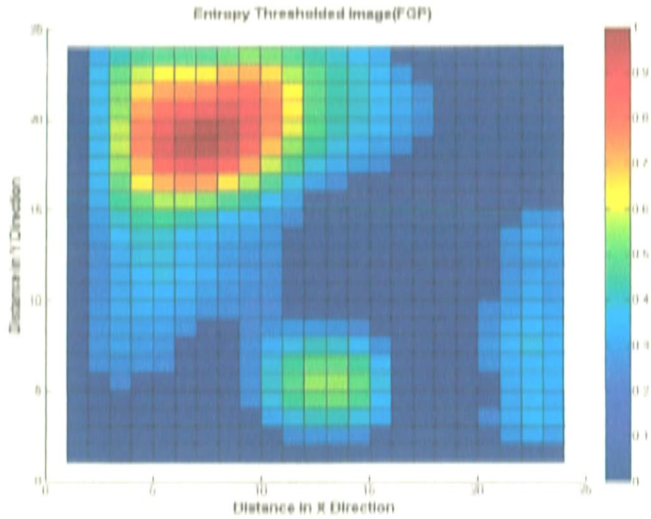

Fig. 4.79.(a) Entropy threshold (FGP).

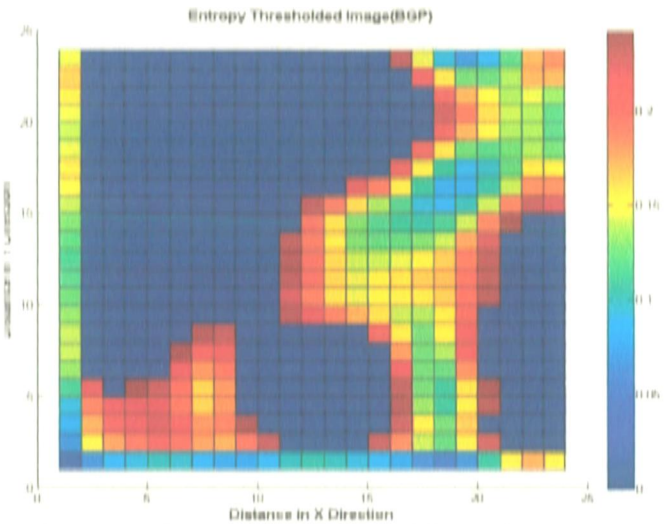

Fig. 4.79.(b) Entropy threshold (BGP).

4.2.4 Inverted Cavity with Triangular Metal Plate Buried at 5 cm Depth The cavity and triangular metal plate were buried at the depth of 5 cm and the observations are carried out with HH polarization as mentioned in Ser No 4 of Table 4.5.

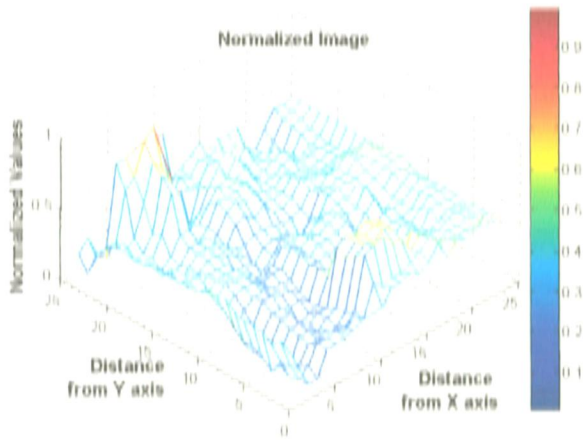

Fig. 4.80. Normalized 3D plot.

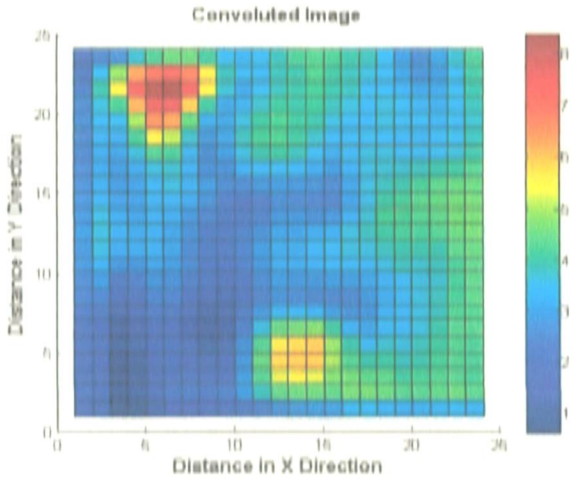

Fig. 4.81. Convoluted image.

This image is preprocessed by calibrating with the metal plate reading and normalization for which the 3-D plot is given in Fig. 4.80. Two higher intensity regions can be seen in this plot. In this image the higher intensity variation is seen but it is difficult to infer the kind of target.

This normalized image is then convoluted to minimize the effect of neighboring pixels as a process of image enhancement. In the convoluted image as seen in Fig. 4.81, we are able to view two prominent groups of pixels.

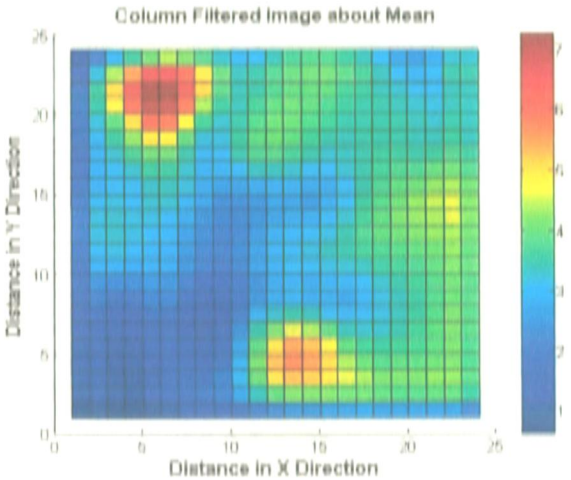

Fig. 4.82.(a) Column filtered image.

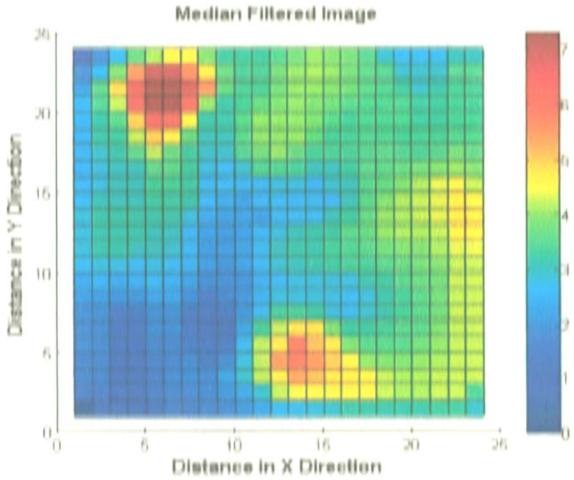

Fig. 4.82.(b) Median filtered image.

Filtering is carried out to improve the target pixel improvement. The columnwise filtered image about the mean and the median filters are used. The two filtered images are shown in Fig. 4.82. (a), (b). The images are now ready for the threshold and detection.

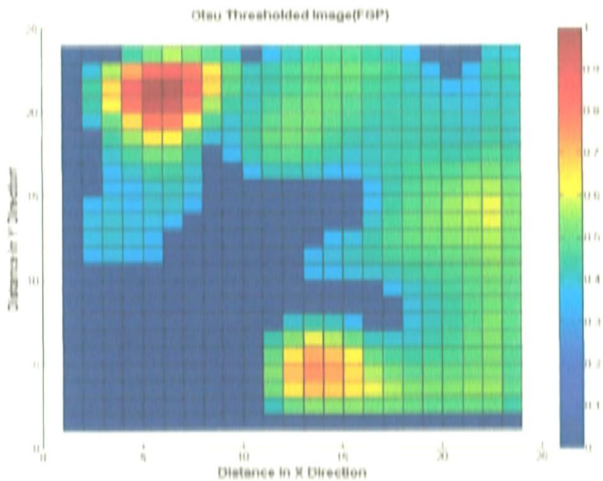

Fig. 4.83. (a) Otsu threshold (FGP).

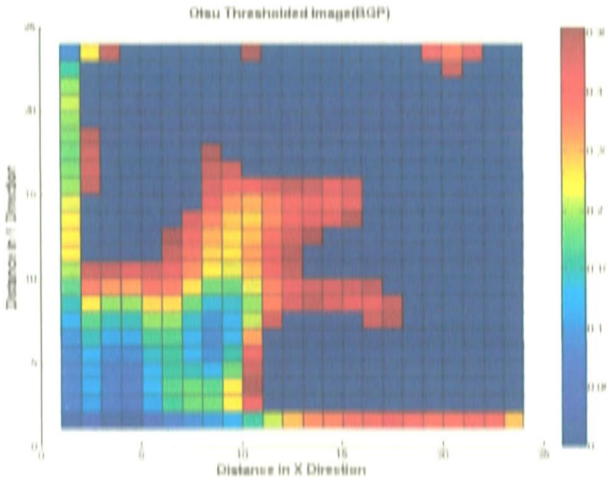

Fig. 4.83. (b) Otsu threshold (BGP).

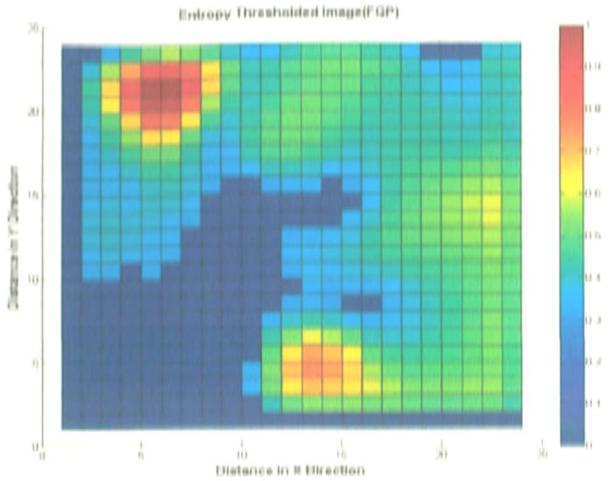

Fig. 4.84. (a) Entropy threshold (FGP).

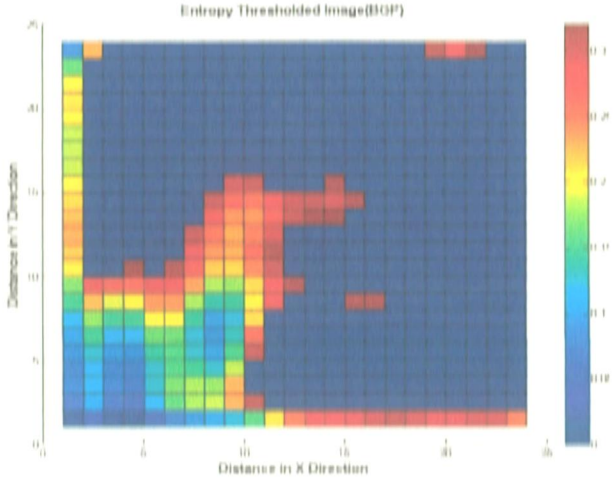

Fig. 4.84. (b) Entropy threshold (BGP).

The threshold is set based on Otsu and Entropy techniques which are set at 0.3569 and 0.3255 respectively. A total of 331 and 370 pixels were detected in Otsu and Entropy threshold giving the DA 100% in both cases and FAR of 53.95% and 61%. It can be seen clearly that both the cavity and the metal plate at this depth have been detected and distinguished but very high false alarm rates have been obtained.

4.2.5 Inverted Cavity with Square Metal Plate Buried at 10 cm Depth The cavity and metal plate (in this instance square plate) were buried at the depth of 10 cm and the observations are carried out with HH polarization.

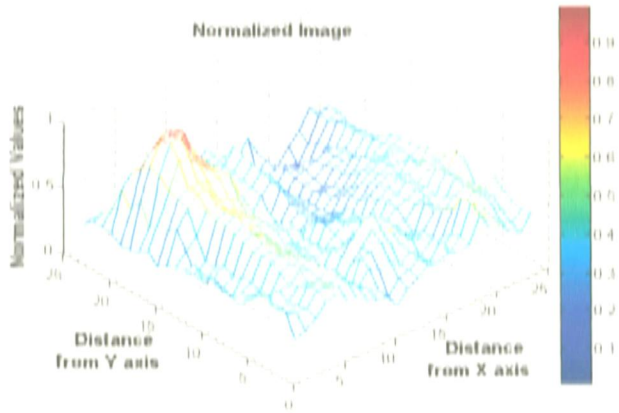

Fig. 4.85. Normalized 3D plot.

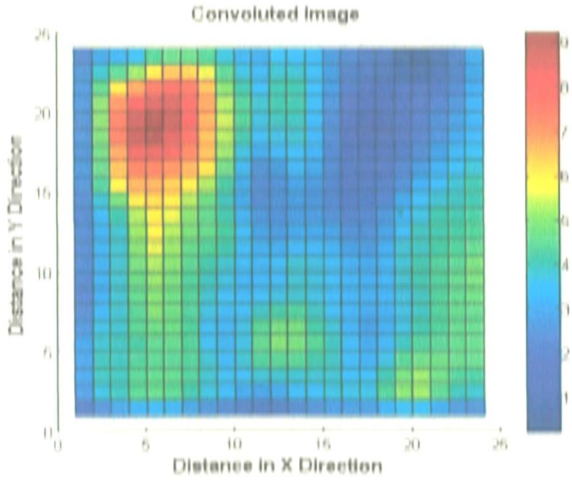

Fig. 4.86. Convoluted image.

The processing has been carried out as given in the flow chart in Fig. 3.7. On completion of the preprocessing the normalized plot is obtained and shown in Fig. 4.85. which indicates the presence of one sharp and few relatively low peaks.

This normalized image is then convoluted to minimize the effect of neighboring pixels as a process of image enhancement. In the convoluted image as seen in Fig. 4.86., we are able to view one prominent group of pixels and few more pixels. The image is now ready for enhancement by filtering. The two filters are applied and images obtained as seen in Fig. 4.87. (a), (b).

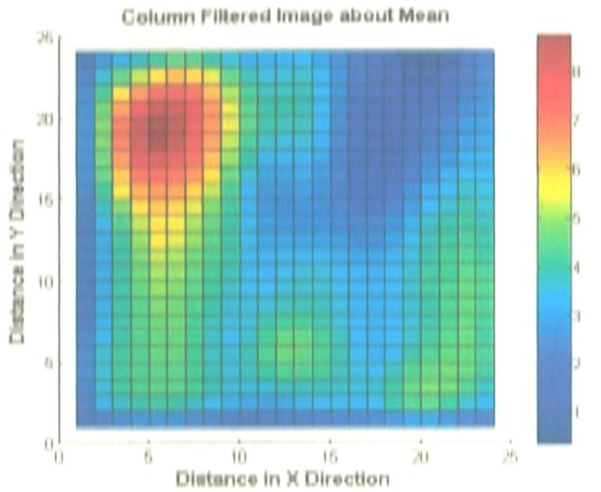

Fig. 4.87. (a) Column filtered image.

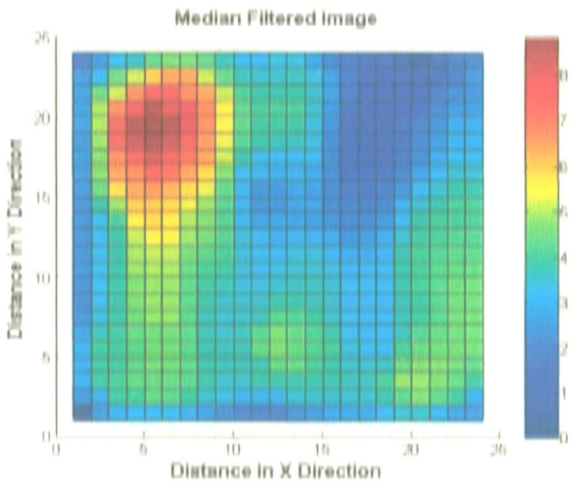

Fig. 4.87. (b) Median filtered image.

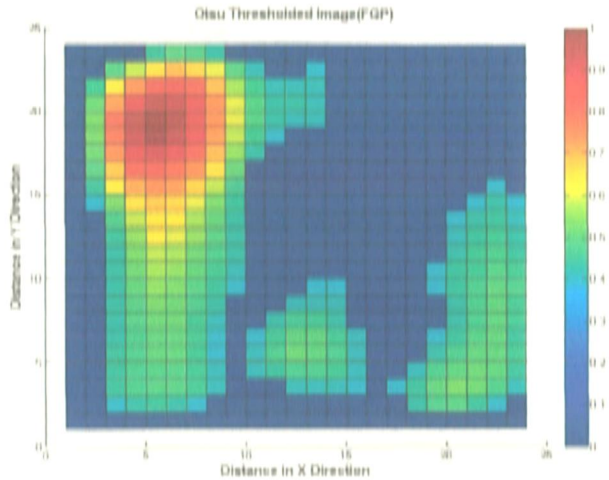

Fig. 4.88. (a) Otsu threshold (FGP).

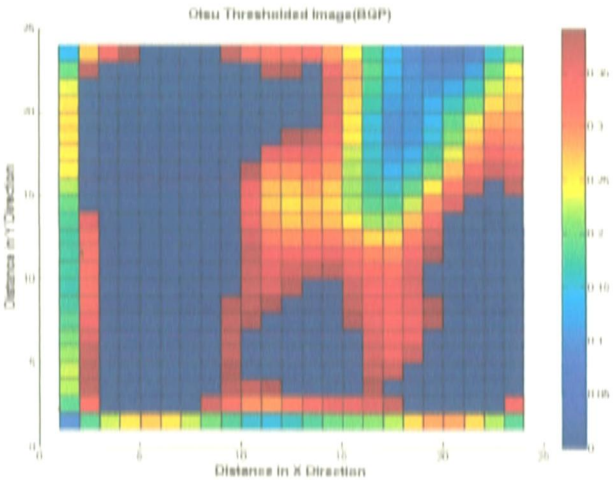

Fig. 4.88. (b) Otsu threshold (BGP).

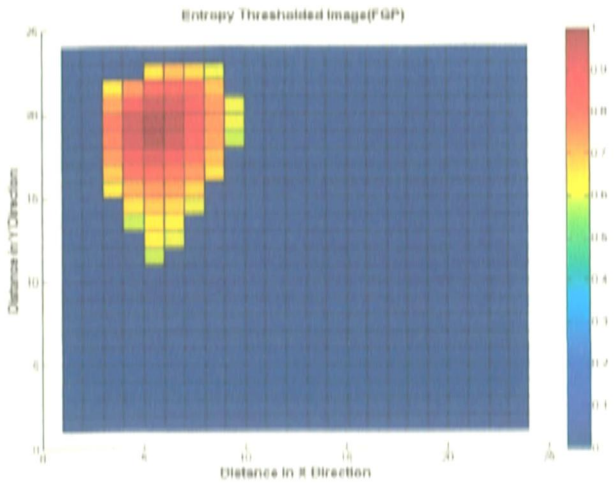

Fig. 4.89. (a) Entropy threshold (FGP).

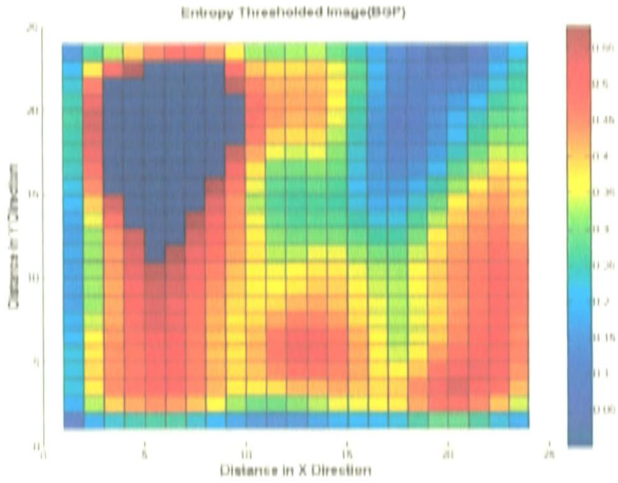

Fig. 4.89. (b) Entropy threshold (BGP).

The threshold is set based on Otsu and Entropy techniques which are set at 0.3992 and 0.5845 respectively. It can be clearly seen from Fig. 4.88. (a) and Fig. 4.89. (a) and threshold levels so obtained that entropy threshold technique is more stringent. A total of 261 and 58 pixels were detected in Otsu and Entropy threshold giving the DA of 96.43% and 62.5% and FAR of 42.96% and 4.37%. It can be seen clearly that both the cavity and the metal plate at this depth have been detected and distinguished with reasonably high accuracy using Otsu technique.

4.2.6 Inverted Cavity with Triangular Metal Plate Buried at 10 cm Depth The cavity and metal plate (in this instance triangular plate) were buried at the depth of 10 cm and the observations are carried out with HH polarization.

This image is preprocessed by calibrating with the metal plate reading and normalization for which the 3-D plot is given in Fig. 4.89. Two higher intensity regions can be seen in this plot. In this image the higher intensity variation is seen but it is difficult to infer the kind of target.

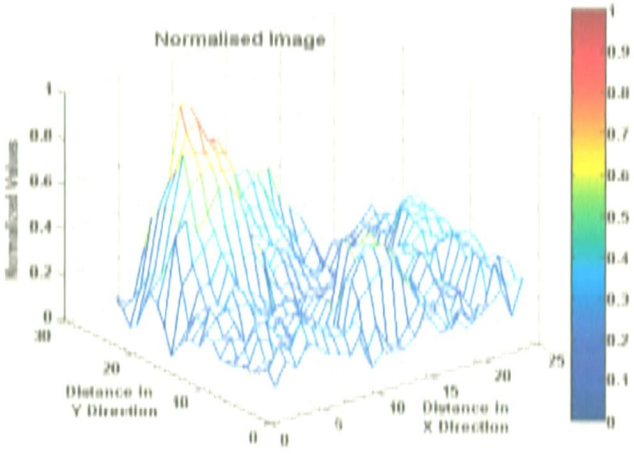

Fig. 4.90. Normalized 3D plot.

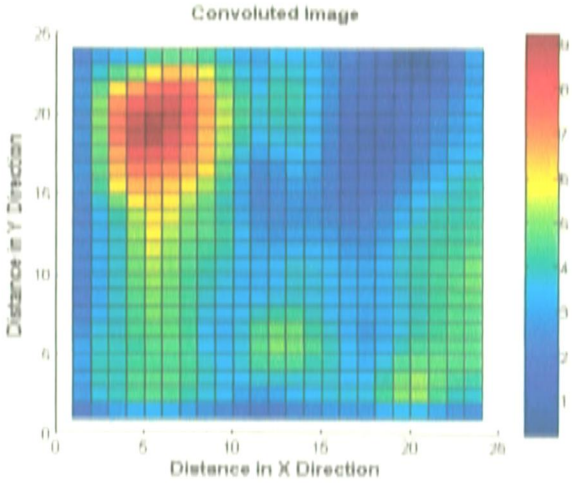

Fig. 4.91. Convoluted image.

This normalized image is then convoluted to minimize the effect of neighboring pixels as a process of image enhancement. In the convoluted image as seen in Fig. 4.91. we are able to view a prominent group of pixel.

To enhance the image further the two filtering techniques have been applied. The filtered images have been shown in Fig. 4.92. (a), (b) are again lying in the range of 0-8. The images are now ready for the threshold and detection.

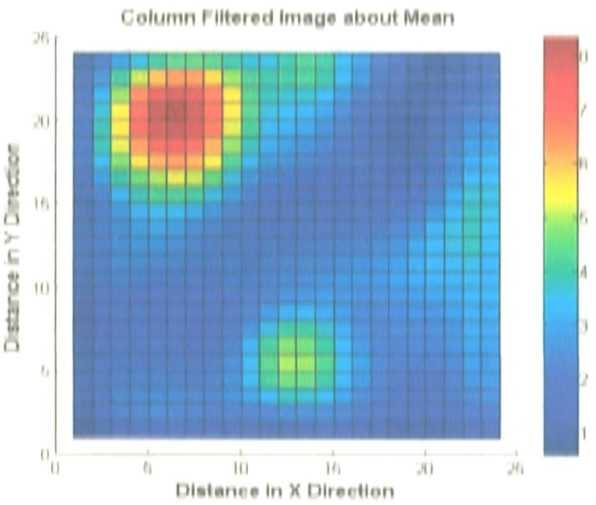

Fig. 4.92. (a) Column filtered image.

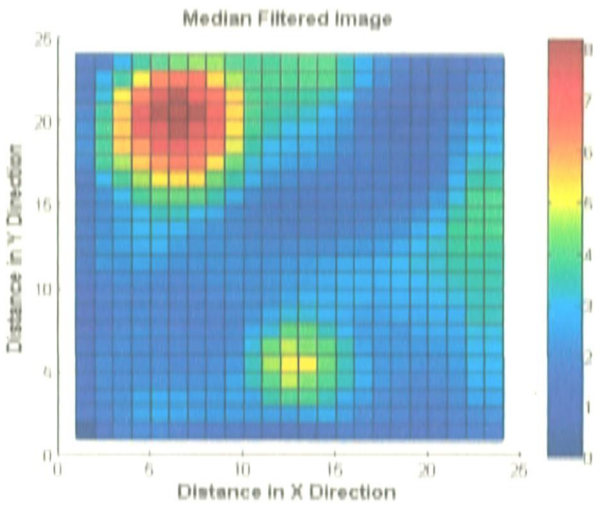

Fig. 4.92. (b) Median filtered image.

On applying Otsu threshold technique the cavity and metal plate are visible in FGP as seen in Fig. 4.93. (a), with threshold level set at 0.3922, a total of 95 pixels were detected with DA of 86.37% and FAR of 10.77%. For the high level entropy threshold set at 0.7188, only 22 pixels, in the region of metal plate, were detected with DA of 30% and FAR 1.69%.

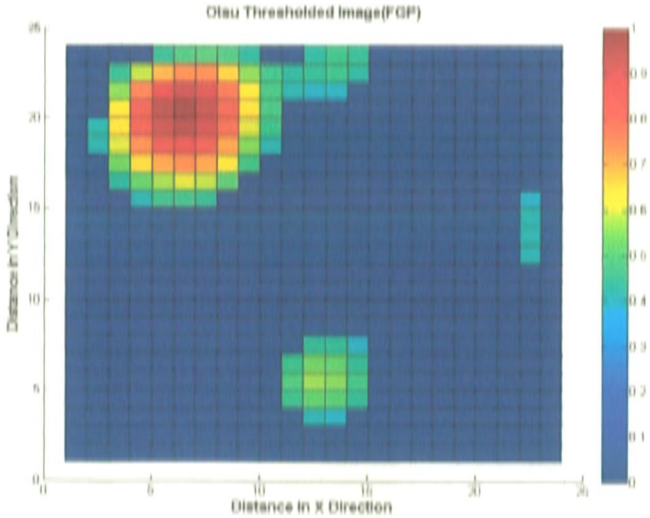

Fig. 4.93. (a) Otsu threshold (FGP).

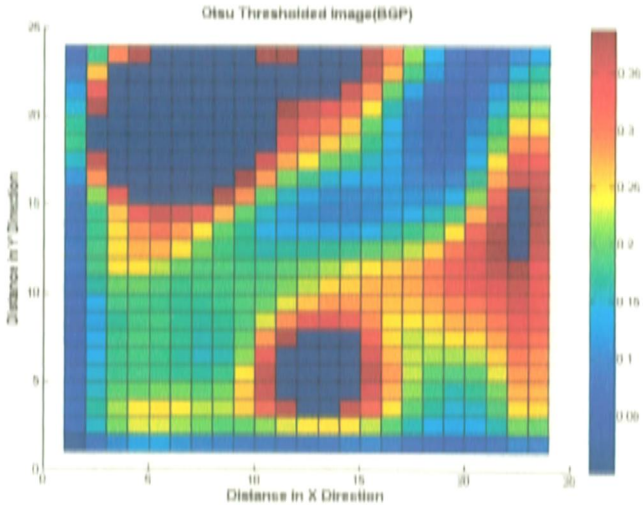

Fig. 4.93. (b) Otsu threshold (BGP).

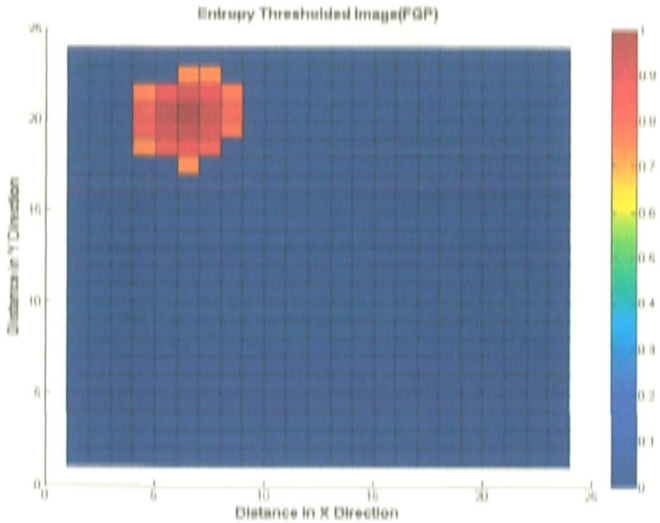

Fig. 4.94. (a) Entropy threshold (FGP).

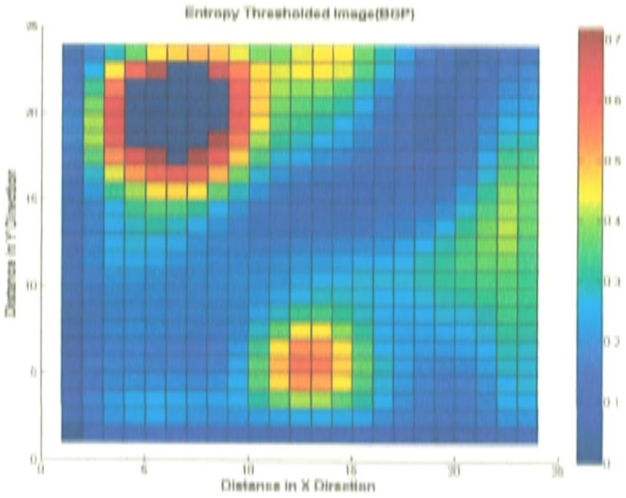

Fig. 4.94. (b) Entropy threshold (BGP).

On applying Entropy thresholding the metal plate is detected in FGP as seen in Fig. 4.94. (a) while the cavity is visible in BGP in Fig. 4.94. (b). The received power

levels and statistics involved with the threshold image have been tabulated in Table 4.6 below.

Table 4.6 Power values and threshold statistics for objects at C-band.

SCE NO	TGT	SOL	DEPTH	CAL POWER (dBm) AVG	MAX	MIN	CAL POWER AVG	MAX	MIN	THRESHOLD LEVEL	DET FOG	NO OF PIXELS	DETECTION ACCURACY (DA) IN %	FALSE ALARM RATE(FAR) IN %
1.	Sq Plate	HH	2cm	11.0644	11.46	10.91	0.8405	0.9304	0.8113	0.8725 a	165.08	95	54.83	8.25
										1.8014 b	284.62	16	38.57	0
2	Tri Plate*	HH	2cm	9.5415	10.11	9.51	1.5166	1.6467	1.4859	0.3412 a	87.14	222	96.72	56.52
* This feature was examined only with 16dBm of transmitted power										1.5529 b	166.216	35	25.75	1.37
3.	Sq Plate	HH	5cm	11.4053	11.89	11.16	1.0845	1.2155	1.0238	2.4014 a	148.35	95	21.46	15.96
										0.2429 b	45.07	283	58.21	44.49
4	Tri Plate	HH	5cm	11.284	11.79	11.11	1.2700	1.3830	1.0118	0.3266 a	65.6	331	100	52.08
										0.3229 b	71	370	100	61
5.	Sq Plate	HH	10cm	11.52	11.97	11.32	1.0684	1.1655	0.9860	3.3925 a	7.25	361	96.46	42.95
										0.5845 b	109.264	59	68.5	5.37
5	Tri Plate	HH	10cm	11.29	11.84	11.34	1.0042	1.0955	0.9605	0.3963	140.12	95	55.37	10.27
										0.7188 b	258.35	22	33	.69

4.3 Comparison of the Results at X and C-Bands

- The cavity and metal objects are better detected at C-band at depths greater than 5 cm visavis the X-band. The peaks for the backscattered power for the buried objects are more pronounced in the C band. This can be observed by comparing the normalized images as shown in the previous subsections. The detection of cavity beyond 8 cm using X-band frequency is uncertain. It can be seen in Table 4.4 that there is a reduction in the DA and rise in the FAR when analyzing the data at 8 cm.
- Although the surface has been leveled and kept dry, its effect is more pronounced at higher frequency as discussed in Chapter 2. This effect can be viewed from the raw image obtained at the C and X-band. Since the lower wavelength is more responsive to surface level we can seen a more spread in pixels in X band raw images visavis the C-band images. This spread can be attributed to the surface level which is frequency sensitive.

4.4 Discussion of Results

- Better results were obtained with the C band readings as the lower frequency waves achieve better result. Another important factor involved is that the antenna in this case was much closer to the surface than the X-band. The cavity was better visible in the C-band as has been discussed previously. The cavity has been detected with reasonable accuracy till 5 cm depth in X-band. However at 8 cm depth the cavity was not detected with complete accuracy as only half the numbers of total pixels were detected. In C-band the detection were reasonable accurate till 10 cm depth
- As the threshold value reduces the number of pixels detected on average increases thereby increasing the false alarm. Usually the Otsu threshold value is much lower than the values for the cavity due to which additional pixels are seen at lower depths, however as the depth increases the reflections from the cavity reduce and hence fall below the threshold. Entropy threshold on the other hand enforces a higher threshold level due to which the metal plate pixels are detected but the cavity pixels get suppressed and are not detected, especially as the depth increases.

At 8 cm depth in X band it has been observed that for the Otsu threshold, the detection accuracy and false alarm for HH in both types of metal plate is lower than the

VV orientation. Similarly for Entropy threshold also the detection accuracy for HH is lower than the VV orientation in both the cases.

- Since the metal has better reflectivity its returns were highest and hence the metal plate was easily detected practically at all levels.
- The detection accuracies are higher in VV orientations than the HH orientation as has been observed. However in some cases the FAR have also been higher.

CHAPTER 5

Conclusion and Future Scope for Work

The work carried out in this dissertation was aimed to detect the shallow buried subsurface cavity. For this purpose, a box shaped cavity open from one end was formed using soil with almost similar constitutive parameters as sand. This cavity was buried inverted in sand at different depths and using the scatterometer approach the backscattered power at different depths was observed. To add to the complexity metal plate of different shapes were also buried at the same depth as the cavity in the vicinity of the cavity. The backscattered powers were measured at two different frequencies in X and C-band. This raw backscattered power data was calibrated and normalized and simple algorithm was developed using techniques used in image processing. The spatial domain filtering was carried out to minimize noise and two threshold techniques were used to set a threshold level for the detection of cavity and the metal object buried besides it. It is observed that the cavity and metal plate can be detected together successfully with MRS by using suitable image analysis approach. Multifrequency observation is a good choice where we can get complimentary information of the cavity i.e. like detection of cavity will be more accurate in C-band while the area of the cavity will be more accurate in the X-band. Polarimetric analysis has been carried out in like polarization and it has been found that polarization can play an important role once the surface is not smooth.

5.1 Future Scope The work in this dissertation was carried out with single cavity. As the detection is possible the scope of the exercise can be increased to different dimensions and shapes of the cavity. This work can be extended for different surface roughness and soil moisture condition which can be similar to the exact field conditions.

REFERENCES

[1] C. Dourthe, C. Pichot, J. Y. Dauvignac, and I. Carlou, "Inversion algorithm and measurement system for microwave tomography of buried object," *Radio Science*, vol. 35, pp. 1097–1108, Oct. 2000.

[2] Z. Q. Zhang and Q. H. Liu, "Two nonlinear inverse methods for electromagnetic induction measurements," *IEEE Transactions on Geoscience and Remote Sensing*, vol. 39, no. 6, pp. 1331–1339, Jun. 2001.

[3] K. A. Michalski, "Electromagnetic imaging of elliptical-cylindrical conductors and tunnels using differential evolution algorithm," *Microwave Optical Technology Letter*, vol. 28, pp. 164–169, 2001.

[4] K. A. Michalski, "A neural-network approach to the electromagnetic imaging of elliptic conducting cylinders," *Microwave Optical Technology Letter*, vol. 28, pp. 303–306, 2001.

[5] D. J. Daniels, *Ground Penetrating Radar*. London, UK: IEE 2004.

[6] D. K. Butler, "Microgravimetric and gravity gradient techniques for detection of subsurface cavities," *Geophysics*, vol. 49, no. 7, pp. 1084–1096, Jul. 1984.

[7] C. R. I. Clayton, M. C. Matthews, and N. E. Simons, *Site Investigation*. UA, USA: Halsted Press, 1982.

[8] D. J. Daniel, D. J. Gunton, and H. F. Scott, "Introduction to the subsurface radar," in *IEE Proceedings*, vol. 135, pt. F, no. 4, pp. 274–320, Aug. 1988.

[9] H. Zhou and M. Sato, "Subsurface Cavity Imaging by Crosshole Borehole Radar Measurements," *IEEE Transactions on Geoscience and Remote Sensing*, vol. 42, no. 2, pp. 335–341, Feb. 2004.

[10] A. J. Kassab and J. F. Pollard, "Automated algorithm for the nondestructive detection of subsurface cavities by the IR-CAT method," *Journal of Nondestructive Evaluation*, vol. 12, no. 3, pp. 175–186, 1993.

[11] G. El Qady, M. Hafez, M. A. Abdalla, and K. Ushijima, "Imaging subsurface cavities using geoelectric tomography and ground-penetrating radar," *Journal of Cave and Karst Studies*, vol. 67, no. 3, pp. 174–181, Dec. 2005.

[12] T. Mochales, A. M. Casas, F. L. Pueyo, O. Pueyo, M. T. Roman, A. Pocovi, M. A. Soriano, and D. Anson, "Detection of underground cavities by combining gravity, magnetic and ground penetrating radar surveys: a case study from the Zaragoza area, NE Spain," *Environmental Geology*, 53, pp. 1067–1077, Apr. 2007.

[13] M. Bavec, M. Luetscher, and R. Olivier, "Integration of ground penetrating radar and microgravimetric methods to map shallow caves," *Journal of Applied Geophysics*, 46, pp. 249–262, 2001.

[14] Y. F. Abdelhady, S. M. Hanafy, E. A. Morsy, and H. S. Mashhal, "Combined geophysical techniques for cavity detection," *Egyptian Geophysical Society (EGS) Journal*, vol. 2, no. 1, pp. 147–151, 2004.

[15] R. Piwakowski, J. M. Wetelet, and D. Moreaux, "High-resolution seismic prospection of old gypsum mines: Evaluation for detection possibilities," European Journal of Environment and Engineering Geophysics, 2, pp. 22-33, 1997.

[16] P. Kourkoulis, and N. P. Goulty, "Seismic reflection imaging of gypsum mine working at Sherburn-In-Elmet," European Journal of Environment and Engineering Geophysics, 1, Yorkshire, England , pp. 53-63, 1996.

[17] D. W. Steeples and R. D. Miller, "Direct detection of shallow subsurface voids using high resolution seismic reflection techniques," in Proceedings on 2nd Multidisciplinary Conference on Sinkholes and the Environmental Impacts of Karst, Balkema, Rotterdam, Boston, 1987.

[18] S. M. de Jong and F. D. vander Meer, *Remote Sensing Image Analysis: Including the Spatial Domain*. Boston; Springer Science, 2005.

[19] *Fundamentals of Remote Sensing*, Canada Centre for Remote Sensing, 2008.

[20] *The Remote Sensing Tutorial - Radar and Microwave Remote Sensing Applications* URL.. http://rst.gsfc.nasa.gov/

[21] R. K. Carver, C. Elachi, and F. T. Ulaby, "Microwave remote sensing from space," in *Proceedings of IEEE*, vol. 73, no. 6, pp. 970–1013, Jun. 1985.

[22] A. K. Swami, "Detection and performance optimization of shallow buried objects with microwave and image analysis approach," M Tech thesis, IIT Roorkee, India, 2007.

[23] R. Honeycutt, "Active remote sensing applications to disaster management with implications to spectrum management," in *IEEE International Symposium on Geoscience and Remote Sensing, IGARSS*, pp. 4091–4094, Jul. 2007.

[24] P. M. Mather, *Computer Processing of Remotely-Sensed Images An Introduction*. West Sussex, England: John Wiley & Sons, 2005

[25] A. Low, "Coupled modelling of land surface microwave interactions using ENVISAT ASAR data," Ph.D. dissertation, Munich, 2004.

[26] J. S. Lee and E. Pottier, *Polarimetric Radar Imaging from Basics to Applications*. CRC Press, 2009.

[27] F. T. Ulaby, R. K. Moore, and A. K. Fung, *Microwave Remote Sensing Vol II*. Norwood, MA. Artech House, 1986

[28] R. R. Navalgund, V. Jayaraman, and P. S. Roy "Remote sensing applications: An overview," *Current Science*, vol. 93, no. 12, pp. 1747–1766, Dec. 2007.

[29] M. B. Wolfgang, "Recent advancements of radar remote sensing," in *Proceedings of Microwave Conference, Asia-Pacific*, pp.1–4, Dec 2007.

[30] P. Pampaloni and K. Sarabandi, "Microwave remote sensing of land," *Radio Science Bulletin*, no. 308, pp. 30–48, Mar. 2004

[31] D. Flett, R. D. Abreu, M. Arkett, and M. F. Gauthier, "Initial evaluation of Radarsat-2 for operational sea ice monitoring," in *IEEE International Symposium Geoscience and Remote Sensing, IGARSS 2008*, Boston, vol. 1, pp. I-9–I-12, Jul. 2008.

[32] M. Arkett, D. Flett, R. De Abreu, P. C. Colon, J. Woods, and B. Melchior "Evaluating AIOS-Pulsar for ice monitoring," in *IEEE International Symposium Geoscience and Remote Sensing, IGARSS 2008*, pp. V-188–191, Jul. 2008.

[33] F. J. Yanovsky and L. P. Ligthart, "Microwave remote sensing of dangerous meteorological phenomena," in *13th International Conference on Microwaves, Radar and Wireless Communications, MIKON*, vol. 3, pp.70–81, May 2000.

[34] D. Peppyne, D. Westbrook, B. Philips, E. Lyons, M. Zink, and J. Kurose, "Distributed collaborative adaptive sensor networks for remote sensing applications," in *American Control Conference*, USA, pp. 4167–4172, Jun. 2008

[35] E. Ceraldi, G. Franceschetti, A. Iodice, and D. Riccio, "Estimating the soil dielectric constant via scattering measurements along the specular direction," *IEEE Transactions on Geoscience and Remote Sensing*, vol. 43, no. 2, pp. 295–305, Feb. 2005.

[36] C. Kuo and M. Moghaddam, "Electromagnetic scattering from multilayer rough surfaces with arbitrary dielectric profiles for remote sensing of subsurface soil moisture," *IEEE Transactions on Geoscience and Remote Sensing*, vol. 45, no. 2, pp. 349–366, Feb. 2007.

[37] N. Pierdicca, L. Pulvirenti, F. Ticconi, and M. Brogioni, "Radar bistatic configurations for soil moisture retrieval: A simulation study," *IEEE Transactions on Geoscience and Remote Sensing*, vol. 46, no. 10, pp. 3252–3264, Oct. 2008.

[38] J. Daniels, D. G. Blumberg, L. D. Vulfson, A. L. Kotlyar, V. Freiliker, G. Ronen, and J. Ben-Asher, "Microwave remote sensing of physically buried objects in the Negev Desert: implications for environmental research," *Remote Sensing of Environment*, vol. 86, pp. 243–256, 2003.

[39] M. Petrou and P. Bosdogianni, *Image Processing: The Fundamentals*. John Wiley & Sons Ltd., 1999.

[40] R. C. Gonzalez and R. E. Woods, *Digital Image Processing*. New Delhi, India: Prentice Hall, 2005.

[41] J. S. Lim, *Two-Dimensional Signal and Image Processing*. New Jersey, USA: Prentice Hall, 1990.

[42] S. J. Chapman, *MATLAB Programming for Engineers*. Bangalore, India: Thomson Learning, 2007.

[43] G. Blanchet and M. Charbit, *Digital Signal and Image Processing using MATLAB*. London, UK: ISTE, 2006.

[44] D. Singh, "Electromagnetic and computational approach to detect the depth of buried object using the radar remote sensing data at X-band," in *Proceedings of Wave Propagation in Communication, Microwave Systems and Navigation, WPMN07*, Germany, pp. 98–103, 2007.

[45] H. C. Mahboob and D. L. Warren, "Image thresholding techniques," in *IEEE Proceedings of Pacific Rim Conference on Communications, Computers and Signal Processing*, Canada, pp. 585–589, May 1995.

[46] P. K. Sahoo, A. A Farag, and Y. F. Yeap, "Threshold selection based on histogram modeling," in *Proceedings of IEEE Conference Systems Man and Cybernetics*, Chicago, vol.1, pp. 351–356, Oct. 1992.

[47] C. I. Chang, Y. Du, J. Wang, S. M. Guo, and P. D. Thouin, "Survey and comparative analysis of entropy and relative entropy thresholding techniques," in *IEE Proceedings-Visual Image Signal Processing*, vol. 153, no. 6, pp. 837–850, Dec. 2006.

[48] N. Otsu, "A threshold selection method from gray-level histograms," *IEEE Transactions on Systems Man and Cybernetics*, vol. SMC-9, no. 1, pp. 62–66, Jan. 1979.

[49] T. Pun, "A new method for grey-level picture thresholding using the entropy of the histogram," *Signal Processing 2 North Holland Publishing Company*, pp. 223–237, 1980.

[50] J. N. Kapur, P. K. Sahoo, and A. K. C. Wong, "A new method for gray level picture thresholding using the entropy of the histogram," *Computer Vision, Graphics, and Image Processing*, 29, pp. 273–285, 1985.

APPENDIX A

```
%-------------------------------------------------------------
%Initialising and reading the data from the Recorded data
%-------------------------------------------------------------
E zeros(24,24);%Initialize matrix with all elements as zeros
E0 zeros(24,24);
M zeros(24,24);
e=zeros(24,24);
m=zeros(24,24);
E= xlsread('Path of the reflected power data file');% Read from the excel sheet
e= exp(E/10*log(10)),%Convert into power from dBm scale of excel sheet reading
M= xlsread('Path of calibration data file');% Read from the excel sheet
m= exp(M/10*log(10));
E0= e./m ;% Standardising the reading wrt metal sheet
figure, surfbar (E)
xlabel('Distance in X Direction','fontsize',12,'fontweight','b')
ylabel('Distance in Y Direction','fontsize',12,'fontweight','b')
title('Raw Image','fontsize',12,'fontweight','b')
colorbar()
figure, surface (E0)
xlabel('Distance in X Direction','fontsize',12,'fontweight','b')
ylabel('Distance in Y Direction','fontsize',12,'fontweight','b')
title('Calibrated Image','fontsize',12,'fontweight','b')
% %-------------------------------------------------------------
% %Normalisation of the raw data E0
% %-------------------------------------------------------------
En zeros(24,24);%Initialize matrix with all elements as zeros
a mean(mean(E0));%Finding the mean of E0
b max(max(E0));%Finding the max of E0
c=min(min(E0));%Finding the min of E0
```

```
En =(E0-c)/(b c);% Normalisation
figure,surface(En),% checking the image of E
xlabel('X Axis')
ylabel('Y Axis')
title('Normalised Image')
mesh (En);% mesh image of the normalised image
% %---------- ---------- ----------
% %Application of the convolution to the normalised image of En
% %-------- ---------- ----------
G=zeros(24,24);
F= [1 1 1 ;1 2 1 ;1 1 1];%Convolution kernel of 3x3 matrix
G = conv2(En,F,'same'),
figure, surface (G)
xlabel('Distance in X Direction','fontsize',12,'fontweight','b')
ylabel('Distance in Y Direction','fontsize',12,'fontweight','b')
title('Convoluted Image','fontsize',12,'fontweight','b')
colorbar()
% % %------ ---------- ---------- -------
% % %Application of the Col Filter
% % % The mean can be changed with maximum and minimum
% % %values as shown with commented code Line 61
% % % ---------- ---------- ----------
I2 = colfilt(G,[3,3],'sliding',@mean);
figure,surface (I2)
xlabel('Distance in X Direction','fontsize',12,'fontweight','b')
ylabel('Distance in Y Direction','fontsize',12,'fontweight','b')
title(' Column Filtered Image about Mean','fontsize',12,'fontweight','b')
colorbar()
im1=zeros(24,24);
im1=I2;
```

```
% I3 = colfilt(I,[3,3],'sliding',@min)
% % figure , mesh(I)
%  figure, surface (I3);
%  xlabel('X Axis')
% ylabel('Y Axis')
% title('Filtered Image about Min')
%colorbar()

L = medfilt2(I,[3 3]);
figure, surface (L)
title('Median Filtered Image','fontsize',12,'fontweight','b')
xlabel('Distance in X Direction','fontsize',12,'fontweigh','b')
ylabel('Distance in Y Direction','fontsize',12,'fontweigh','b')
colorbar()

% %  % %          ------------------          ------------------          --
% % % % Otsu Thresholding
% % % %  ------------------          ------------------          ----------
a  0;
b=0;
c=0;
a=min(min(I2));%Finding the mean of I0
b=max(max(I2));%Finding the max of I0
c=min(min(I2));%Finding the min of I0
I2n  (I2-a)/(b-c);% Normalisation
I2NxtStg= I2n;% The value has been set to be used in next stages
depth = 0;
level1 = gray(thresh(I2n);
level= level1;
k=0;
I22=zeros(24,24);
```

```
I23 =zeros(24,24);
for i=1:24
   for j=1:24
      if I2n(i,j)>level;
        k= k+1;
        I22(i,j)=I2n(i,j);
        else
        I23(i,j)=I2n(i,j);
      end
   end
end
level_otsu=level
aa=sum(I22(:))/k
bb=sum(I23(:))/(576-k)
cc=sum(I2n(:))/576
del(fig_otsu = ((aa-bb)/cc)*100
nopix_otsu=k
figure,surface(I22),colorbar
title('Otsu Thresholded Image(I/GI)','fontsize',12,'fontweight','b')
xlabel('Distance in X Direction','fontsize',12,'fontweight','b')
ylabel('Distance in Y Direction','fontsize',12,'fontweight','b')
figure,surface(I23),colorbar
title('Otsu Thresholded Image(BG)','fontsize',12,'fontweight','b')
xlabel('Distance in X Direction','fontsize',12,'fontweight','b')
ylabel('Distance in Y Direction','fontsize',12,'fontweight','b')
img=I22;
ima=max(img(:));
imb=min(img(:));
ims=std(img(:));
snrimg=20*log10((ima-imb)./ims)
s=imhist(I22);
```

```
figure, plot(s)
%%  %% ----------  ----------  ---------
%%%% Entropic Thresholding 1D
%%%%----------  ...  ----------  ----------
I2n  zeros(24,24); % Reinitialise the value of I2n to zeros
I2n  I2NxtStg; % Take the normalised value of filtered value from previous
% stage and place it again in I2n for this stage
w=0;
w=entropy1(I2n),
detfig=0;
k=0;
level  0;
I22  zeros(24,24);
I23=zeros(24,24);
level = w;
for i=1:24
   for j=1:24
      if I2n(i j)<level;
         k=k + 1;
         I22(i,j)  I2n(i,j);
        else
         I23(i,j)=I2n(i,j);
      end
   end
end
level_entropy1  w
aa1  sum(I22(:))/k;
bb1=sum(I23(:))/(576-k);
cc1=sum(I2n(:))/576;
detfig  entropy1    ((aa1-bb1)/cc1)*100
nopix  entropy1  k
```

```
figure,surface(I22),colorbar
title('Entropy Thresholded Image(IGP)','fontsize',12,'fontweight','b')
xlabel('Distance in X Direction','fontsize',12,'fontweight','b')
ylabel('Distance in Y Direction','fontsize',12,'fontweight','b')
figure,surface(I23),colorbar
title('Entropy Thresholded Image(IGP)','fontsize',12,'fontweight','b')
xlabel('Distance in X Direction','fontsize',12,'fontweight','b')
ylabel('Distance in Y Direction','fontsize',12,'fontweight','b')
```

```
% The function entropy1 is used for entropy thresholding.
% The input is the given image matrix.

function entropythresholdd = entropy1(image)
    grayimg = mat2gray(image);              % to convert the matrix into
                                              gray image
    [hist,x]=imhist(grayimg,256);           % the histogram of the image
    hist=hist/576;                          % normalised histogram
    n=256;
    s=1;
    kl = zeros(1,n);                        % the vector containing values
    for i=1:n
        kl(1,i)=hist(i);                        end
    x 1;
    p1 = zeros(1,256);
    p2=zeros(1,256);
    ax=zeros(1,n-1);
    ent=zeros(1,576);
    while(s<=n)
        for i=1:s
            p1(x,1)=kl(1,i);
        end
        pa = sum(p1);
        el = zeros(1,n);
        for i 1:s
            if(kl(1,i)~=0)
                e1(1,i)= -(kl(1,i)/pa)*(log(kl(1,i)/pa));
                                            % loop for 1st level
            end
        end
        ent1 = sum(e1);

        for i=s+1:n
            p2(1,i-s) kl(1,i);              %
        end
        pb=sum(p2);

        for i s+1:n
            if(kl(1,i)~=0)
                e2(1,i-s)=-(kl(1,i)/pb)*(log(kl(1,i)/pb));
                                            % loop for 2nd level
            end
        end
        ent2=sum(e2);

        ent(1,s)=ent1+ent2;
        s=s+1;
    end

    for i=1:256
        if(ent(1)==max(ent))                %
            k=i;
        end
    end
    entropy1=graythresh(k)
end                                 % end
```